INFORMATION TO USERS

The most advanced technology has been used to photograph and reproduce this manuscript from the microfilm master. UMI films the text directly from the original or copy submitted. Thus, some thesis and dissertation copies are in typewriter face, while others may be from any type of computer printer.

The quality of this reproduction is dependent upon the quality of the copy submitted. Broken or indistinct print, colored or poor quality illustrations and photographs, print bleedthrough, substandard margins, and improper alignment can adversely affect reproduction.

In the unlikely event that the author did not send UMI a complete manuscript and there are missing pages, these will be noted. Also, if unauthorized copyright material had to be removed, a note will indicate the deletion.

Oversize materials (e.g., maps, drawings, charts) are reproduced by sectioning the original, beginning at the upper left-hand corner and continuing from left to right in equal sections with small overlaps. Each original is also photographed in one exposure and is included in reduced form at the back of the book. These are also available as one exposure on a standard 35mm slide or as a 17" x 23" black and white photographic print for an additional charge.

Photographs included in the original manuscript have been reproduced xerographically in this copy. Higher quality 6" x 9" black and white photographic prints are available for any photographs or illustrations appearing in this copy for an additional charge. Contact UMI directly to order.

U·M·I

University Microfilms International
A Bell & Howell Information Company
300 North Zeeb Road, Ann Arbor, MI 48106-1346 USA
313/761-4700 800/521-0600

Order Number 8920614

The production of very-high-energy light particles in heavy ion reactions, $E/A \leq 40$ MeV/u

Shaheen, Salem Ali Salem, Ph.D.

The University of Michigan, 1989

U·M·I
300 N. Zeeb Rd.
Ann Arbor, MI 48106

THE PRODUCTION OF VERY-HIGH-ENERGY LIGHT PARTICLES IN HEAVY ION REACTIONS, $E/A \leq 40$ MeV/u

by

Salem Ali Salem Shaheen

A dissertation submitted in partial fulfillment
of the requirements for the degree of
Doctor of Philosophy
(Physics)
in The University of Michigan
1989

Doctoral Committee:
- Professor Frederick Becchetti, Chairman
- Professor Daniel Axelrod
- Associate Professor Henry Griffin
- Professor Karl Hecht
- Professor Michael Longo

To my respectable parents who provided me
with their love, blessing and support.
To my wife and children who tolerated my
absence during the course of this work.
To my loving brothers and sisters.

ACKNOWLEDGEMENTS

I would like to express my deep appreciation to all those who joined me in this work to make it a successful one, especially my thesis advisor Prof. F.Becchetti for his persistent care. Also, I thank our experimental nuclear physics group (Prof. A. Nadasen, Prof. J. Janecke, Dr. D. Roberts, Dr. R. Stern, Mr. W. Liu and Ms. M. Dowell) who helped during the experiments.

My thanks are also due to the staff of Argonne National Laboratory (ANL), the staff of the National Superconducting Cyclotron Laboratory (NSCL) especially Dr. T. Murakami, Dr. J. Winfield and Mr. W.K. Wilson for their cooperation and assistance, and the staff of Indiana University Cyclotron Facility (IUCF) for their cooperation. Also I thank my doctoral committee for their time and patience.

Finally, I thank King Abdul Aziz University and the National Science Foundation (NSF) for financial support.

TABLE OF CONTENTS

LIST OF FIGURES

Figure

LIST OF TABLES

<u>Table</u>

LIST OF APPENDICES

Appendix

CHAPTER I

INTRODUCTION

I.1 History and Motivation for the Research

Apart from cosmic ray experiments, heavy-ion induced ($A \geq 4$) nuclear collisions were almost unknown before the 1960's[1] when the first hilacs (heavy-ion linear accelerators) and heavy-ion cyclotrons were built at Berkeley, Yale, and Oak Ridge. Since then this area of study has grown very quickly and has provided exciting insights on nuclei and nuclear dynamics[1].

In the early stages of the study of heavy-ion collisions, accelerators weren't powerful enough to produce beams with energies much higher than the Coulomb barrier. For example, Britt and Quinton[2] observed many energetic alphas and protons emitted in the bombardment of ^{197}Au and ^{209}Bi by beams of ^{12}C, ^{14}N and ^{16}O of energy $E_{\rm beam}/A$ = 10.5 MeV/u. In another experiment Newman and Steigert[3], in order to study the response of the Sodium Iodide (NaI) scintillators to energetic heavy ions as a function of the beam energy, used beams of ^{4}He, ^{10}B, ^{11}B, ^{12}C, ^{14}N, ^{16}O, ^{19}F and ^{20}Ne accelerated to 10 MeV/u. These energies are just at the repulsive nuclear Coulomb barrier heights. Although this energy was much higher than the previously available energies, the need for higher energies still existed. Therefore in the 1970's more heavy-ion accelerators were built to accelerate ions such as U to an energy higher than 10 MeV/u. For example, at IUCF (Indiana University Cyclotron Facility) He and Li ions can be accelerated to 30 - 90 MeV/u, at Atlas-ANL (Atlas Argonne National Laboratory) ^{16}O can be accelerated to 40 MeV/u, at the k = 500 (k is the parameter used to categorize the energy range of the cyclotron, given by k = $\frac{AE_{max}}{q^2}$ where A is the atomic mass in a.m.u. of the accelerated ion, E_{max} is the maximum energy obtained for that ion and q is its charge state[4]) NSCL-MSU Cyclotron (National Superconducting Cyclotron Laboratory at Michigan State University) ^{4}He, ^{6}Li, ...^{40}Ar can be accelerated to 30 MeV/u, and at the Lawrence Berkeley Laboratory at UC/Berkeley ^{16}O and other heavy ions can be accelerated to 147 MeV/u. It seems that there is a semi-agreement among the researchers to divide the beam energy range into three intervals, namely low, intermediate and high for the energies $E \leq 10$ MeV/u, 10 MeV/u$< E \leq 100$ MeV/u and $E > 100$ MeV/u respectively[5].

With heavy-ion beams now available at high energies, scientists have the chance to study nuclear matter under different conditions, *e.g.* higher densities than those of normal nucleus, that can't be produced with any other probe[6]. Therefore, now there is a major effort in heavy-ion research to investigate all possible reaction mechanisms. One aspect involves study of the emitted particle spectra very thoroughly so one can understand the mechanisms of the reactions and the nuclear structures involved. The evolution of the reaction mechanisms with beam energy is known generally, as reported by Ref. 2, to be mainly due to formation and decay of the compound nuclear system at low energies and mainly due to projectile or target break-up and transfer reactions at high energies. The situation at intermediate energies is less understood. One mechanism generally becomes the dominant reaction in each extreme energy range. These different mechanisms are incorporated in different theoretical models but they do not constitute a completely understood and agreed-upon theory. There are many questions that need to be answered - for example at what bombarding energy does sequential projectile break-up (as distinct from prompt break-up which takes place during the time scale of the collision and in the field of the target nucleus) become an important process?[7]. Can the particle spectra observed at low, intermediate and high bombarding energies be understood in the context of some simple model? Therefore the experiments must be done in various ways, *i.e.*, different beams, energies, targets, detectors, coincidence set-ups, and electronics, to investigate each possible mechanism and provide a suitable range of data for the various theoretical models.

For technological reasons, accelerators were first developed either at low energy, below 20 MeV/u or at high energy from 250 MeV/u to 3 GeV/u. Later on, acceleration at intermediate energies was possible[1]. At low energies it is assumed that all nuclear reactions proceed via one-body processes (long mean free path), *i.e.*, the projectile nucleus interacts with the target nucleus as a whole. At high energies, however, nucleon-nucleon scattering should become increasingly important (short mean free path)[8,9], *i.e.*, nucleons in the projectile nucleus interact with nucleons in the target nucleus directly. A transition might then be expected to occur as the velocity of the colliding nuclei approaches, and then exceeds the velocity of sound in nuclear matter ($\simeq$ 15 MeV/u) or the intrinsic Fermi velocity ($\simeq$ 35 MeV/u)[8,10,11]. Other thresholds can be surpassed at these energies: i) the mean nucleon binding energy, $B \doteq 8$ MeV/u (if the average participant excitation energy $E^* = E_{\text{beam}} \frac{A_1 A_2}{(A_1+A_2)^2}$, where A_1 and A_2 are the mass numbers of the target and the projectile, exceeds B a "total explosion" is possible), and ii) the pion production threshold ($\doteq$ 150 MeV/u).

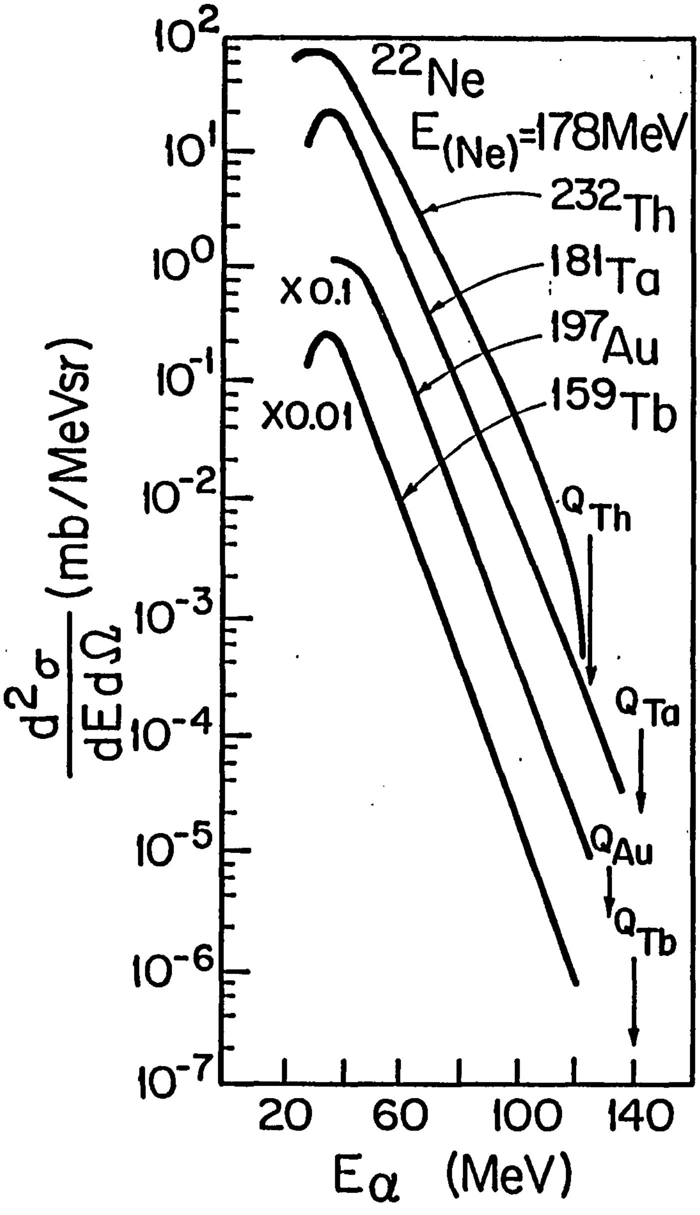

Fig. I.1. Measured α-particle energy spectra at 0° in laboratory. The arrows indicate where the calculated $E_\alpha^{\max}$ should be assuming two body final state reaction with $E_\alpha^{\max} = E_{\text{beam}} + Q_{\text{value}} - E_{\text{R}}$ (Ref.12). E_{R} is the residual nucleus recoil energy($<< E_\alpha$).

An important phenomenon which is noticed for the intermediate energy range and which perhaps doesn't get the attention it deserves is the production of very energetic light particles (p, d, t, α) at forward angles, especially near $\theta = 0°$, and their production rates relative to the incident heavy ion beam and its energy. It has been observed that alpha particles can be produced at zero degrees with energies much higher than E_{beam}/A,*i.e.*, the projectile velocity, as seen in Fig. I.1. What happens at still higher beam energies? One expects that the spectra of light particles will extend further in energy and may approach the full beam energy.

As mentioned earlier, a group at Dubna (Ref. 12) claimed to have measured (at 0°) high energy α-particles with energies well above the quoted limit for a three-body final state and very close to the maximum energy possible assuming a two-body final state from ^{20}Ne, ^{22}Ne, and ^{40}Ar induced reactions *i.e.* $A(^{20}\text{Ne},\alpha)B$. Their projectile and target combinations were: $E(^{22}\text{Ne}) = 178$ MeV on ^{159}Tb, ^{181}Ta, ^{197}Au and ^{232}T, $E(^{20}\text{Ne}) = 110$, 196 MeV on ^{181}Ta and $E(^{40}\text{Ar}) = 220$ MeV on ^{232}Th, as seen in Fig. I.1, I.2 and I.3. From Fig. I.1, we see $E_{\alpha}^{\max} \simeq 128$ MeV in the reaction of 178 MeV ^{22}Ne on ^{197}Au. The two body limit is $E_{\alpha}^{\max} \simeq 128$ MeV and the three-body limit cited is $E_{\alpha}^{\max} \simeq 70$ MeV. A group at Jülich (Ref. 13) believe that most of the high energy yields of Ref. 12 is from a three body final state reaction: $A +^{22}\text{Ne} \rightarrow B + C + \alpha$ via a breakup (*i.e.*, more than two fragments in the final state) mechanism. In their experiment (Ref. 13) of ^{197}Au (^{20}Ne, α) with $E_{\text{Ne}} = 392$ MeV, they observed $E_{\alpha}^{\max} = 185$ MeV (Fig. I.4.) which is far below the two-body limit of 342 MeV and the three-body or break-up limit of 379 MeV. Therefore it is not clear what kind of break-up mechanism they refer to in their theoretical calculations. Also, they believe that the three-body limit of 70 MeV quoted in Ref. 12 would be for a particular composite system but from

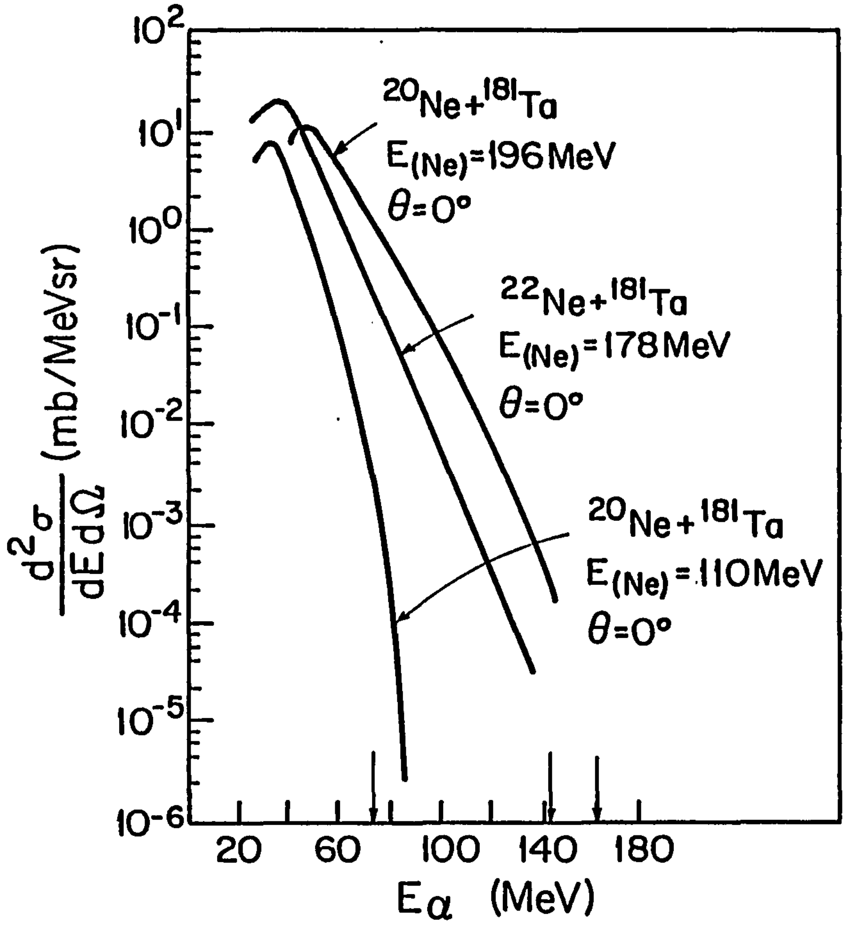

Fig. I.2. α-particle energy spectra measured at 0° in laboratory. The arrows indicate the possible $E_{\alpha}^{\max}$ ($=E_{\text{beam}}+Q_{\text{value}}-E_{\text{R}}$), assuming two body final state reactions (Ref.12).

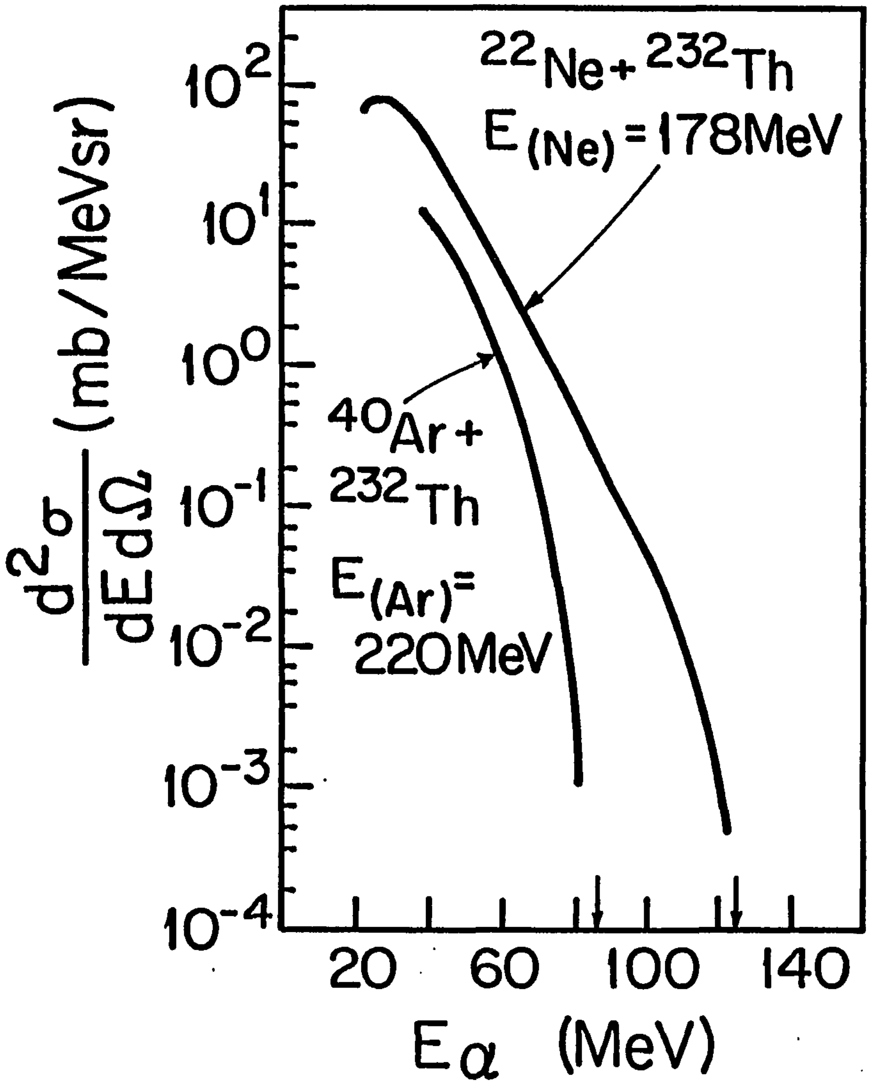

Fig. I.3. α-particle energy spectra measured at 0° in laboratory. The arrows are as indicated for Figs. 1 & 2 (Ref.12).

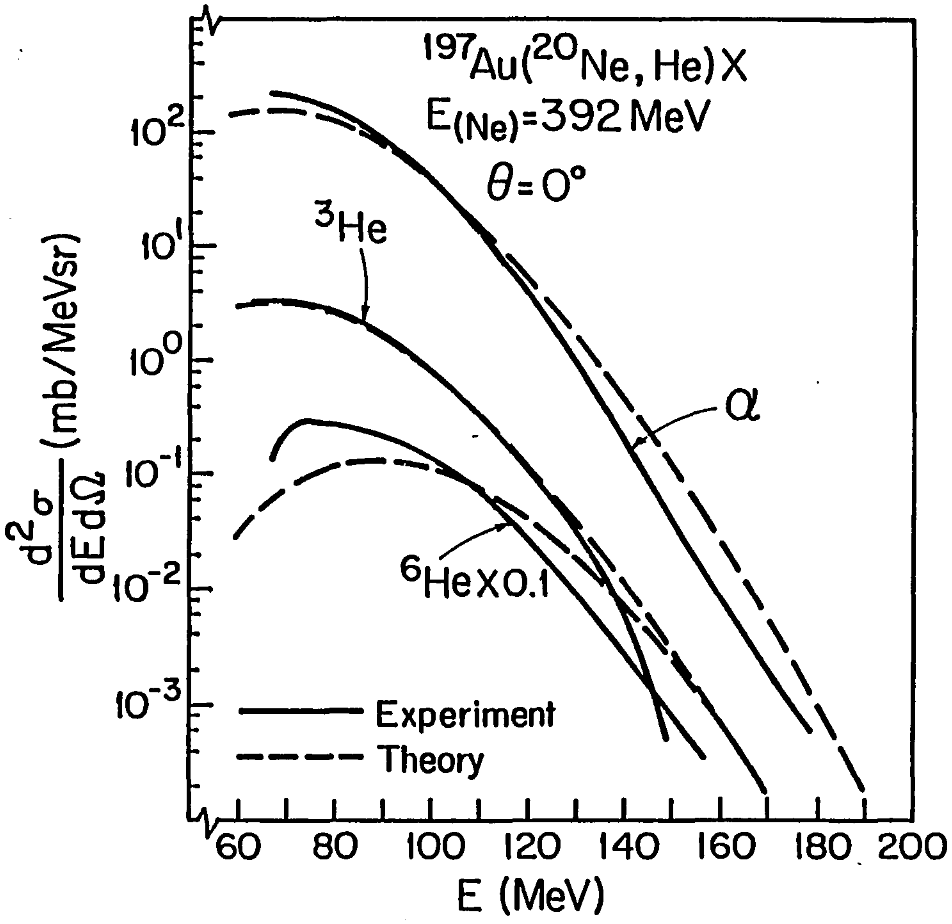

Fig. I.4. Experimental energy spectra of He isotopes detected at 0° in laboratory and compared with break-up calculations (Ref.13).

a break-up reaction ^{197}Au (^{22}Ne, ^{18}O + α), E_{α}^{max} = 162 MeV. Now the question raised is why the results of Ref. 12 agree with two-body kinematics while the results of Ref. 13 do not. This suggests that the reaction mechanism is different at the two energies. In any case, it can be concluded that the origin of these energetic light particles is not yet entirely determined. Since this observation is noticed in this transitional ion energy range, many experiments at these energies are needed to determine the source of these particles. Most of the existing data give inclusive results, *i.e.* without specifying the production mechanism. So far exclusive data are not generally available. Besides that the spectra of the charged particles are not as simple as those of γ-rays and neutrons due to the coulomb repulsion effects unless the particle emission takes place far away from the target nucleus.[14,15] Also one more point which has to be determined is, what is the role of the target, *i.e.*, the dependence on A_t? Fig. I.1 gives α spectra for the same energy and projectile but different targets. Fig. I.2 gives α spectra for same target and almost the same projectile but at different energies. Fig. I.3 gives α spectra for the same target with different projectiles and energies. It is noticeable how different the spectra appear to be.

Research at higher energies automatically creates another requirement, which is to find suitable energetic light-particle detectors. One such detector is BGO (Bismuth Germinate Oxide) scintillator, which is known for its high density (7.13 g/cm^3) and consequently its high stopping power[16]. Therefore BGO is suitable for measurements at the forward directions and zero degrees, in particular, since it can stop the energetic emitted light particles[17]. Measurements with scintillators always create a problem which is related to the accuracy of the particle energy measured. Due to the lack of the experimental data on the response of the scintillators to light particles, an extrapolation (although non-linear) is necessary to high energy.

The lack of these data in part is due to the recent introduction of BGO. Although Sodium Iodide (NaI) scintillators are much older than BGO it is not an easy job to measure their response to light particles and γ-rays together at different energy ranges. Despite these calibration problems the choice of the scintillators (BGO and NaI) as an E (energy) detector is usually made due to their ease of use and adequate light particle identification (time of flight in BGO and both time of flight and pulse shape discrimination in NaI).

It is clear that the focus of the present research, *i.e,* the study of the energetic light particles produced in the heavy ion collisions mainly at forward angles, is a new and unique one. It is not a matter of light particles being produced at high energy but being produced at energies much higher than what is expected from the existing experiments and many theories. Hence one goal of this research is, obviously, to establish this observation as an acceptable fact by performing many experiments confirming the same phenomenon. The other goal is to interpret the data in a way to explain the origin of these particles. So far, measurements at or near 0° are very limited and therefore research in this area is a new subfield. Several experiments were done with beams of O, S, Ar and Ni at non-relativistic beam energies. The beam energies used were about 10 MeV/u for ^{32}S and ^{58}Ni, 14 MeV/u for ^{32}S, 20 MeV/u for ^{40}Ar, 30 MeV/u for ^{16}O and ^{40}Ar and 40 MeV/u for ^{16}O. The target used most often was Ta, although data were also obtained with Cu. Some data, *i.e.*, for the ^{16}O beams, showed that protons can extend to about half of beam energy and alphas can approach the *full* beam energy. Since there are many possible mechanisms for the interaction in heavy ion collisions, one expects that there may be new mechanisms by which these very energetic ($E \rightarrow E_{\text{beam}}$) light particles are produced.

In Chapter 2, I will outline the theoretical aspects of this problem. Different theories will be mentioned which could explain the origin of these energetic particles and predictions of the various models will be given. In Chapter 3, the detection system, the experimental setup, the particle identification system and the calibration methods will be discussed. In Chapter 4, the data and comparisons with model fits will be presented. Chapter 5 will present the conclusions and recommendations for further research ideas. Appendices outline the nuclear Fermi gas model (Appendix A), transformation of the cross-section equations from the rest frame to the laboratory system (Appendix B) and the particle identification methods (Appendix C).

CHAPTER II

THEORETICAL ASPECTS

II.1. Overview of Reaction Mechanisms in Heavy Ion Collisions

Nuclear reactions with heavy ion (HI) beams have led to the introduction of many concepts about HI reaction mechanisms. Although it is reasonable to say that massive or cluster transfer (as distinct from a few and single nucleon transfer such as pickup and stripping mechanisms) and projectile breakup (*i.e.* more than two fragments) are the main reaction mechanisms that have been introduced, each has other submechanisms. These two mechanisms are considered direct processes (Fig. II.1) as compared to non-direct compound nucleus formation (complete fusion) and decay[2,18] which dominates at low beam energies.

A nuclear reaction can take place only if the energy of the incident ion is at least comparable with that of the Coulomb barrier, $E_B = Zz\,e^2/R$, where $R = R_1 + R_2$ is the separation of the centers of the two ions; Z and z are the atomic numbers of the ions. In terms of atomic masses E_B can be written as E_B (MeV) = 1.03 $Zz/(A_{particle}^{1/3} + A_{nucleus}^{1/3})$. At these energies, heavy ions have wavelengths much less than their radii, so that in some respects their motion can be considered similar to that of a classical particle[18].

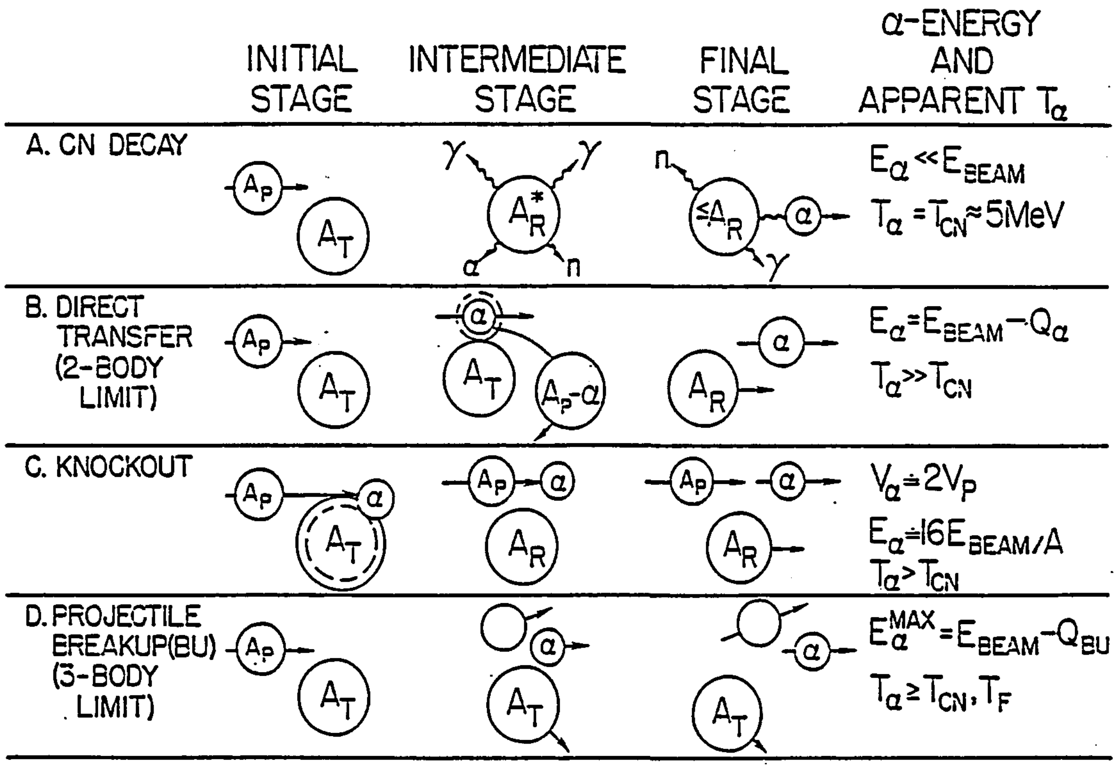

Fig. II.1. Schematic representation of heavy ion nuclear reactions producing energetic light particles.

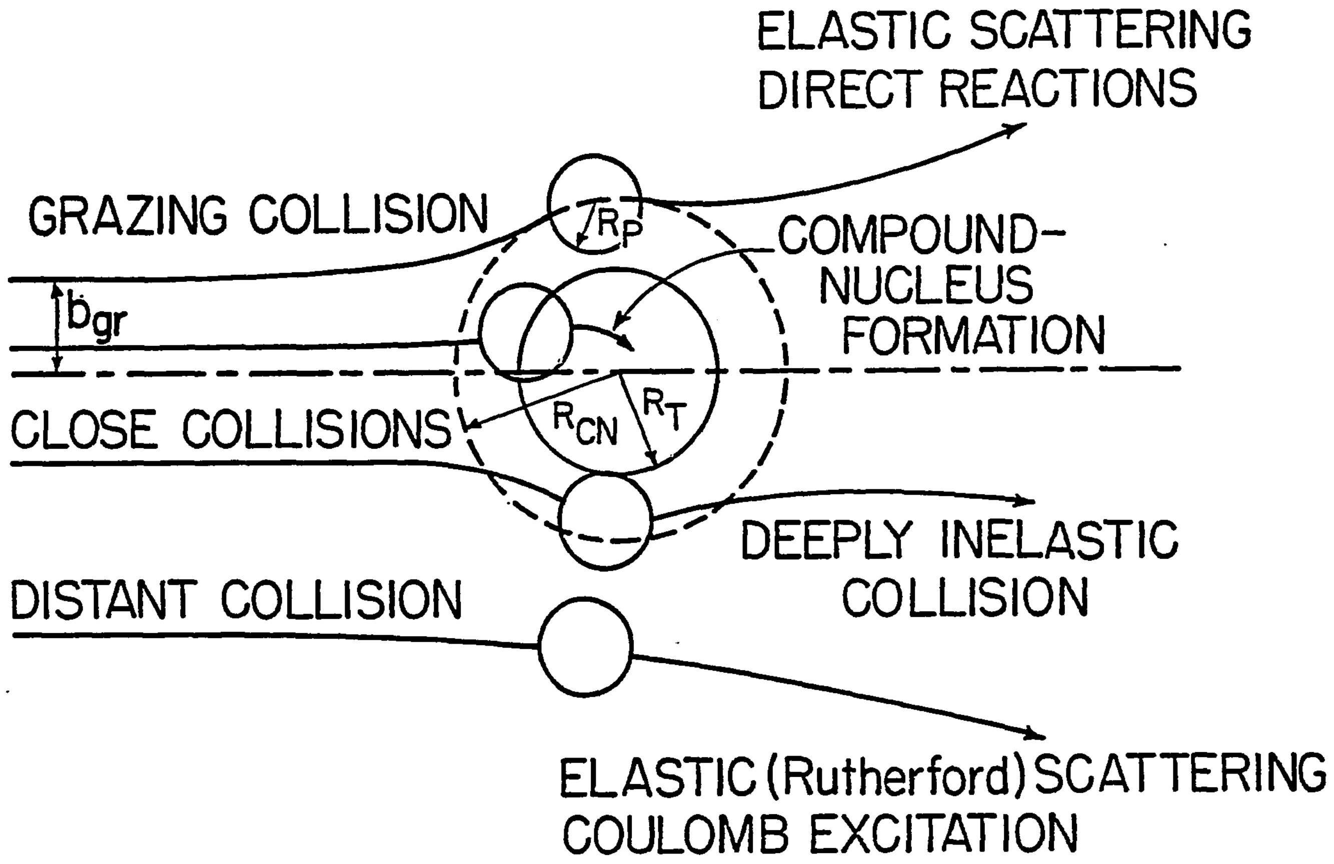

Fig. II.2. Illustration showing the impact parameters for the different nuclear reaction.

The different interaction possibilities can be represented in Fig. II.2. At energies below the Coulomb barrier the ions do not touch and can interact only through the Coulomb field, and this results in elastic Rutherford scattering and possibly non-elastic Coulomb excitation. At higher energies the ions can interact through the nuclear potential, and it then becomes more convenient to classify the interactions according to the impact parameter R_L. If R_L is comparable to the sum of the radii of the ions, a grazing collision takes place, and the ions can be elastically or inelastically scattered or a few nucleons can be transferred from one to the other; these may be referred to collectively as peripheral interactions. When the impact parameter is reduced still further the ions begin to interact very strongly, providing the incident energy is high enough to overcome the Coulomb potential. This happens quite abruptly because the nuclear densities rise very rapidly in the surface region, and the interactions change from those in which a few nucleons are transferred from one ion to the other, with little loss of energy, to the so-called "strongly damped" or "deep inelastic" collisions in which the incident ion loses a substantial fraction of its energy.

At low energies with $R_L << R_1 + R_2$ the collisions will be close or central and lead to the formation of an excited compound nucleus (CN). This is followed, after a time long compared with the transit time, by the evaporation of the CN and emission of one or more particles (or gamma rays) until the residual nucleus reaches its ground state. In the nuclear Fermi gas model (Appendix A) the excitation (E_x) of the CN can be related to a nuclear temperature, T, via the relation $E_x = a(kT)^2$ where a is a nuclear level density parameter and $T = T_{CN} \simeq 5$ MeV for α emission from the CN. Fig. II.3. shows the relative energy spectra of the CN and break-up mechanisms at low and high energies.

The division of nuclear reactions into CN reactions and direct reactions is not a sharp one, as it is possible for the excited nucleus to decay before statistical equilibrium is established[18]. This pre-compound (pre-equilibrium) emission takes place in an early stage of the reaction. Therefore it is usually assumed that the reaction occurs in two stages: a fast stage (*i.e.* an emission in the early stages) or abrasion stage in which part of the nucleons are removed from the region of overlap between the projectile and the target, and a slow stage or ablation stage in which the excited residual (spectator) nucleus is de-excited by emission of particles[19,20] (*i.e.* evaporation). This region of overlap (hot spot, fireball) is a subset of nucleons formed during the collision from both the projectile and target, equalizes and appears as an intermediate hot source of ejectiles with mean velocity roughly half the beam velocity above Coulomb barrier[21]. This fireball decays by emitting fast secondaries or firestreaks.[21,22]

These reactions have been classified according to (although interrelated) the impact parameter, the stage of emission, the energy of the beam, and the mechanism of reactions. For each type of interaction or impact, particular scattering angles are favored, depending on the energy of the interaction[18]. For example, peripheral collisions are detected at small angles whereas central collisions are detected at large angles[1]. Some of these reaction mechanisms such as the CN reactions and transfer reactions are understood much better than the breakup and the breakup-fusion mechanisms. In the intermediate energy range, the projectile velocity is getting so high that the influence of the target on the projectile can no longer be randomized over the entire projectile. Instead, the projectile feels a differential force, the side facing the target getting attracted by the nuclear potential whereas the remainder moves more or less unaffected. Also the long range Coulomb force repels the far side of the projectile. In effect the projectile might simultaneously break up and

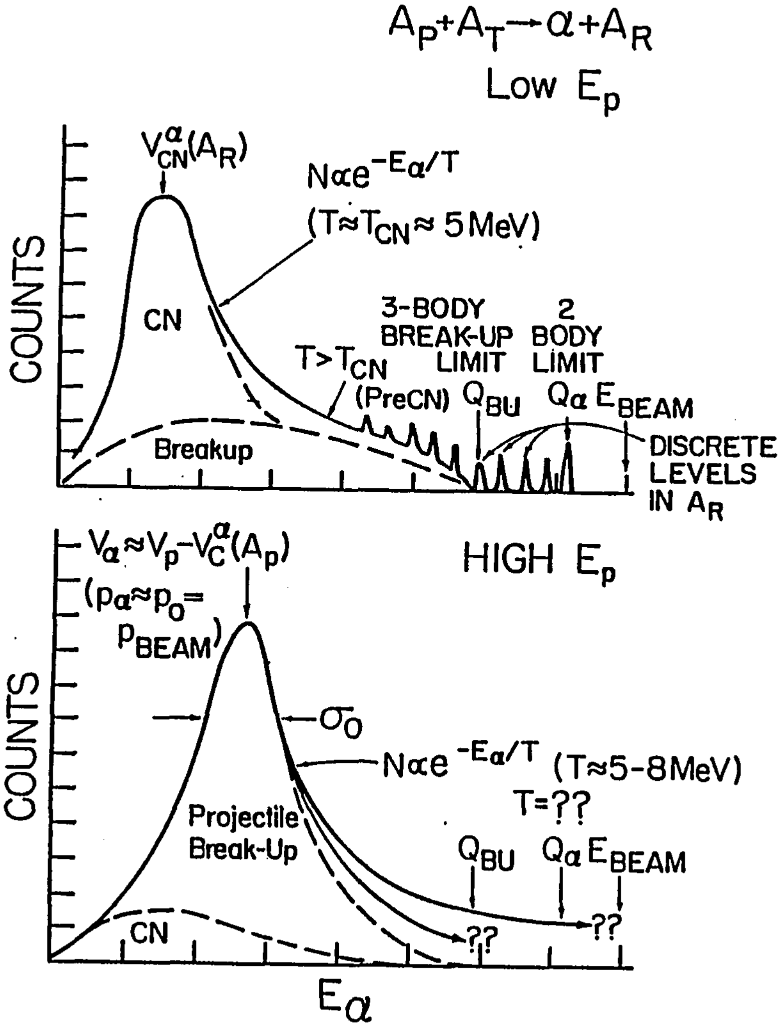

Fig. II.3. Energy spectra for α-particles expected from CN and breakup mechanisms. V^{α}_{CN} is the α-particle velocity in a CN reaction and V^{α}_{C} is the velocity of α-particle due to Coulomb interaction. BU means break-up; A_p is the projectile nucleus; A_T is the target nucleus; A_R is the residual nucleus.

partly fuse with the target[21,23]. It seems that the breakup process is most likely to happen in peripheral reactions, since the short range nuclear force is involved in the process. The observation of emitted fragments having a velocity close to the projectile velocity has been generally interpreted in terms of a projectile fragmentation process[24], *i.e.* the emitted particle is coming from a projectile like source or fragment (PLF). Massive transfer (incomplete fusion or incomplete momentum transfer) or break-up fusion reaction and hot-spot models have been proposed as a simple mechanism for fast light-particle emission accompanied by fusion like residues[23]. Since conservation of energy implies $E_{\text{beam}} = E_{\text{emitted particle}} + Q$-value (Fig. I.4), then it is desirable that the Q-value must be the least negative possible to account for the high energy of the emitted light particles[23].

The above described picture of the break-up fusion process implies a prompt break-up process with two body in the final state *i.e.* the residual part (target projectile fusion like particle) and PLF (Fig. II.1). It is found that the prompt Coulomb breakup is very small and that sequential breakup dominates[22]. In the sequential breakup (Fig. II.1) the target is considered to be a spectator, *i.e.*, a three body final state reaction. In any case the sequential emission of α-particles is unlikely since it is assumed that the energetic α particles are emitted in the early stage of the reaction[23].

The origin of the energetic light ion (LI) particles is thus still largely unknown,[25] and it becomes more complex when considering the 0° degree measurements *i.e.* the most energetic emitted particles. It is not possible to interpret these data by the break-up mechanism alone since it produces in the laboratory particles with energies that are not greatly different from the velocity *i.e.* energy/nucleon of the incident ion.[6,26] Therefore another mechanism must be employed, such as break-up with Fermi motion which includes the nucleon's intrinsic motion inside the projectile, to understand the production mechanism of the LI particles emitted at the high energy tail of the energy spectrum as seen in Fig. II.3.

II.2. Light Particle Spectra in Heavy Ion Reactions

The energy spectra of light emitted particles at a given projectile energy have similar shapes, *i.e.* a smooth bump with an exponential decline on the high energy side. They extend to lower emission energies for increasing detection angle. With larger incident energy, the slopes diminish and the spectra extend towards larger energies. A maximum in cross-section is reached for energies close to that for which the particles have the beam velocity[25].

These properties can be illustrated by the following experimental spectra. Fig. II.4 shows proton energy spectra resulting from the reaction of Sn with 100 MeV/u ^{16}O and Fig. II.5 shows the spectra for $Z = 1, 2$ particles in the reaction of ^{16}O with Ni at three different energies[27]. Although the following remarks are related to protons, it is noticed that the LI spectra are generally similar. At small angles, the cross-sections are observed to peak at energies close to the beam E/A, suggesting peripheral fragmentation as the source of these particles (Fig. II.4.). As the emission angle increases, the fragmentation component decreases in intensity, the spectra acquire an approximately exponential energy dependence characteristic of thermal emisson, and the angular distribution becomes more isotropic. To see this more clearly, Figs. II.4-II.6 show[2,27] angular distribution for α particles emitted in the reactions of ^{16}O with Sn, Ni, Au, Bi at different energies and N with Au. It is noticed that at forward angles $\frac{d\sigma}{dEd\Omega}$ increases with decreasing the emission angle besides it is dependent on the energy and the type of the projectile which again suggests a direct type process. On the other hand, at backward angles, $\frac{d\sigma}{dEd\Omega}$ is

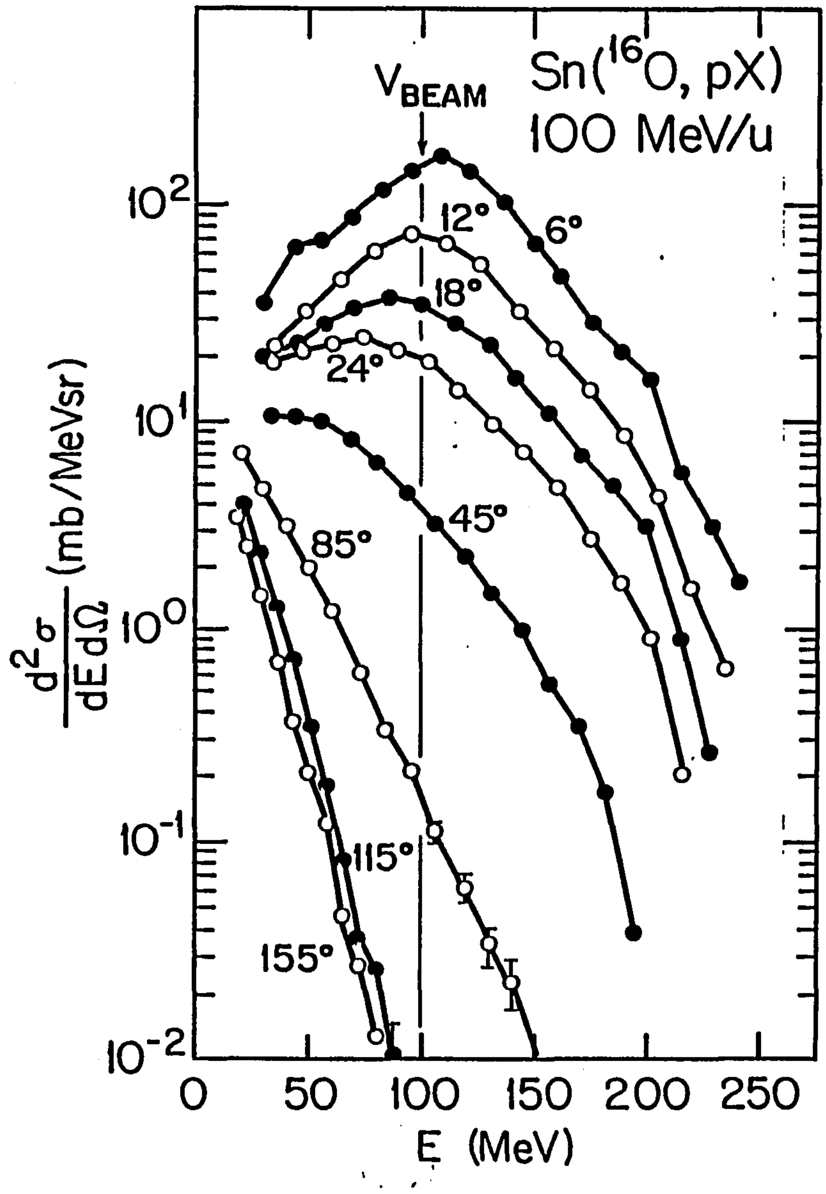

Fig. II.4. Proton energy spectra from the reaction noted (Ref. 27).

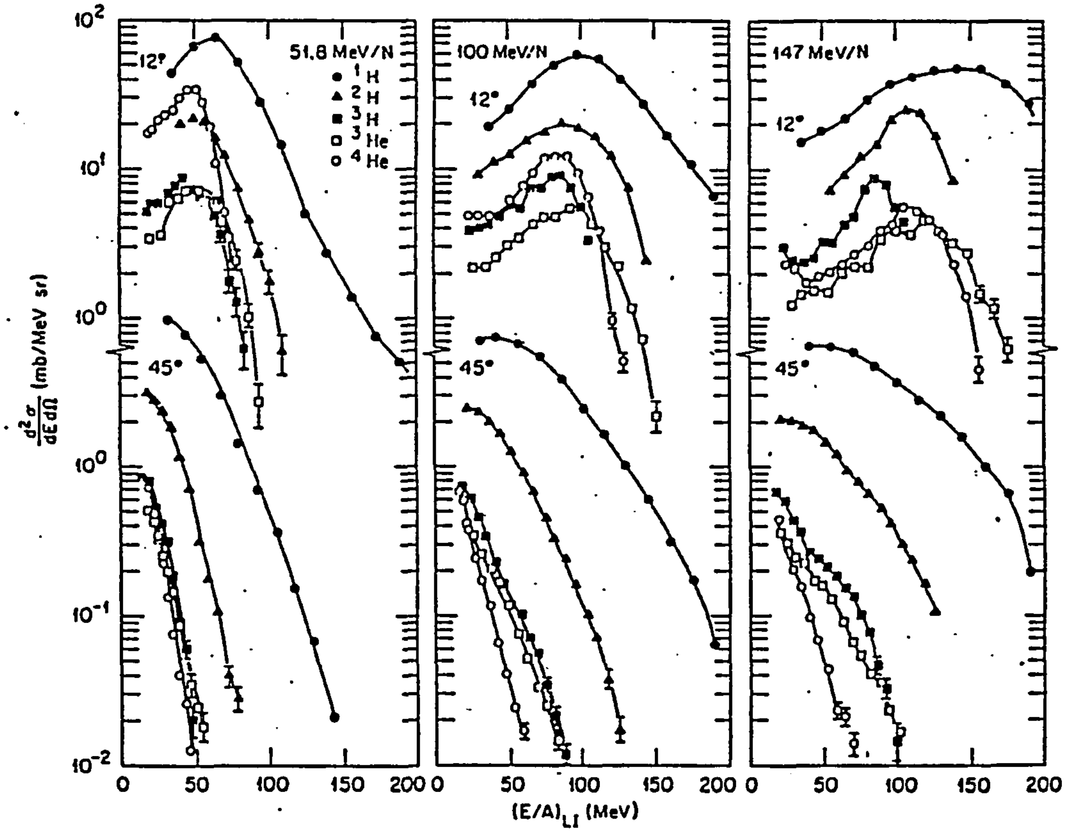

Fig. II.5. Light particle energy spectra from ^{16}O on Ni at three different energies (Ref. 27).

independent on the angle of emission *i.e.* isotropic emission and $\frac{d\sigma}{dEd\Omega}$ depends on the CN excitation energy which again suggests an evaporation process from the compound system. It is also observed that at backward angles energy spectra peak near the coulomb barrier expected for the particle emission from the compound system[27].

Fig. II.7 shows[27] momentum plots of the 6° proton spectra measured for a Ni target at three different projectile energies 50, 100, 147 MeV/u. The solid lines are fits to the data assuming Gaussian momentum distribution of the form $\frac{d^3\sigma}{dp^3} \alpha \exp\left[\frac{-(p-p_0)^2}{2\sigma^2}\right]$ where p is approximately the mean momentum corresponding to the projectile velocity and σ is the momentum distribution width which has approximately the following form for the i^{th} particle with mass m_i,

$$\sigma_i^2 = \sigma_0^2 m_i(m_p - m_i)/(m_p - 1) \qquad \text{II.1}$$

where m_p is the projectile mass and $\sigma_o \simeq 90$ MeV/c. This result is expected for collisions in which the momentum transfer is small[28] in comparison to σ_0. If fragmentation is assumed to abruptly occur early in the collision, then σ_0 can be related to the Fermi momentum p_F of the nucleons in the projectile[28] through the relation $\sigma_0^2 = p_F^2/5$. Alternatively, if one assumes that emission occurs after thermal equilibrium is attained, the width can be related to the nuclear Fermi gas model temperature (Appendix A) of the source by

$$T = \frac{m_p}{m_i(m_p - m_i)} \frac{\sigma_i^2}{m_N} \qquad II.2.$$

where m_N is the nucleon mass [28].

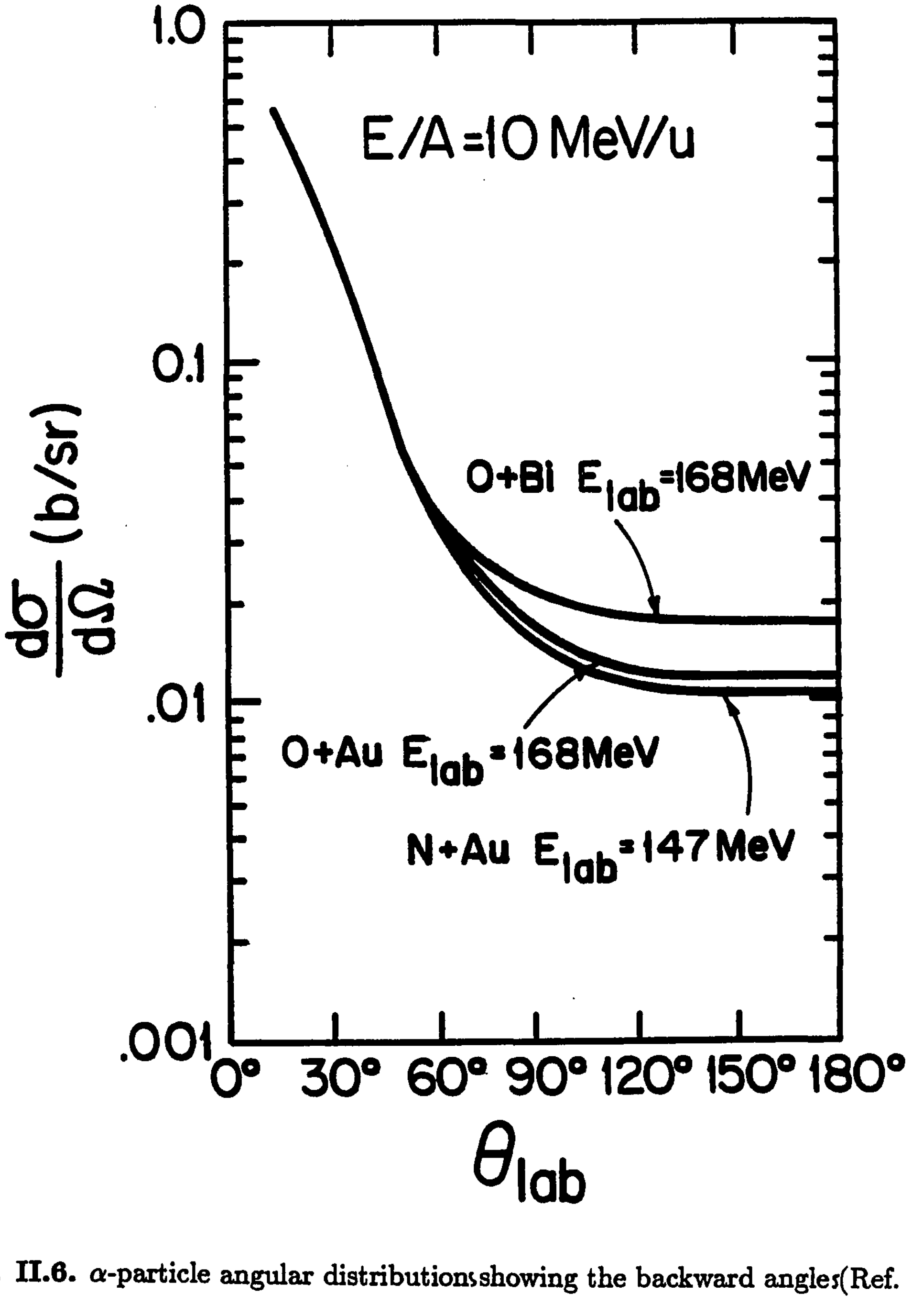

Fig. II.6. α-particle angular distributions showing the backward angles (Ref. 2).

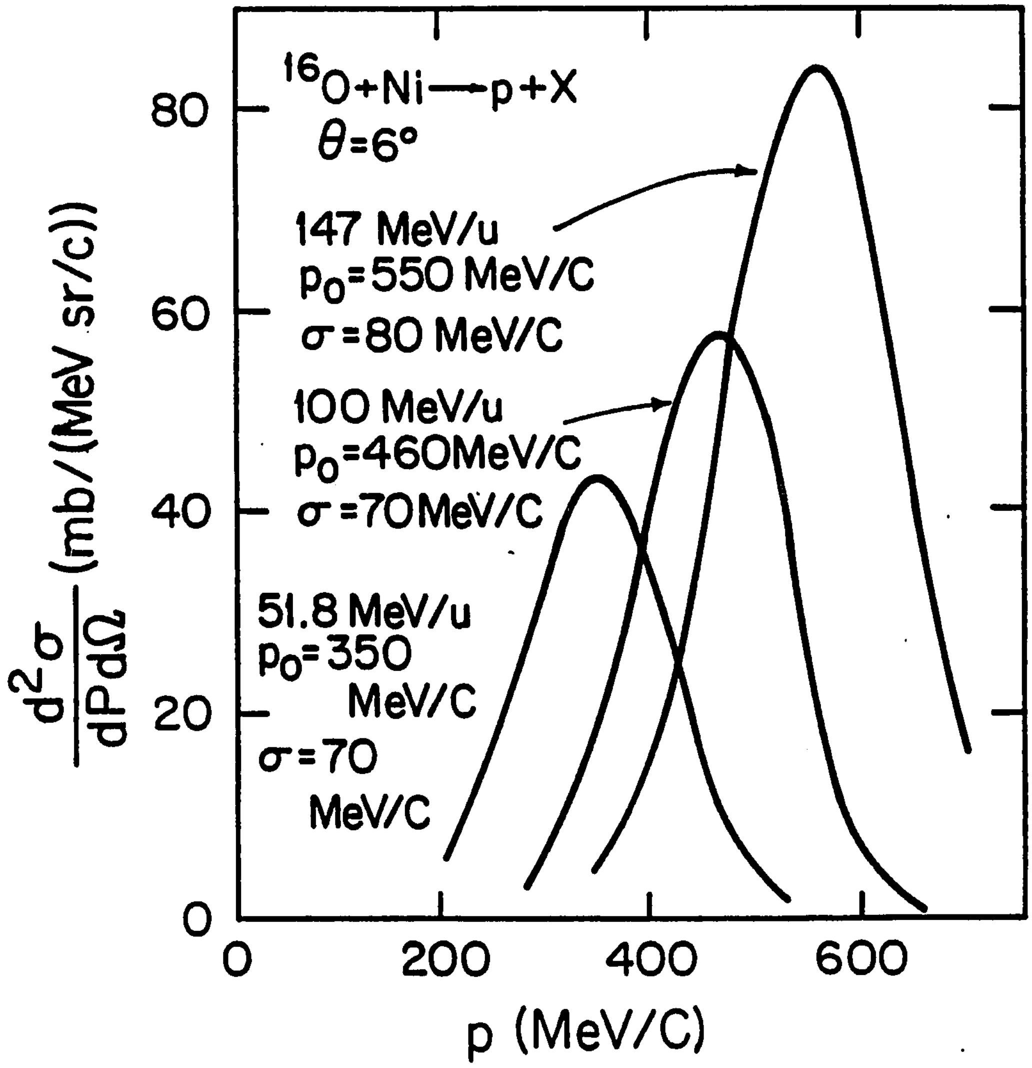

Fig. II.7. Proton momentum spectra in the heavy ion reactions (Ref 27).

These spectra indicate that emission of these particles comes from sources that move with specific velocities and are characterized by a certain apparent temperature, T. Therefore a natural consequence of this is to think about these particles as being emitted from an unknown moving source regardless of the formation mechanism. The phrase "moving source" now is used to denote a general model being widely and frequently used to interpret and fit the spectra of the energetic particles emitted in heavy ion reactions.

II.3. The Moving Source Model

This model assumes that each type of the outgoing particles is emitted from a source characterized by certain values of apparent temperature and velocity. Frequently the spectra are fitted by assuming more than one source for the same particle such as a source for the forward angles and a source for a backward angles. The source is not clearly known. It could mean the projectile, target or their combination. The velocity of the source is not fixed relative to the beam velocity i.e. they could be the same or different.

In its rest frame the source is assumed to emit particles with a Maxwellian distribution of the form

$$\frac{d^2\sigma(E_R,\theta_R)}{d\,E_R\,d\Omega_R} = N_0\sqrt{E_R}\,\exp(-E_R/T_S) \qquad II.3.$$

where E_R is the energy of the emitted particle, T_S is the apparent source temperature or the slope parameter in the source rest frame and N_0 is a normalization constant. It is clear the emission is isotropic in the *source* frame.

If the source moves in the beam direction with velocity v_S (Fig. II.8) then the equation in the laboratory system (see Appendix B) becomes

$$\frac{d^2\sigma(E_L,\theta_L)}{dE_L\,d\Omega_L} = N_0\sqrt{E_L}\,\exp[-(E_L - \sqrt{2mE_L}v_s\cos\theta_L + \frac{mv_s^2}{2})/T_S] \qquad II.4.$$

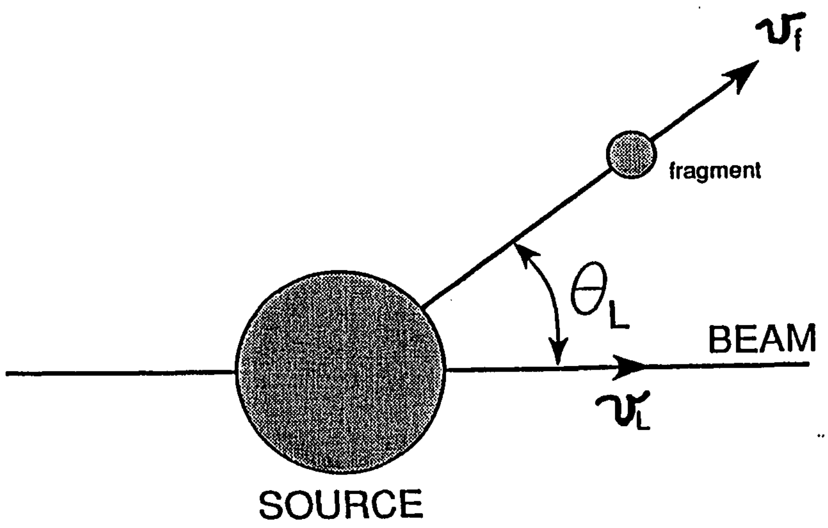

Fig. II.8. Schematic view for the source in the laboratory moving with velocity $v_s = v_L$ in the beam direction. The fragment moves with velocity v_f and makes angle θ_L with respect to the beam direction.

where E_L is the energy of the emitted particle of mass m. However, since charged particles get extra energy $[E_B = Zze^2/R]$ in the exit channel due to Coulomb repulsion from the target residue or the assumed source the value E_L must be approximated as $(E_L - E_B)$ and this equation becomes

$$\frac{d^2\sigma(E_L,\theta_L)}{dE_L d\Omega_L} = N_0\sqrt{E_L - E_B}\exp[-((E_L{-}E_B){-}\sqrt{2m(E_L - E_B)}v_S\cos\theta_L{+}\frac{mv_s^2}{2})/T_S] \qquad II.5.$$

The effect of the Coulomb repulsion is to shift the spectra, a correction sometimes accomplished by adding[26] to θ an estimated angular shift θ_0 due to this repulsion. In any case this correction is only approximate due to the uncertainty of the change of the repelling nucleus.

Thus one can determine the apparent source velocity v_s and temperature T_S (excitation) by fitting the shape and angular distribution of the energetic light particles using equations. II.4 and II.5 with adjustable parameters v_S,N_0 and T_S.

Although Eq. II.5 has been derived for one incident beam energy, i.e. typical for a thin target, one can show[29] that the high-energy portion from a thick, even stopping, target also follows an exponential form with approximately the *same* T_S and T_L. However, unlike thin-target emission, the LI spectra are not necessarily peaked at the beam velocity (Fig. II.3) but may extend to much lower energies since $E_L \rightarrow O$ in the target.

CHAPTER III

THE EXPERIMENT

III.1. The Detectors

As the title of the thesis indicates, the purpose of this experiment is to study the production of very-high-energy light particles. These energetic light ions(LIs) must be stopped in the detectors so that their energy (E) can be measured. Scintillators, which can be made in different shapes and sizes, are suitable for these measurements despite the fact that their energy resolution is the poorest of any commonly used detectors[30]. However, the particle spectra from heavy ion or light ion (HI,LI) reactions are rather continuous and thus do not require good energy resolution. During the course of the experiments several scintillators were used. Table III.1 lists these detectors and their sizes. One of them is BGO or Bismuth Germanate Oxide ($Bi_4Ge_3O_{12}$) which due to its high density and atomic number Z is approximately capable of stopping a 1.3 GeV alpha and a 335 MeV proton as seen in Table III.2. This stopping power (dE/dx) is approximately twice that of NaI(Tl) (as can be seen in Figs. III.1 & 2) and this is the reason why a big NaI detector with a depth approximately twice that of the BGO is necessary to stop the same particles. Figs. III.3 & 4 show the relation between the range of p,d,t,^{3}He, and α in NaI and BGO versus E. The data on p range was taken from a NASA[31]

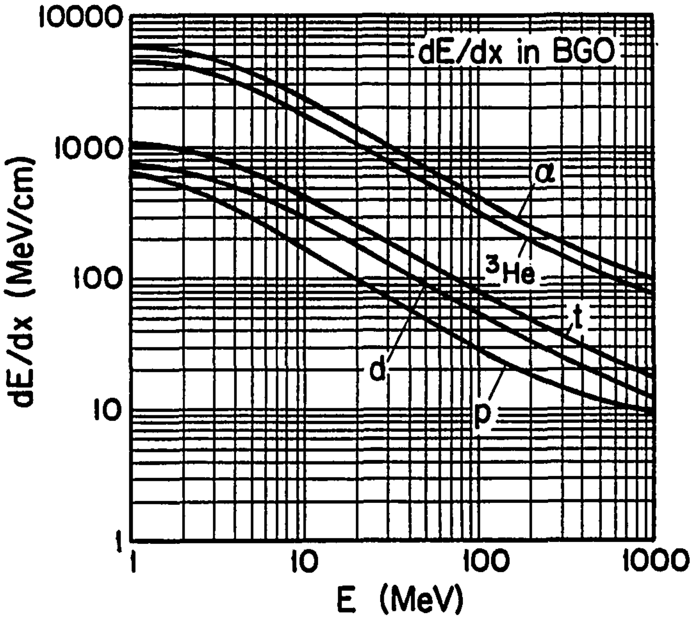

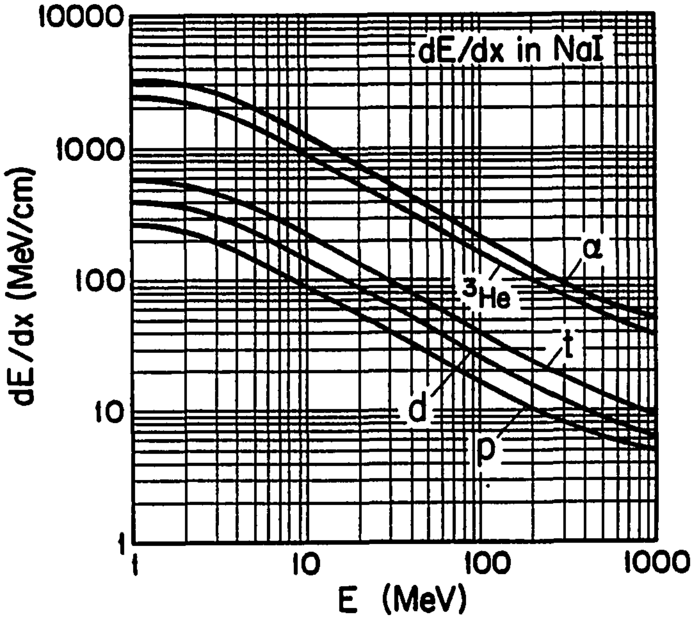

Fig. III.1 (top) and III.2 (bottom): Energy loss of light particles in BGO and NaI scintillators. Data for *p* and *d* were taken from Ref. 32. Other particles were scaled by mass and charge relative to *d*.

Detector number	Detector	Dimensions (cm)	Cross-section shape	Maximum energy (MeV) of stopped particle E_p	E_α
1	BGO	4.3 × 15.2	Circular	335	1335
2	NaI	10.16 × 10.16	Circular	190	757
3	NaI	5.08 × 10.16	Circular	190	757
4	NaI	5.08 × 5.08 × 15.24	Square	220	877
5	NaI	10.16 × 10.16 × 40.64	Square	400	1594

Table III.1. List of the detectors used in different stages of the experiments. For the circular ones, the first figure represents the diameter. The travel path is the longest dimension.

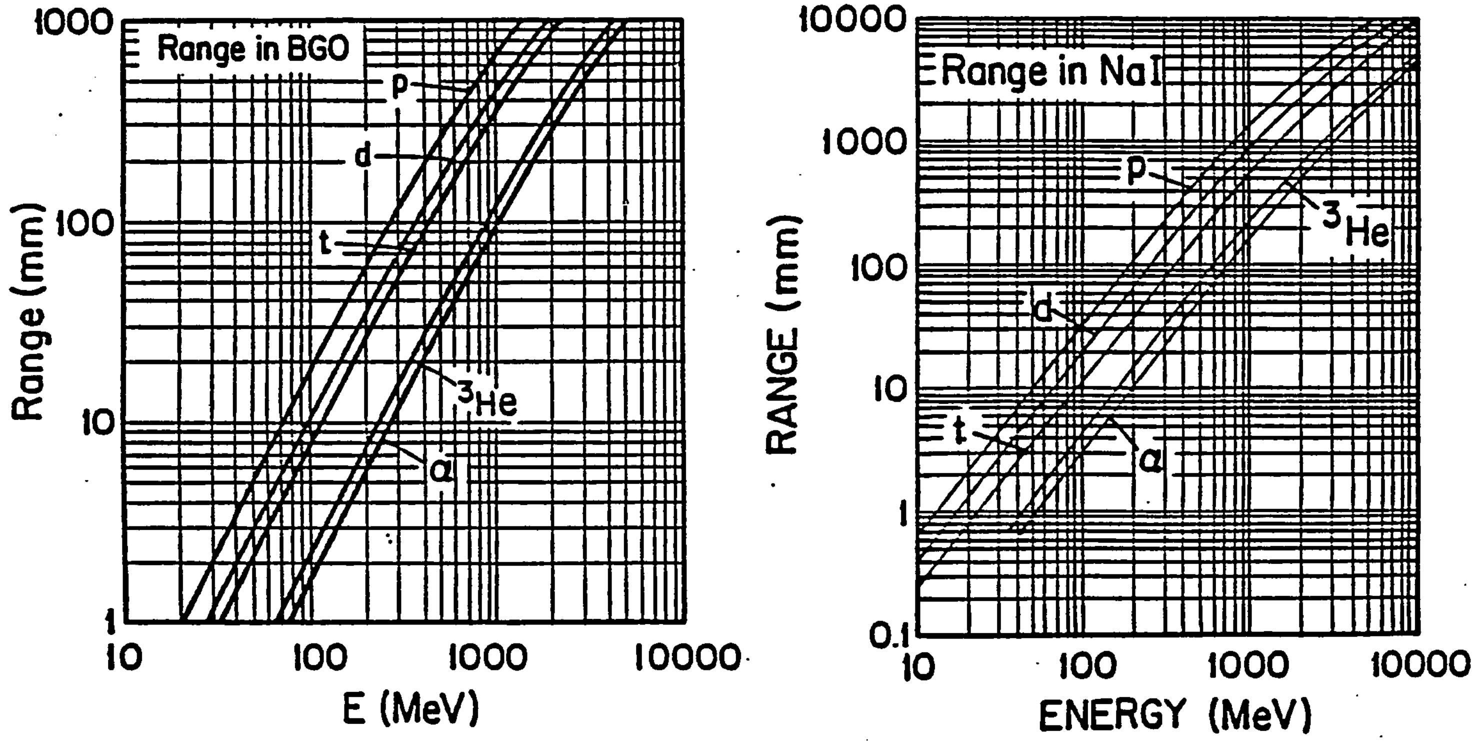

Fig. III.3 (left) and III.4 (right): The ranges of p,d,t, ^{3}He and α in BGO and NaI scintillators.

Property	BGO	NaI(Tl)
Density (g/cm^3)	7.13	3.67
Effective atomic number (Z)	20-30	12
Thickness to stop 90% at 150 KeV x-ray (mm)	2.3	10.4
Hygroscopicity	None	Yes
Refractive index at 480 nm	2.15	1.85
After glow after 3 ms	0.1%	0.3-5%
Wavelength of maximum emission (nm)	480	415
Scintillation cutoff wavelength (nm)	350	320
Wavelength of maximum excitation (nm)	308	
Radiation length (cm)	1.12	2.6
Total x-ray attenuation coeff. at 150 KeV (cm^{-1})	9.98	2.22
Relative light output (pulse height)	10%	100%
Linear coeff. of thermal expansion (25-450°C)	7×10^{-6}/K	47.4 $\times10^{-6}$/K
Temperature coefficient of light yield (1/K)	$-$(1.5-1.7)%	($-$0.2 -0.95)%
Melting point (° C)	1050	651
Typical rise time (ns)	6-8	20-30
Luminescence lifetime (1/e decay constant, μs)	0.3	0.23
FWHM energy resolution for ^{137}Cs gamma ray	12-15%	6.5-7%
Time resolution (ns)	≤ 0.5	≤ 1.5
Resistance to acids, bases, organic solvents	inert	hydroscopic
Hardness(Mho)	5	2
Cleavage plane	none	$\langle 100 \rangle$
Cost	3 (NaI)	1

Table III.2. Comparison between BGO and NaI(Tl) as reported by the manufacturers and some papers (Refs. 16,17, 33).

table for NaI and from a TRIUMF[32] table for BGO. Other particles energies were scaled for the same range by using the following relation[34]

$$\text{Range} \quad \propto \quad \frac{E^k}{M\,Z^2} \qquad (III.1)$$

where E, M and Z are the energy, mass and charge of the incident particle, and $k \doteq 2$. It is clearly seen from these curves that the range in NaI is about twice that in BGO since the latter density is about twice that of NaI. Table III.2 shows a comparison between BGO and NaI. As seen from the table, NaI has better energy resolution (the ratio of the peak full width at half maximum to the peak centroid) whereas BGO has better time resolution. The good energy resolution of the NaI is attributable to the fact that the conversion efficiency[30] of the absorbed incident energy (scintillation efficiency) to light output of the NaI is about ten times that of the BGO. The good time resolution of the BGO is due to the short rise time (light production time in the detector) which is about 6 ns[17].

The detection efficiency (the ratio of the unscattered particles to total number of the incident particles) is different for the different particles in each detector but it is about the same for the corresponding particles in each detector due to the approximately equal geometrical nuclear cross-section in NaI and BGO . It is seen in Fig. III.5 & 6 that the efficiency drops exponentially with the energy and the range (since the range is proportional to the energy). At the same energy, α-particles have the highest efficiency of all due to their short range. The efficiency for p and α is about 55% at $E_p = 300$ MeV and $E_\alpha = 1200$ MeV, respectively, which are about the highest energies measured in the present experiments for these two particles.

Because of the high stopping power of BGO it was mostly used for the small angle measurements. Those NaI detectors which were used at small angles were of large size, a property which is not good for pulse height and timing resolution due

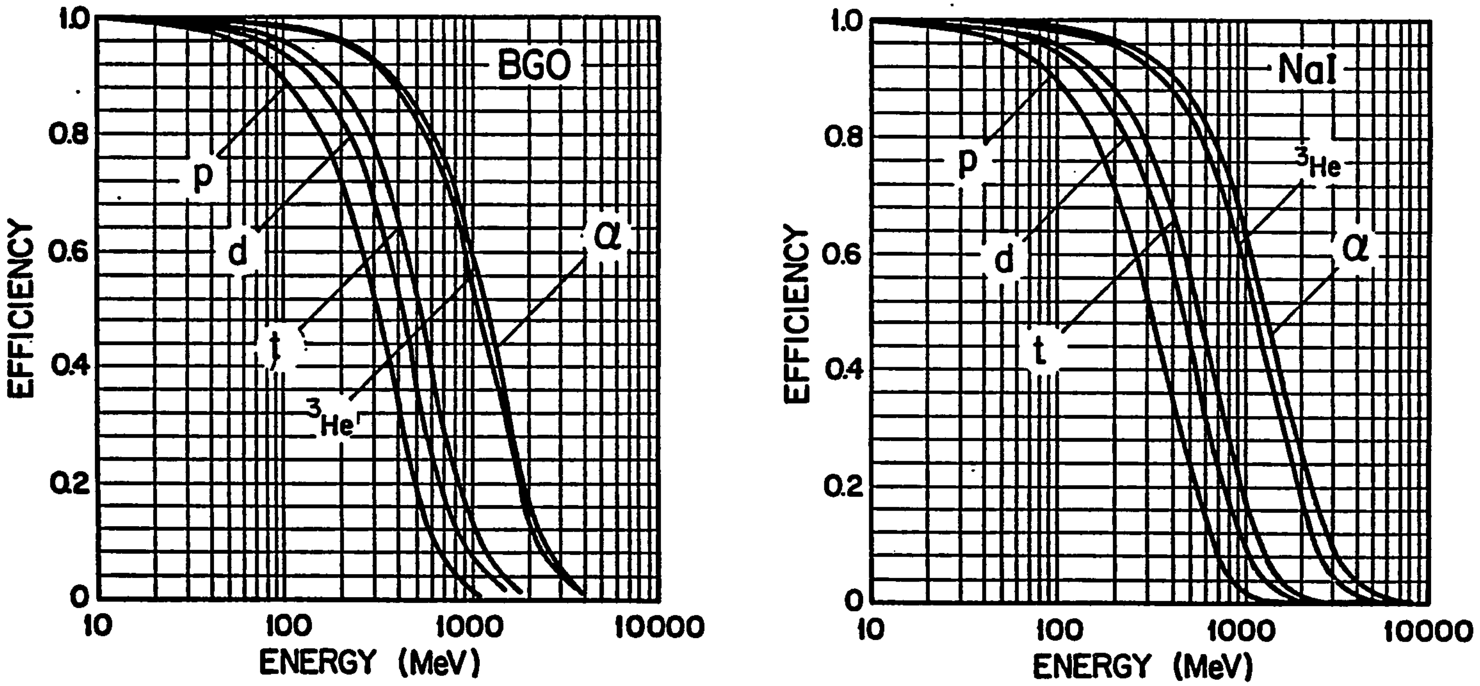

Fig. III.5 (left) and III.6 (right): The detection efficiency for p,d,t, ^{3}He and α in BGO and NaI scintillators.

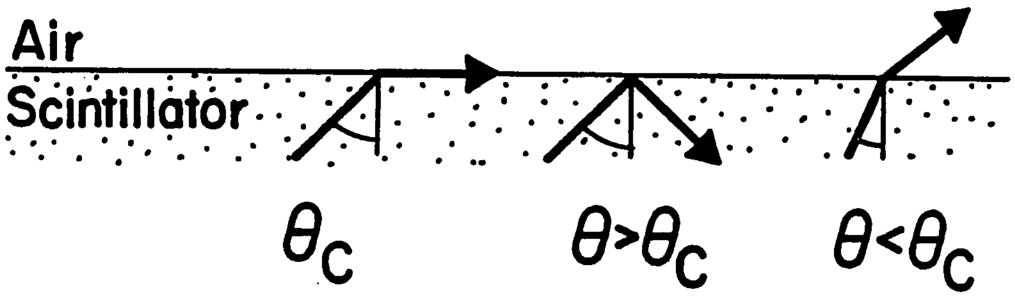

Fig. III.7. The effect of the detector refraction properties on the light collection.

to the imperfect light reflection at the detector surfaces and consequently losses. This results in a nonuniform light collection efficiency and consequently poor[30] resolution. Therefore BGO, due to its compact volume, has a more efficient light collection geometry. In order to keep the light inside the detector, an internal reflection must take place by keeping the critical reflection angle θ_c as small as possible. In Fig. III.7 it is seen that θ_c is given by

$$\theta_c = \sin^{-1} \frac{n_{out}}{n_{medium}} \qquad (III.2)$$

where n_{out} is usually taken as the index of refraction of air. Consequently, since $n_{BGO}(=2.15) > n_{NaI}(=1.85)$, θ_c is smaller for BGO specifically θ_c(BGO) = 27.72° and θ_c(NaI) = 32.72°.

The decay constants of BGO and NaI are comparable(250 ns). Therefore both are suitable for fast counting applications at high energy[16], but as noted BGO has a much faster rise time (6 ns *vs* 20 ns). Also, it is noticed that the range of the useful wavelength of emission for BGO is larger than that for NaI.

Finally , BGO seems to have more practical properties than NaI, such as its hardness, rigidity, chemical neutrality (to acids, bases, water and organic solvents), small linear coefficient of thermal expansion and high melting point.

III.2. The Experimental Set-up

Detection of the emitted particles at zero degree was the most important measurement in all my experiments. Throughout a period of $2\frac{1}{2}$ years, five runs, excluding calibration experiments, were done of which three were only zero degree measurements. Table III.3 gives a detailed summary of these runs. The detectors were numbered in the same way as in Table III.1.

Exp. #	Lab.	Beam	Beam energy (MeV)	Avg. beam current (na)	Det. used	Angle range	Tgt.	Tgt. thickness (mg/cm^2)
1	ANL	^{32}S	306	20	# 1	0°	Ta	203 (beam stop)
2	ANL	^{58}Ni	600	7-10	#1	0°	Ta	407 (beam stop)
3	ANL	^{32}S	450	20	#1	0°	Ta	203 (beam stop)
4	NSCL	^{16}O	480,640	20	#1	0°-35°	Ta,	199 (thin)
								796 (stops 480 MeV)
								1195 (beam stop)
					#2	45°-150°	Cu,	32 (thin)
								859 (beam stop)
5	NSCL	^{40}Ar	800,1200	20	#1	0°-20°	Ta	60 (thin)
								597 (beam stop)
					#5	0°-20°		
					#4	20°-40°		
					#4	40°-100°		

Table. III.3. A summary of the experimental conditions.

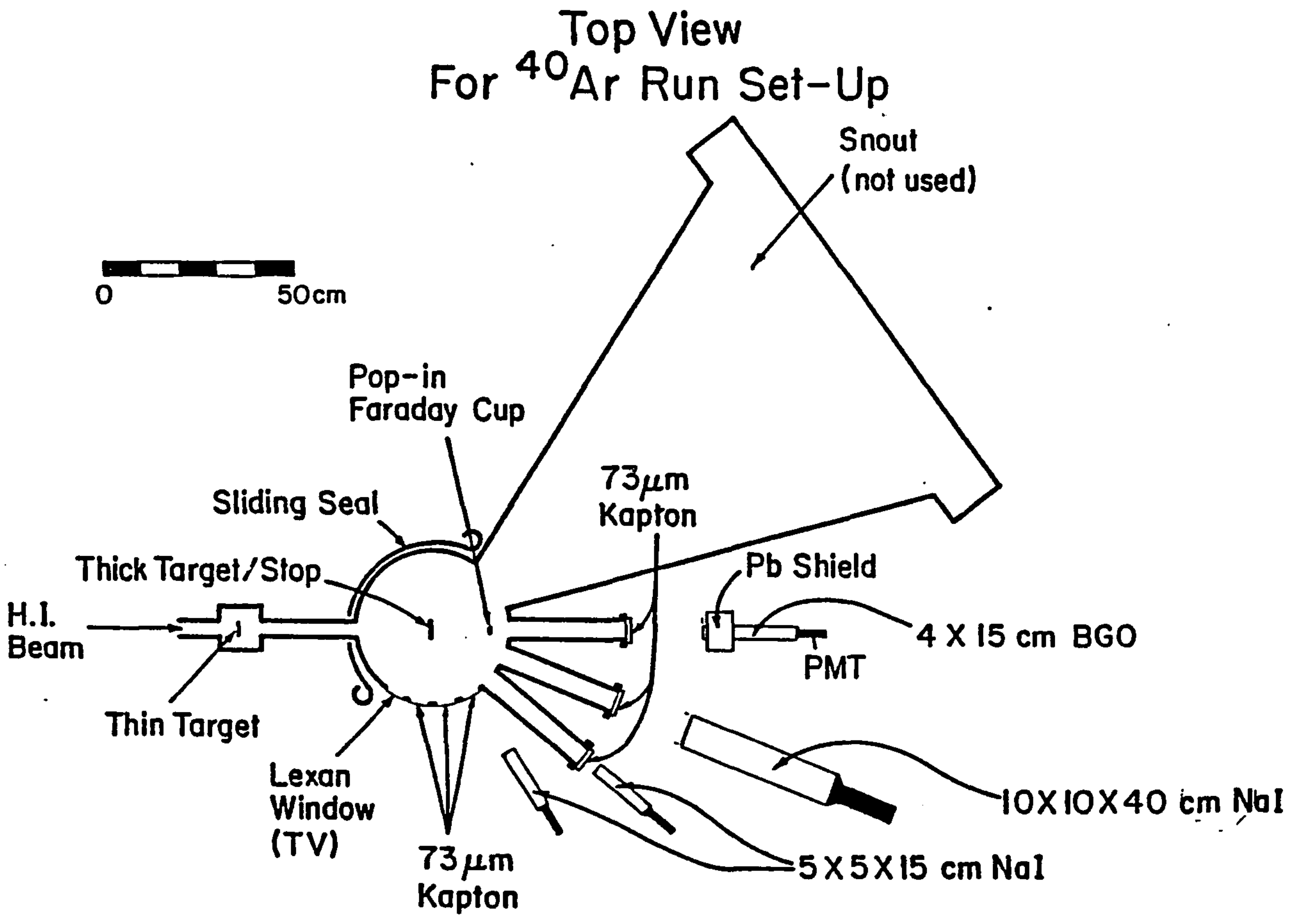

Fig. III.8. Schematic diagram (top view) for the ^{40}Ar run experimental set-up.

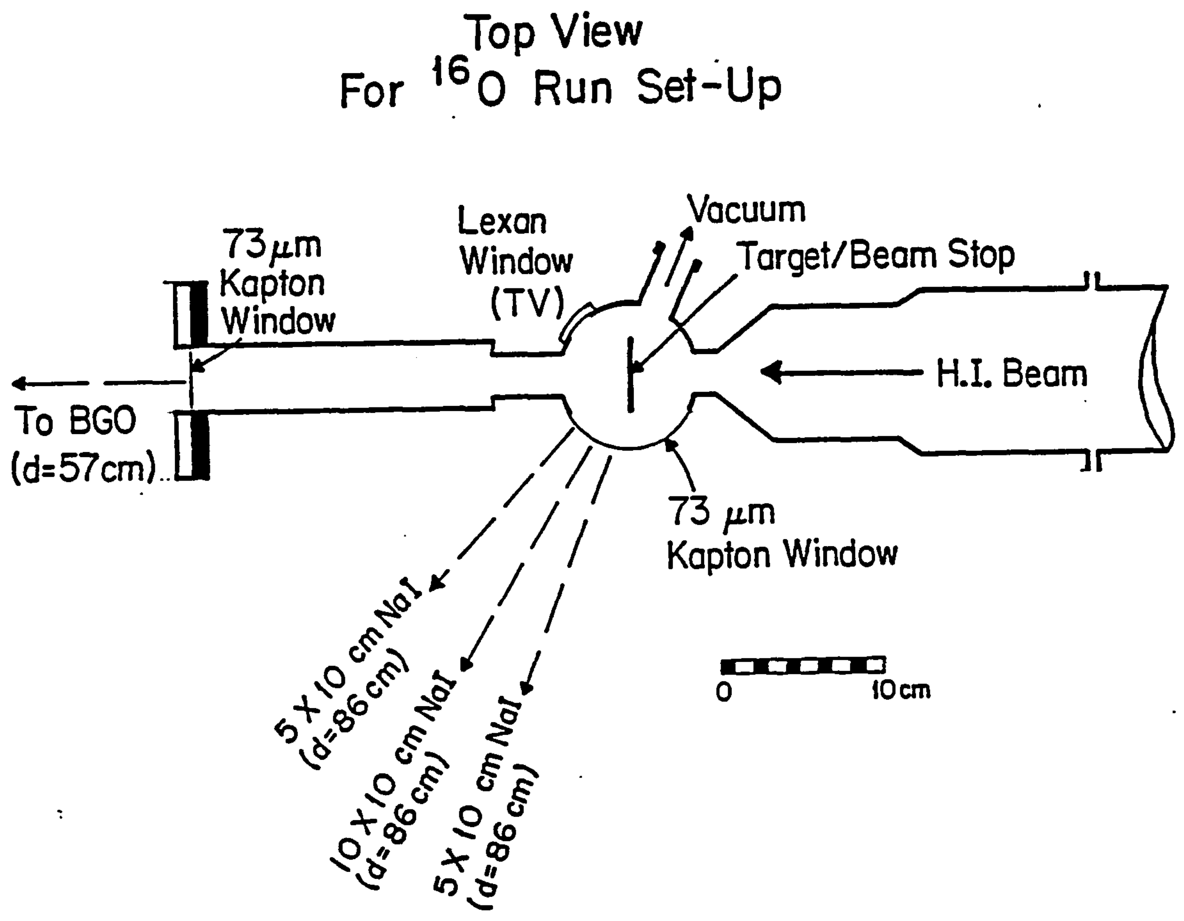

Fig. III.9. Schematic diagram (top view) for the ^{16}O run experimental set-up.

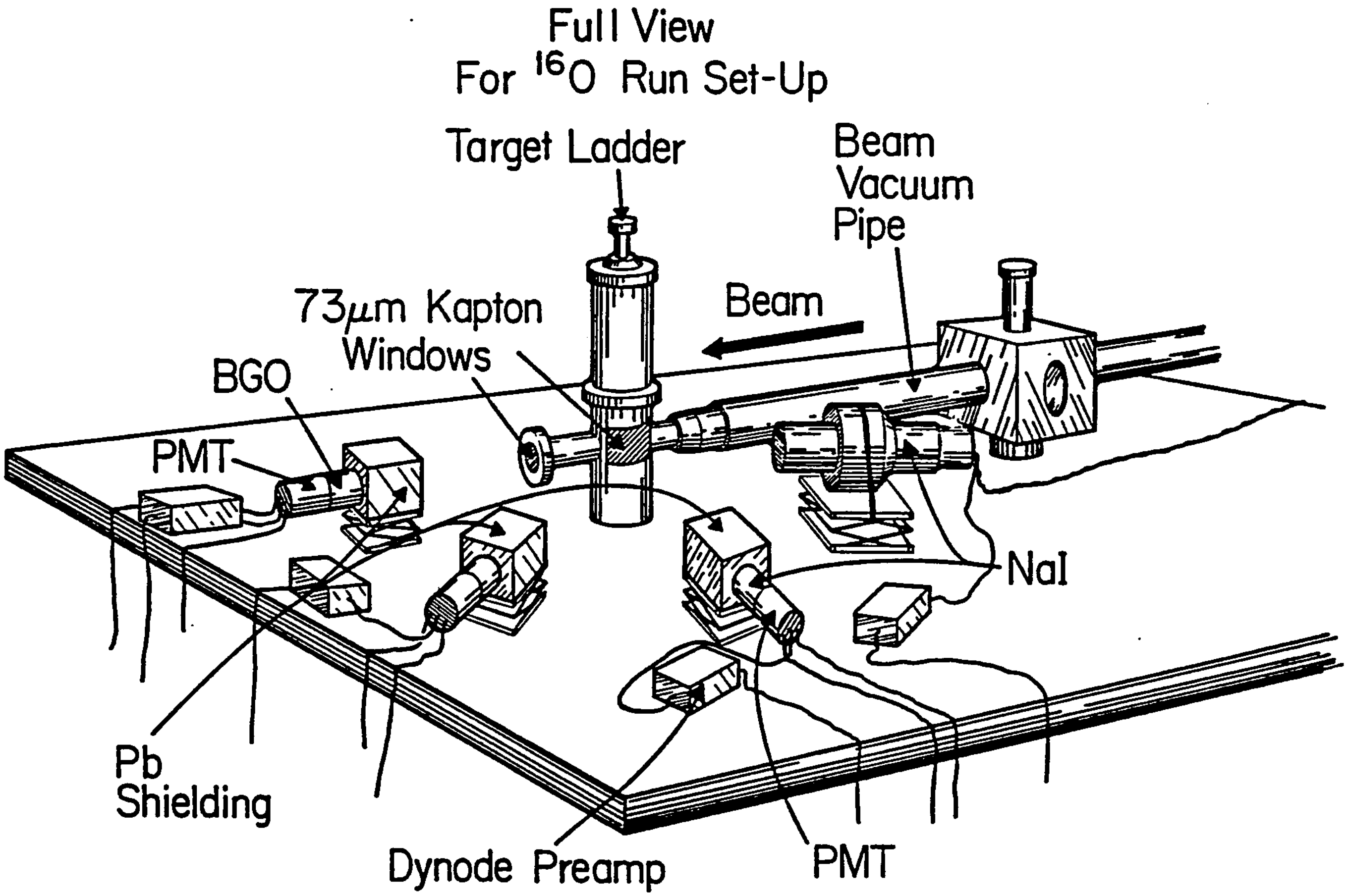

Fig. III.10. Full-view experimental set-up diagram for the ^{16}O run.

Figs. III.8, 9 & 10 show schematic top view set-ups for ^{40}Ar, ^{16}O runs and a full view set-up for ^{16}O run only. Both set-ups were in the S-320 (spectrometer) vault at NSCL. Unlike the ^{16}O scattering chamber, in the moving seal scattering chamber set-up seen in Fig. III.9, targets, targets angles and detectors angles were controlled instrumentally which are more precise.

Both scattering chambers have 73μm kapton windows. In the moving seal chamber there are 7 ports separated by 20°. Each port covers an angle of $9\frac{1}{4}^{\circ}$. Most of the time the thick target serves as the Faraday cup, i.e., it stops the beam. When a thin target is used an external Faraday cup can be attached to the 0° port or an internal pop-in 5° cup can be used. The thin target and the thick are 50 cm apart.

The detectors were positioned in a wide angular range and shielded by Pb collimators. A fast PMT was attached to each detector to collect the light output. A Lexan window was used for the TV camera to monitor the target.

III.3. Particle Identification Methods

In nuclear reactions many different particles are produced. These particles must be identified in z and m since this is important for both the calibration of the detectors and as well for the reaction study itself. The type of the particles which can reach the detector depends on its energy, mass, the incident ion energy, and the target thickness. If the target is thick enough to stop the beam, then only light particles (proton, ..., alphas) will have enough energy to come out. On the other hand, if the target doesn't stop the beam, other massive particles may hit the detector. In any case, it is always possible to discriminate the unwanted particles by setting the energy threshold high.

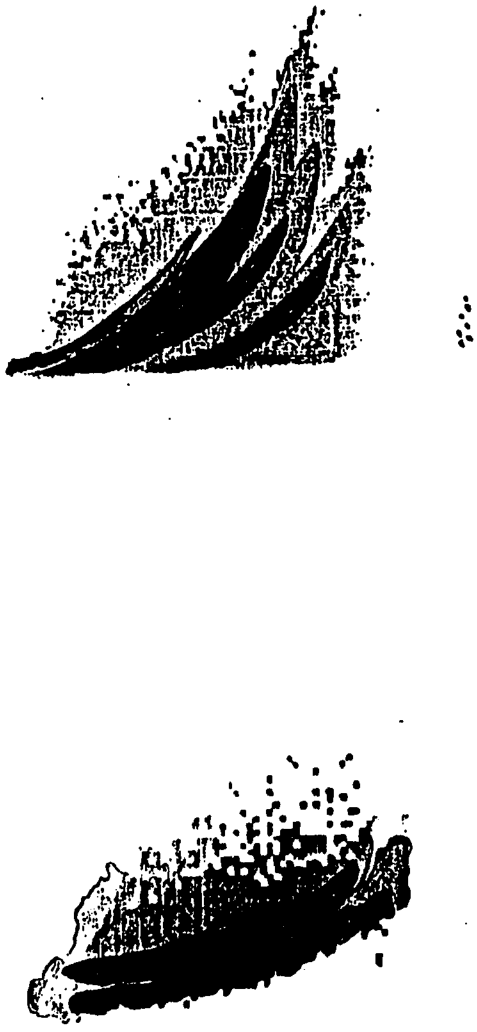

Fig. III.11. TOF (horizontal) *vs.* $\mathcal{L}$ (vertical) plots from BGO (top) and 10 × 10 × 40 cm NaI (bottom).

There are three identification methods well known in the field of heavy ion collisions. These are the Time of Flight (TOF), the Pulse Shape Discrimination (PSD), and the Energy Loss in Absorbers (ELIA) methods. Unless it is necessary due to background to confirm the identification, one method is usually enough. In Appendix C short conceptual descriptions of TOF and PSD methods are given. Fig. III.11 shows some typical TOF *vs.* scintillator light ($\mathcal{L}(m, z, E)$) plots in the BGO and NaI detectors. As is seen in the BGO plot, there are five bands representing gamma rays, protons, deuterons, tritons, and alphas. Gamma rays are taken to be the zero time. Except for the tritons and alphas, these particles are arranged in reverse order because the start and stop signals are reversed. The reason that tritons and alphas aren't ordered in the same way is the non-linear light saturation of the scintillator with the higher z which means a shorter range, *i.e.* alphas give less light than tritons at the same E. This situation disappears in the TOF vs. energy plot. As noted, the BGO detector is known for its ability to give a very good TOF since the time resolution of the BGO is $\leq$ 0.4 ns. The flight paths in these different experiments range from 36 cm to 150 cm. The relativistic TOF's are calculated by the equation

$$TOF = \frac{d}{c}[1 - \frac{1}{1 + \frac{E}{mc^2}}]^{\frac{1}{2}} \qquad (III.3)$$

and plotted for p, d, t, ^{3}He, and α particles in Fig. III.10. In the equation d is the flight path, c is the speed of light, and E & m are the energy and the mass of the particle.

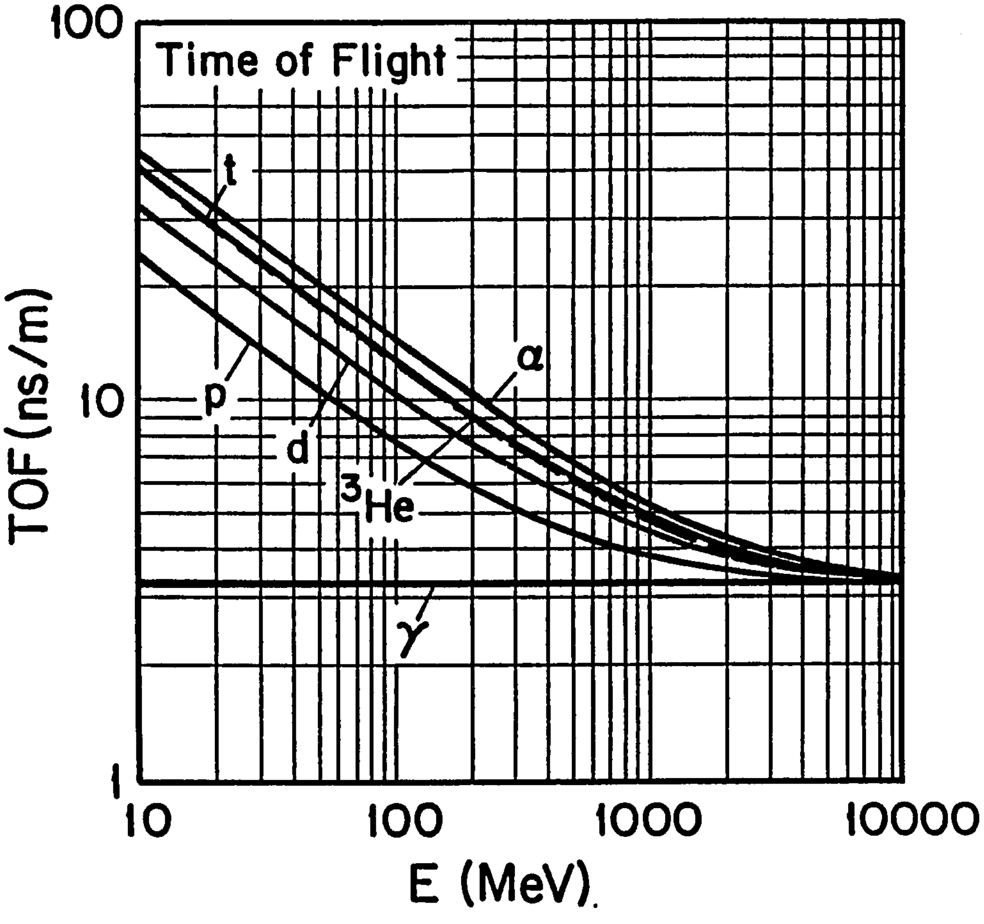

Fig. III.12. TOF curves for p, d, t ^{3}He and α particles.

Fig. III.13. TOF (horizontal) *vs.* $\mathcal{L}$ (vertical) plots from BGO (top) and 10 × 10 × 40 cm NaI (bottom) with thin and thick Ta targets separated by 50 cm.

Fig. III.14. TOF (horizontal) *vs.* PS (vertical) plots for 5 × 5 × 15 cm NaI (top) and 10 × 10 × 40 cm NaI (bottom) from thin (front) and thick Ta targets separated by 50 cm.

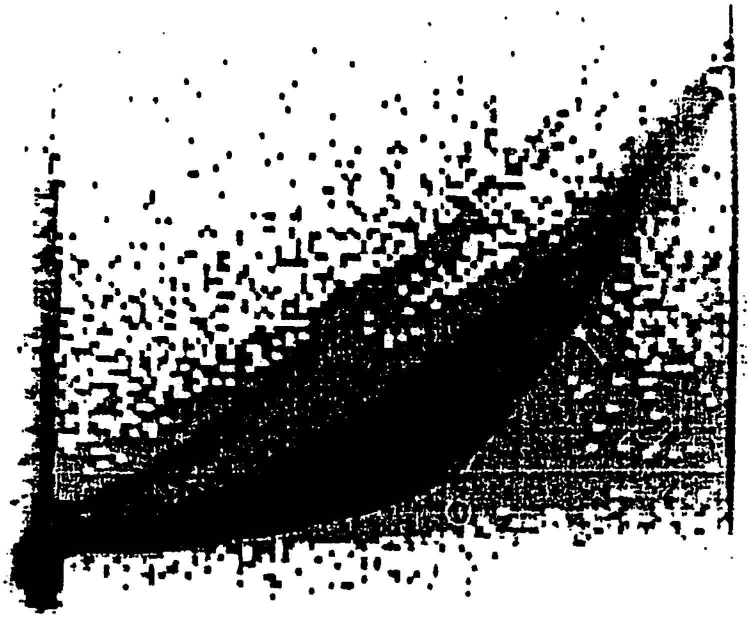

Fig. III.15. PS (horizontal) *vs.* $\mathcal{L}$ (vertical) plot from a 5 × 10 cm NaI.

On the other hand NaI detectors have a better PSD due to their long rise time as seen in Fig. III.14. In the TOF *vs.* PSD plot, the particles are ordered sequentially according to the mass with p, or the faster particle, being the upper band and α, the lower one. In the PSD *vs.* $\mathcal{L}$ plot, Fig. III.15, t and α interchange places for the same reason as explained previously.

Pile-up of simultaneous, coincident events in a single detector can usually be rejected by $\mathcal{L}$ *vs.* TOF since these events fall outside the true mass band (Fig.III.11) and appear as background.

Figs. III.13 and 14 shows the thin (front) and thick Ta targets TOF *vs.* $\mathcal{L}$ and PS plots. These targets were separated by 50 cm. Since the thick target is closer to the detectors, its particles come earlier in time. It is noticed these spectra are very similar but the thin target bands are more intense. Since the projectile energy is much higher in the thin target ($E \doteq E_{beam}$) than in the second, thick target ($E = E_{beam} - \Delta E_{thin}$ to 0), this implies that the 0° cross-sections are higher for higher projectile energies.

Block diagrams for typical analog and logic circuits are given in Fig. III.16. An alternative PSD circuit using discrete modules is seen in Fig. III.17. The $\mathcal{L}$ signal is usually the dynode signal(to avoid PMT saturation) whereas the PS and time signal are usually taken from the anode.

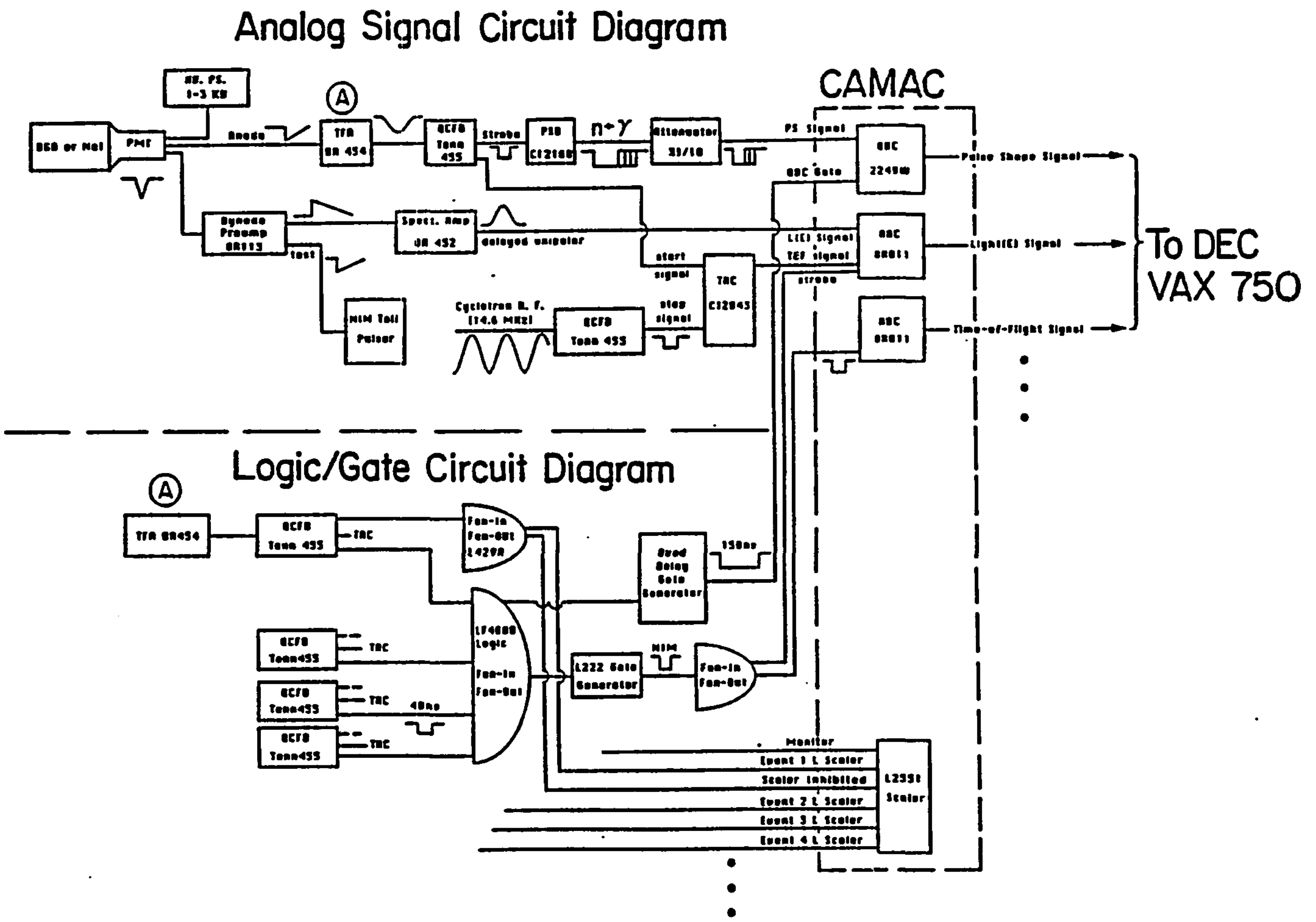

Fig. III.16. The analog signal circuit diagram used in the ^{40}Ar run.

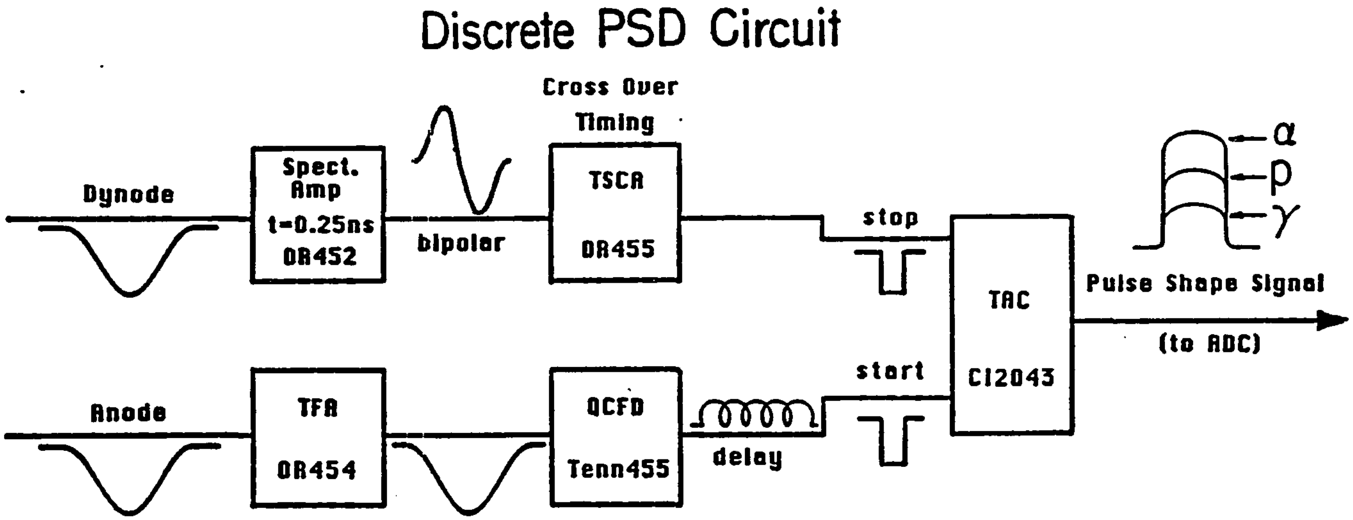

Fig. III.17. The discrete PSD circuit diagram used in the ^{16}O run.

III.4. Energy Calibration of the Detectors

As their name indicates, scintillators emit light($\mathcal{L}$) when they interact with radiation or ionizing particles. The relation between the light output and the corresponding ion's mass, charge and energy is known as the energy calibration, $\mathcal{L}$ (m, z, E). Unfortunately, due to the non-linearity of this relation, it is not accurate to extrapolate $\mathcal{L}$ to the high energy range without having data in that energy range. However this requirement is limited by the availability of high-energy ions.

This calibration process was carefully done several times by using several ion and γ-ray sources for different energy ranges: low, intermediate, and high. At the low energy range ($E < 10$ MeV), γ-ray sources with energy ranges from 0.511 to 7.6 MeV (Table III.4) were the only convenient sources available. Among these is ^{22}Na which was used frequently for its distinguished and resolved energy peaks at 0.511(a) and 1.274(b) and the sum peak (c) at 1.79 MeV as displayed in Fig. III.18.

At the intermediate energy range (E = 10-100 MeV), cosmic-ray μ-meson energy signals were identified in all detectors as seen in Fig. III.19. The corresponding ΔE values in all the detectors were then calculated using the previous γ-ray calibrations. These values were confirmed by comparison with

1) the μ energy-loss calculation for BGO and the NASA[31] data on NaI (Fig. III.18). Using these curves, ΔE_μ for the different scintillators was calculated at minimum ionization ($dE/dx\times$ detector thickness) as seen in Table III.5. ($dE/dx|_{BGO} \sim 9$ MeV/cm and $dE/dx|_{NaI} \sim 5$ MeV/cm at minimum ionization.)

2) Monte Carlo simulation by using the BNL (Brookhaven National Laboratory) program[35] (Table III.5).

Source	**γ Energy (MeV)**
^{22}Na	0.511
	1.274
^{137}Cs	0.662
^{54}Mn	0.835
^{88}Y	0.848
^{60}Co	1.173
	1.1332
^{228}Th	2.26
PuBe	4.43
	7.6

Table III.4. Gamma ray sources used to calibrate the detectors. The PuBe lines come from the reaction ^{4}He + ^{9}Be $\rightarrow ^{12}$C* +n, where ^{12}C* goes to the ground state by emitting the gamma ray listed.

Detectors	Detector dimensions (cm)	ΔE_μ (MeV) Monte Carlo	ΔE_μ (MeV) (estimated)	ΔE_μ (MeV) Experiment
BGO	4.3 dia. × 15.2	39.6	38.7	36±3
NaI	10.16 dia. × 10.16	51.7	50.8	50.3±12
NaI	5.08 dia. × 10.16	25.04	25.4	25.1±4.8
NaI	10.16 × 10.16 × 40.64	48.1	50.8	49.6±8
NaI	5.08 × 5.08 × 15.24	29.9	25.4	12±0.7

Table III.5. μ-meson peaks in the detectors as determined by Monte Carlo simulation[35], estimates from dE/dx, and the experimental values.

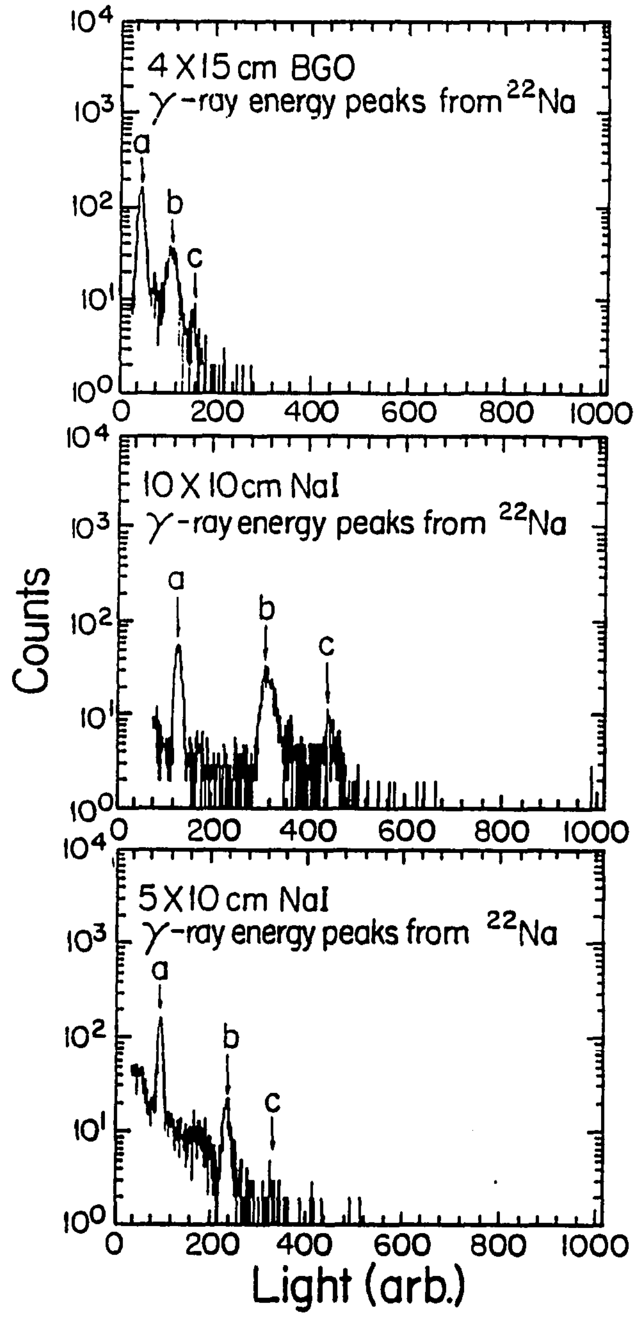

Fig. III.18. γ-ray signals from ^{22}Na in BGO and NaI detectors.

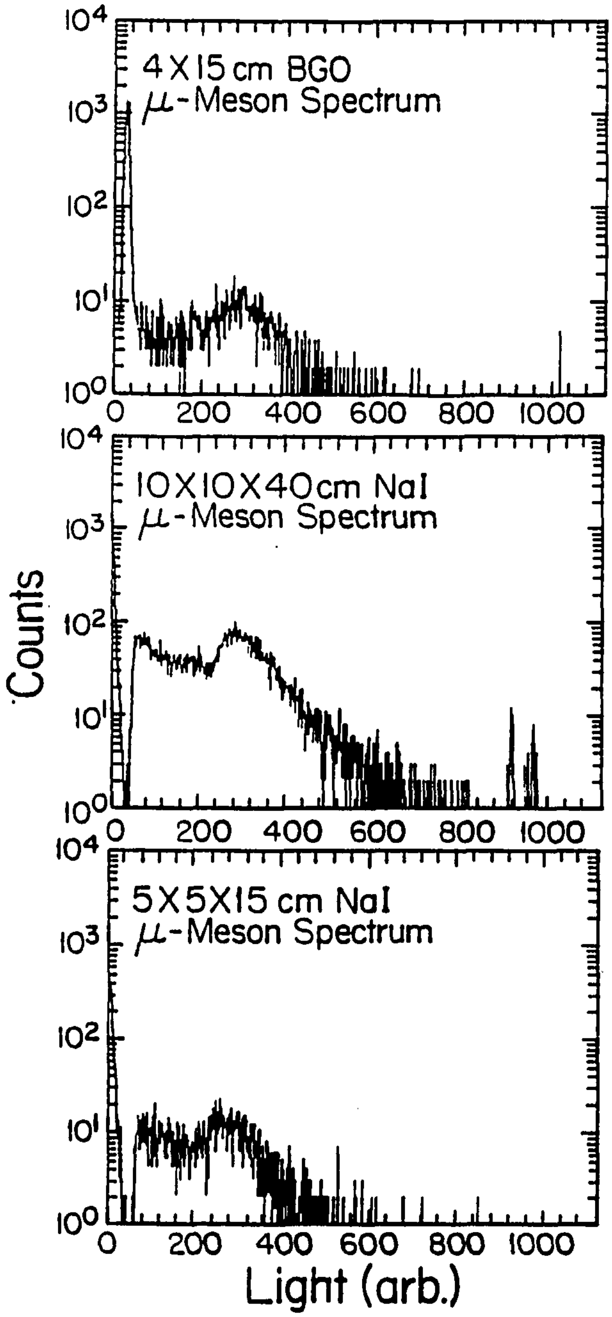

Fig. III.19. μ-meson signal in BGO and NaI detectors.

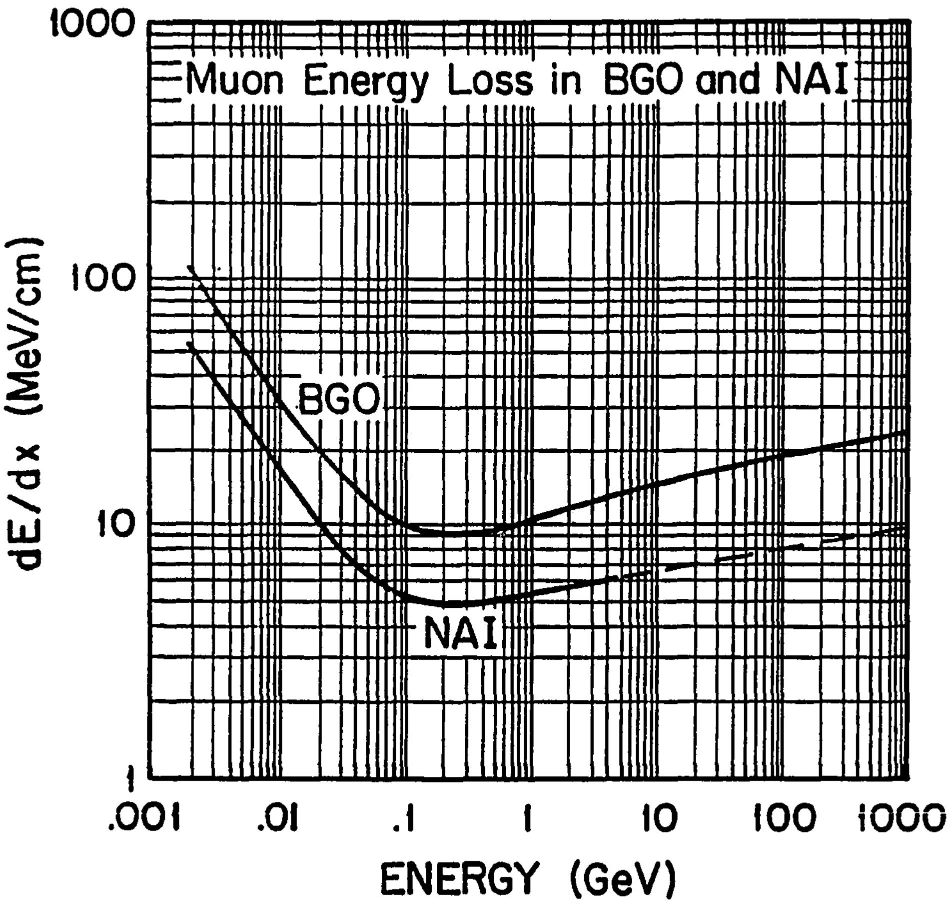

Fig. III.20. Calculated μ-meson energy loss in BGO and NaI detectors.

As is seen from the curves and tables, these three different methods are in good agreement except the last one.

Both γ-ray and cosmic μ-meson calibrations were performed several times throughout the experiments to establish consistency and stability of the calibration. It is evident to say that μ mesons provide a distinguishing calibration point for each detector. This is because the ionization of the μ is almost constant(minimum ionization) as seen in Fig. III.20. At minimum ionization, both NaI and BGO give a similar value for dE/dx of about 0.4 MeV cm^2/gm. Since μ-mesons are the penetrating component of cosmic rays, they are produced in the decay of the π meson. Measurements at the sea level show that the number of μ-mesons is reduced by 50% after passage through one meter of lead. These particles therefore cannot be nucleons, whose mean free path would be much shorter.

At high energy($E > 100$ MeV), accelerator ion beams of 201 MeV protons and 270 MeV ^{3}He at TRIUMF (VanCouver, B.C. Canada) and IUCF (Indiana University Cyclotron Facility) respectively were employed with various targets. Only the BGO detector was calibrated at TRIUMF while the BGO, #2 and #3 NaI detectors were calibrated at IUCF. In order to get several calibration points the detectors were placed at different scattering angles and more importantly scattered reaction products passing through different stages of absorbers were measured. Kinematics confirmed the observation of inelastic protons,deuterons and elastic ^{3}He in the IUCF runs, but only completely elastic protons were observed at TRIUMF. In addition to these new calibration data earlier BGO calibrations[17] were also utilized ($E < 200$ MeV) which checks well for protons.

Fig. III.21 shows the calibration curves for BGO, normalized with respect to average of the .511 and 1.274 MeV lines of ^{22}Na to eliminate the photomultiplier

Detector	Energy range (MeV)	Energy ratio at same $\mathcal{L}$: E_p/E_γ	E_d/E_γ	E_t/E_γ	$E_{^3He}/E_\gamma$	E_α/E_γ
BGO	10-500	1.284	1.32	1.36[a]	1.4	1.54[a]
NaI(Tℓ)	10-500	1[b]			1.08	1.1[b]

Table III.6. Adopted energy ratios of different particles relative to extrapolated γ-ray energy for the same light output, $\mathcal{L}$. (a: Ref. 36; b: Ref. 37)

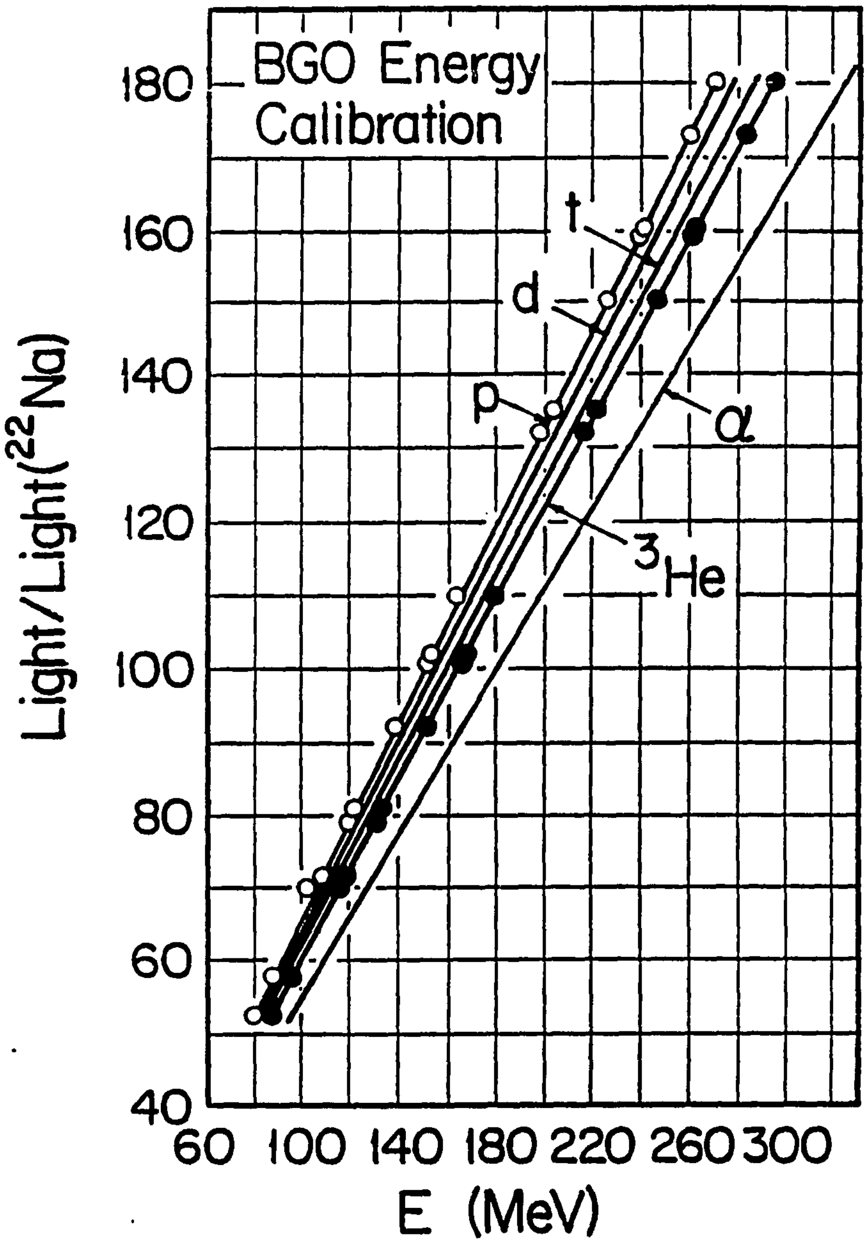

Fig. III.21. BGO energy calibration for light particles. Points represent experimental data (Table III.6).

voltage dependence. Only p, d and ^{3}He have experimental data for BGO and only ^{3}He for NaI. Other values were adopted from Refs. 36 and 37. The ion energy is found to be directly but (non-linearly) proportional to the $\mathcal{L}$ channel number and inversely to the gain (coarse x fine). These curves were fitted by a logarithmic relation of the form $\mathcal{L} = b_i E^{0.9945}$. The coefficients b_i have the following values: $b_p = 0.687$, $b_d = 0.667$, $b_t = 0.648$, $b_{^3He} = 0.63$ and $b_\alpha = 0.573$. Since b_i is light per energy unit, it is expected that its value decreases with particle mass as can be concluded from the light saturation with heavier masses.

Finally, it is noticed that the PMT anode can easily saturate at high energy, therefore giving a lower $\mathcal{L}$ value. On the contrary, an early dynode signal does not saturate so easily so it is used for the energy signal throughout this work.

CHAPTER IV

DATA ANALYSIS AND RESULTS

In Chapter II, theoretical models, including the moving source model, were introduced. In this chapter I will present my experimental data and a theoretical analysis based on the moving source model.

Experimental data will include the energy spectra from the thick and the thin targets, angular distributions of emitted light ions, the relative yields and multiplicity for the different light particles, and the deduced moving source temperatures and their relation to E_{beam}/A.

The experimental cross-sections were calculated according to the equation

$$\frac{d^2\sigma}{d\Omega dE}\,(\mu b/sr/MeV) = \frac{NGcos\phi_t A_t\,(2.65\times 10^{-4})}{(\rho x)(d\Omega)(Q/q)(d.t.c.)(E/ch)_\gamma(E_i/E_\gamma)} \qquad (IV.1)$$

In the equation above (ρx) is the beam ion range (mg/cm^2) in the target, N is # of counts per channel, (E/ch)$_\gamma$ is γ-ray energy in MeV per channel, (E_i/E_γ) the energy of the emitted light particle relative to γ-ray energy as given in Table III.6, (d.t.c.) stands for the deadtime correction of the detector, $d\Omega$ is the detector solid angle, A_t is the target mass number, ϕ_t is the target angle relative to the beam axis, G is a lab to c.m. conversion factor (which is close to unity), Q is the collected charge in μC, and q is the beam charge state.

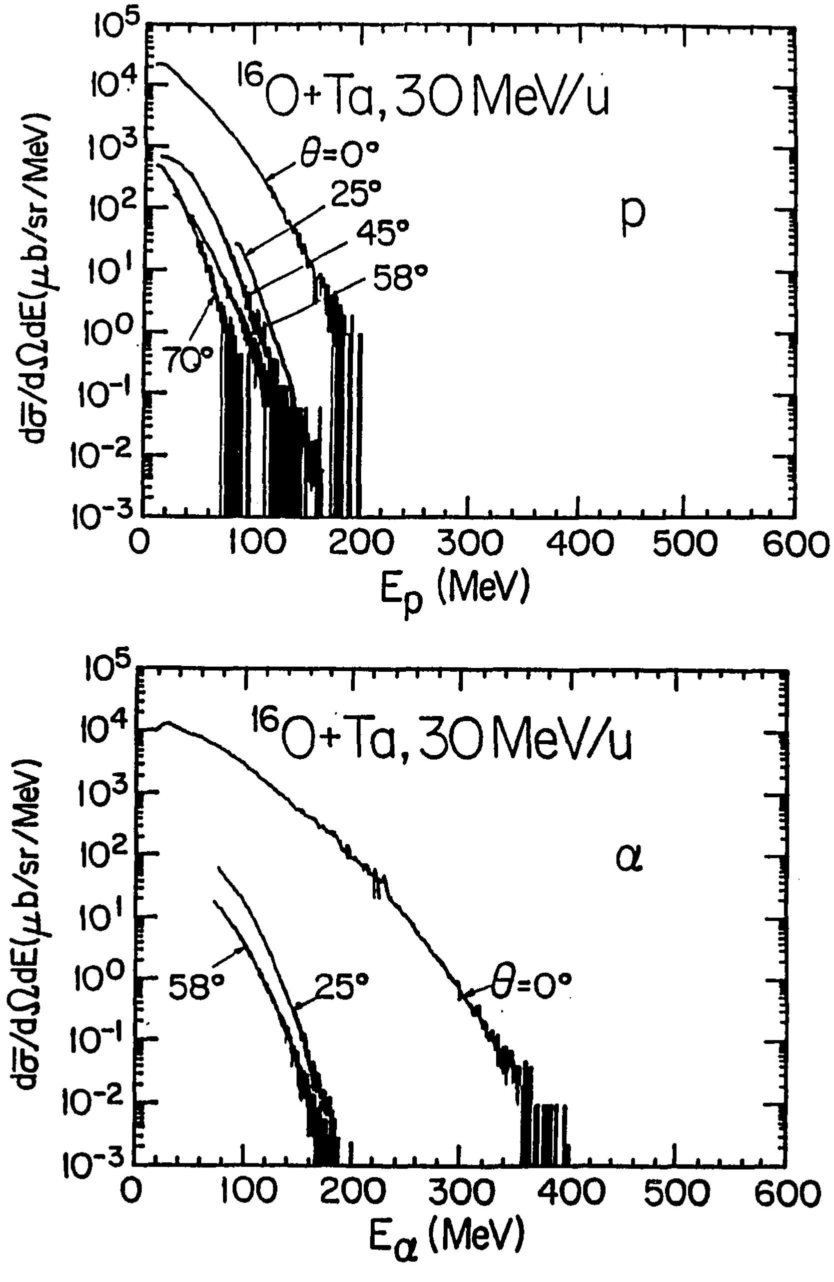

Fig. IV.1 (top) and IV.2 (bottom): The p and α energy spectra for 30 MeV/u ^{16}O on Ta.

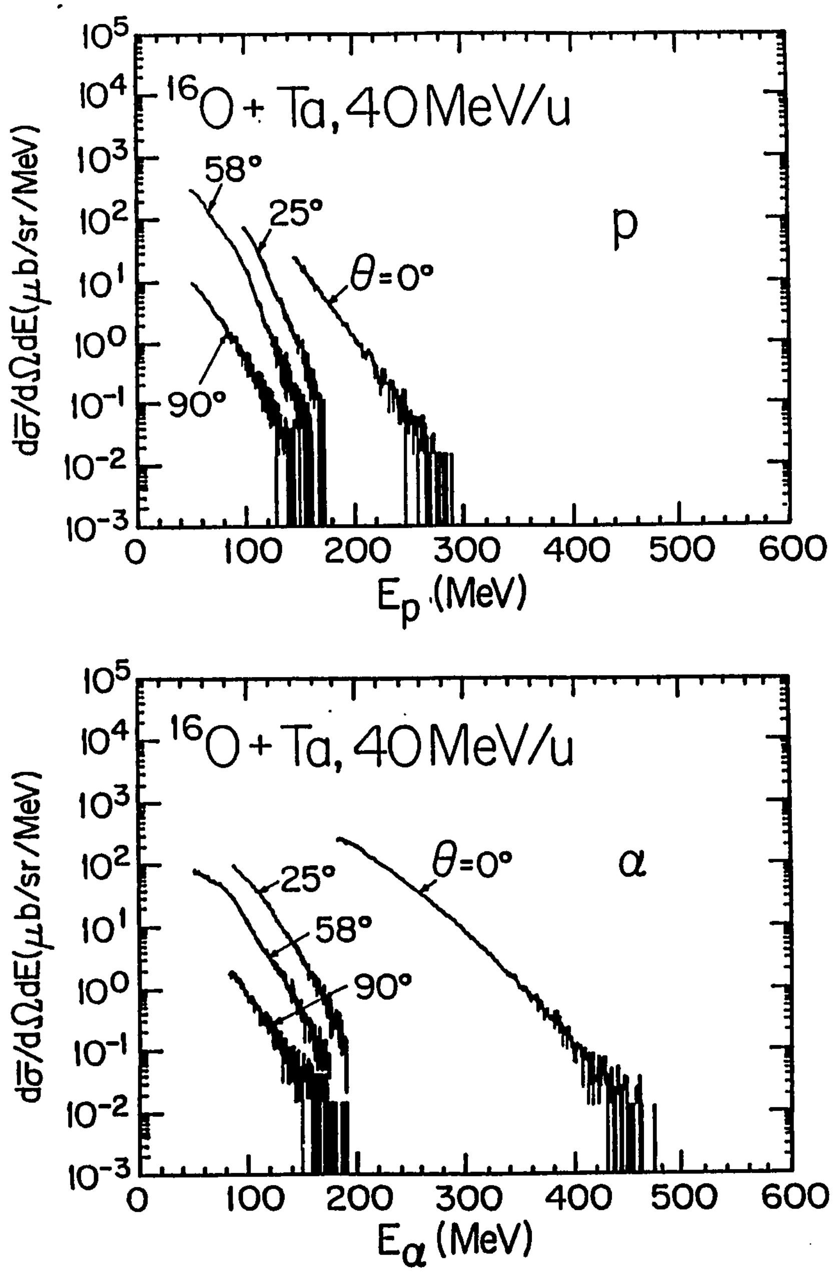

Fig. IV.3 (top) and IV.4 (bottom): The p and α energy spectra for 40 MeV/u ^{16}O on Ta.

Theoretical calculations will include the fits to zero degree data using the moving source model. Based on the parameters of these fits, moving source calculations were done for other angles and compared with the data. This will be used to deduce the source velocity (v_s) and determine the apparent source "temperature" (T_S). The latter can then be compared to values expected from the Fermi gas model (Appendix A) assuming thermal equilibrium.

IV.1. The Experimental Data:

a) These data consist of five groups. The first group is shown in Figs. IV.1 - IV.8 and presents p and α energy spectra at different angles for ^{16}O at 30 and 40 MeV/u and ^{40}Ar at 20 and 30 MeV/u on a thick Ta target/beamstop. The second group, Figs. IV.9 - IV.12, shows the energy spectra of p, d and α for the above mentioned systems. The third group consists of figures IV.13 and IV.14 and shows the 0° energy spectra for p, d and α for ^{16}O on Cu at 40 MeV/u, ^{40}Ar on Cu at 30 MeV/u. The last group, Fig. IV.15, shows the α energy spectra at 0° from 30 MeV/u ^{40}Ar on two Ta targets separated by 0.5 m. A thin target was in the front box and a thick target was in the scattering chamber, as seen in Fig. III.6. Both the BGO and the large 10 × 10 × 40cm NaI detectors show almost the same spectra for the thin target despite having rather different calibrations, etc.

b. Angular distributions

These spectra consist of two groups. The first group shows p (Fig. IV.16) and α (Fig. IV.17) angular distributions for 40 MeV/u ^{16}O on Ta and a combined spectra for p and α (Fig. IV.18) for the same system. The second

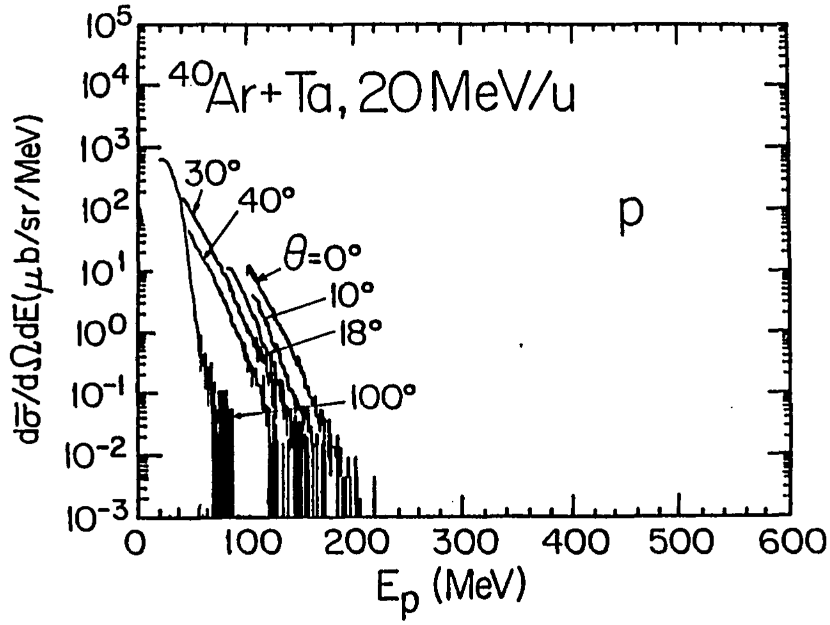

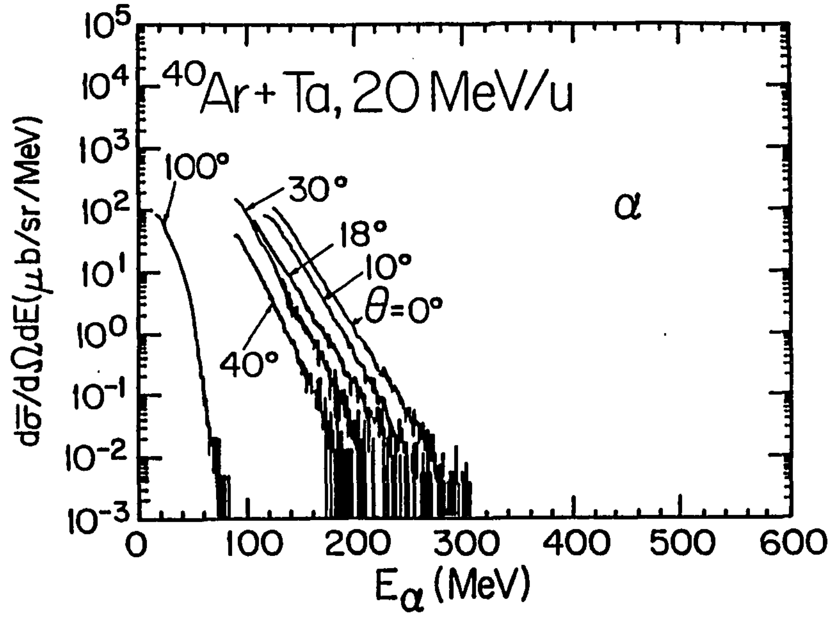

Fig. IV.5 (top) and IV.6 (bottom): The p and α energy spectra for 20 MeV/u ^{40}Ar on Ta.

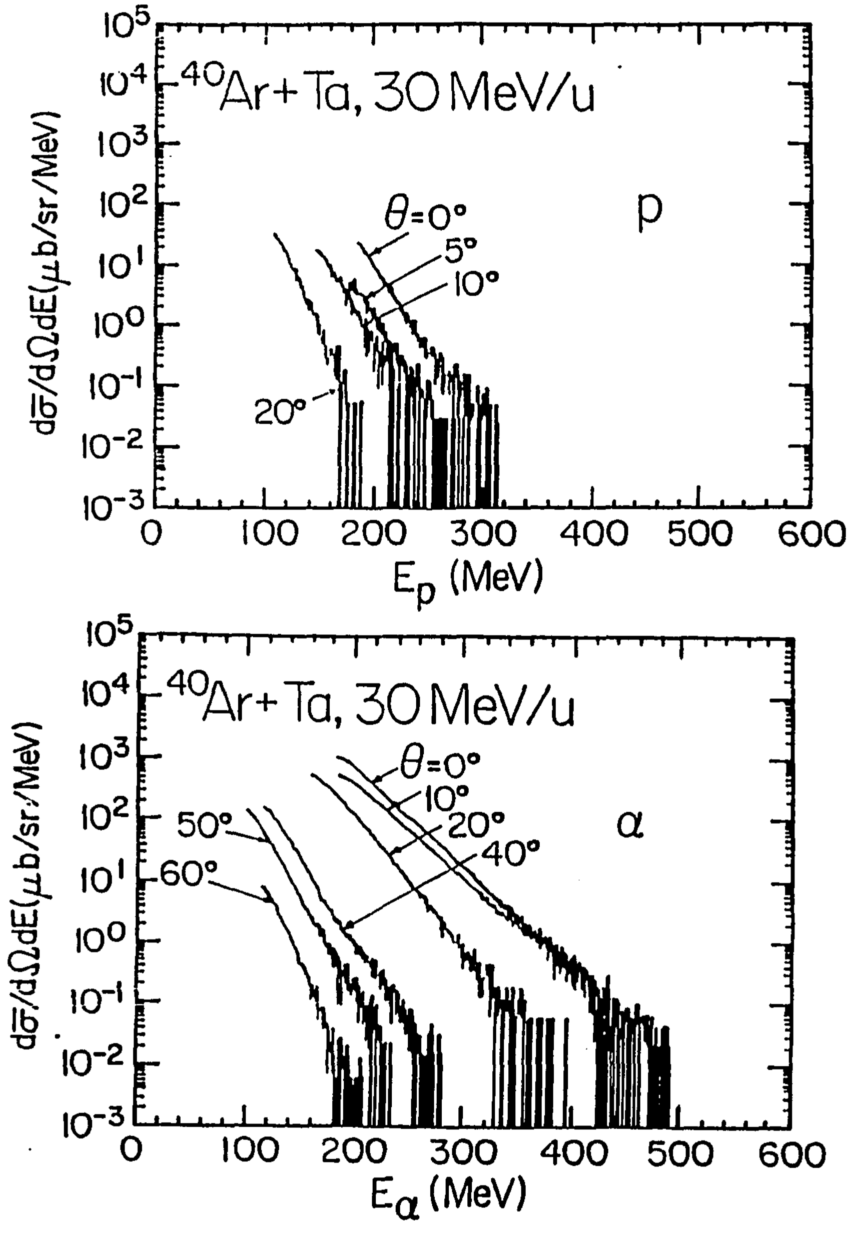

Fig. IV.7 (top) and IV.8 (bottom): The p and α energy spectra for 30 MeV/u ^{40}Ar on Ta.

group shows p and α angular distributions for 20 and 30 MeV/u ^{40}Ar on Ta. Spectra of both p and α are shown (Figs. IV.19, IV.22 and IV.23) for these reactions.

c. The yields relative to α particles

Bar-graph representations for the yields, at 0°, of p, d, t relative to α particles are given in Figs. IV.24 - IV.27. Figs. IV.24 and IV.25 show the yields for ^{16}O on Ta and ^{16}O on Cu. Figs. IV.26 and IV.27 show the same spectra for ^{40}Ar beam on Ta and Cu respectively. These ratios were calculated for different beam energies (indicated on the figures) from the yield integrated over the energy range from a certain minimum energy, E_i and are tabulated in Table IV.1.

d. Multiplicity

The multiplicity represents the frequency of coincident events and therefore, single multiplicity (M=1) means one detector has an event. Double multiplicity means two detectors have events simultaneously and so on. Figs. IV.28 to IV.31 show bar-graph representations for the multiplicity for ^{16}O and ^{40}Ar beams on Ta and Cu at different beam energies, as indicated on the figures.

Although TOF and PSD methods were set up, TOF was primarily used to gate the events and produce energy spectra. It was easy to identify p, d and α, at least in BGO, and p and α in NaI. Occasionally TOF *vs.* $\mathcal{L}$ results were checked with TOF *vs.* PSD plots for NaI data only. Gating from BGO TOF was better defined and more reliable than NaI TOF. [Energy spectra gated from BGO TOF also had minimal pulse pile up.] Therefore, masses in BGO are easier to identify and gate. This can be attributed to the faster

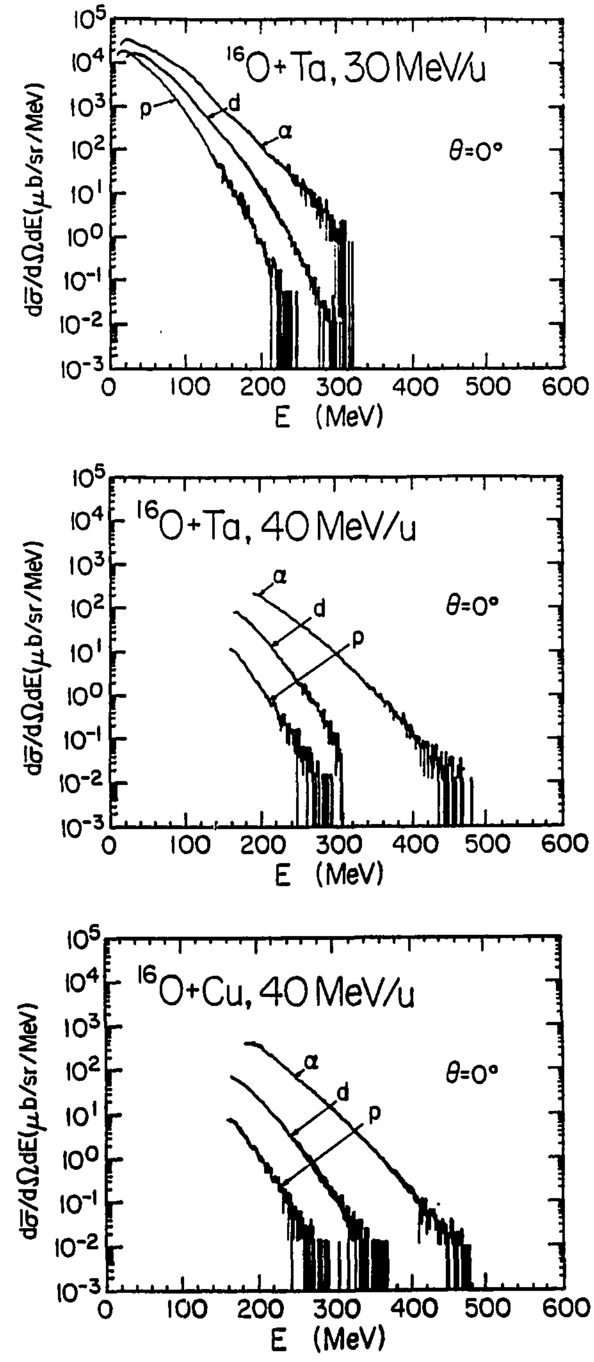

Fig. IV.9 (top), IV.10 (middle) and IV.11 (bottom): The *p*, *d* and *α* energy spectra at 0° for 30 MeV/u ^{16}O on Ta and 40 MeV/u ^{16}O on Ta and Cu.

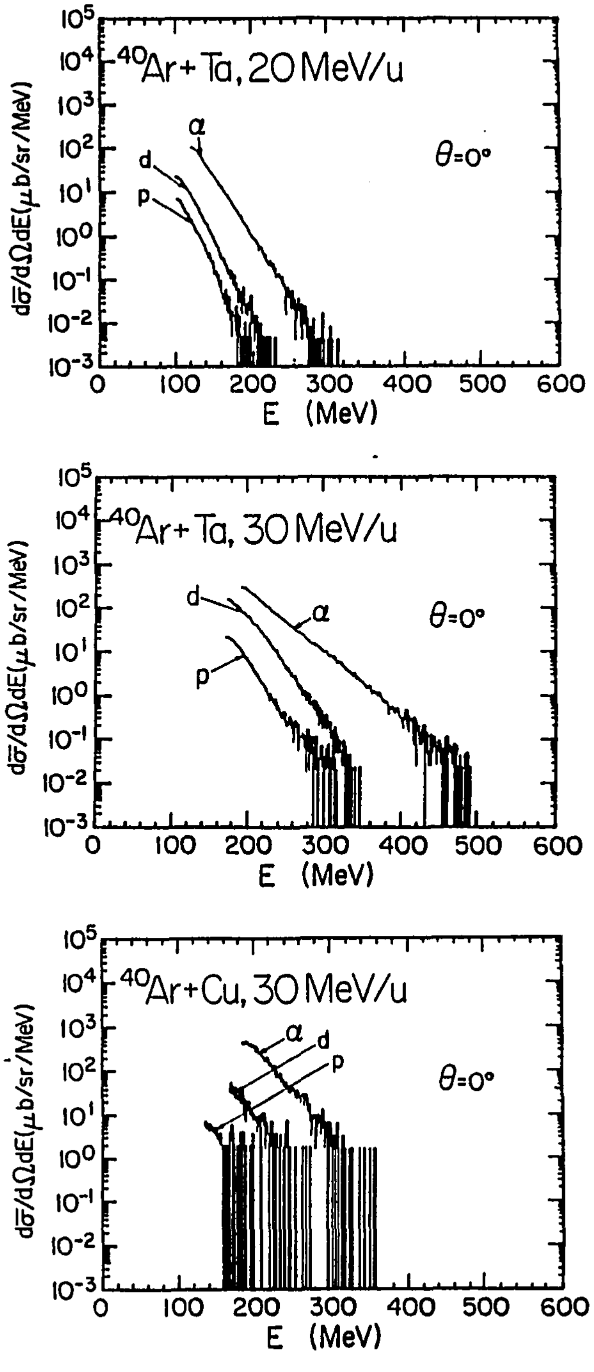

Fig. IV.12 (top), IV.13 (middle) and IV.14 (bottom): The *p*, *d* and *α* particle energy spectra at 0° for 20 MeV/u ^{40}Ar on Ta and 30 MeV/u ^{40}Ar on Ta and Cu.

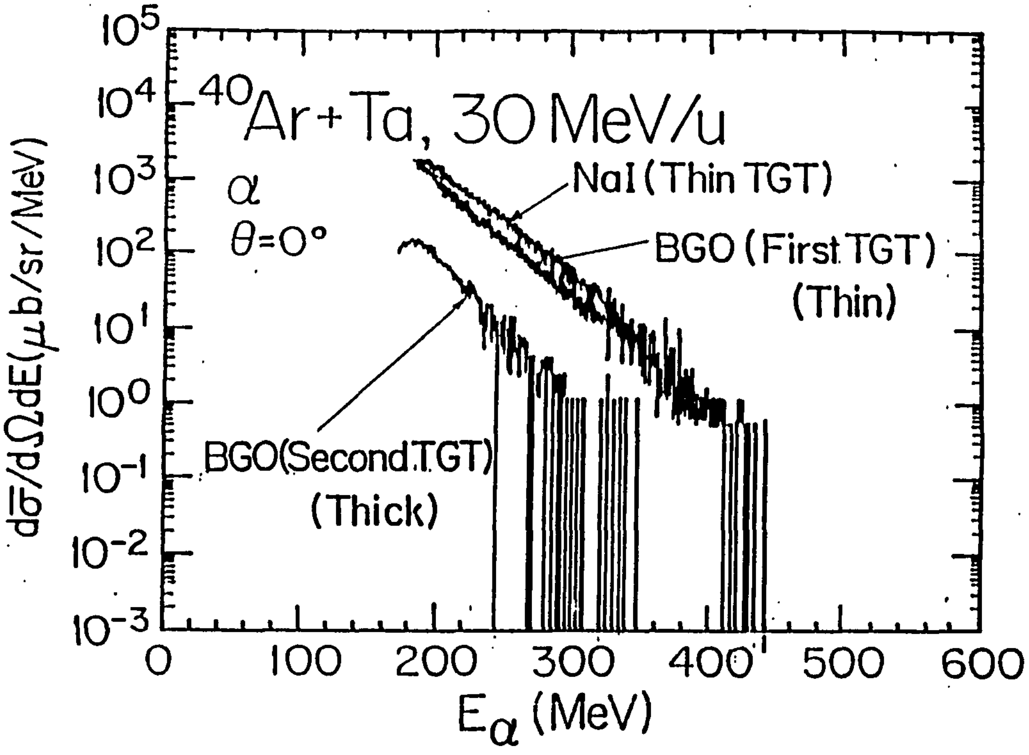

Fig. IV.15. The α-particle energy spectra for 30 MeV/u ^{40}Ar on (thin and thick) Ta at 0° in NaI (10 × 10 × 40 cm) and BGO scintillators.

response and minimal after-pulsing of BGO relative to NaI (Table III.1). Hence BGO is better suited at high count rates such as those encountered in HI experiments. However, its speed also results in poor PSD for mass identification.

Most of my data were taken with thick targets (beam stop). Conceptually, this was expected to produce very-energetic light particles, assuming the beam particles and heavy fragments will stop in the target. Light particles will come out of the target individually, or as part of a light-mass moving source. To get spectra with a well defined beam energy, a thin and thick target scheme can be used as explained in Chapter 3. The α-particle energy spectra produced by this scheme are shown in Fig. IV.15. The BGO and NaI thin target spectra are almost identical. The difference between α-particle energies between thin and thick target spectra is greater than the α-particle energy loss in the thick target. Since the cross-section is a physical quantity, it should be independent of the target thickness i.e. both thin and thick target spectra should yield approximately the same cross section for the same beam energy. The invariance of cross sections can be seen by comparing the α-particle energy spectra (Figs. IV.13 & IV. 15).

Energy spectra and angular distributions show that the cross-sections, as expected, increase with higher beam energy and smaller detection angles, but decrease rapidly with emitted particle energies. The latter,also as expected, follows the exponential form: $dN/dE = N_o exp(-E_L/T_L)$ where T_L is the slope parameter in the lab.

Figs. IV.16 - IV.18 show that the cross-sections increase rapidly towards the beam direction and then decrease more slowly with larger scattering angles.

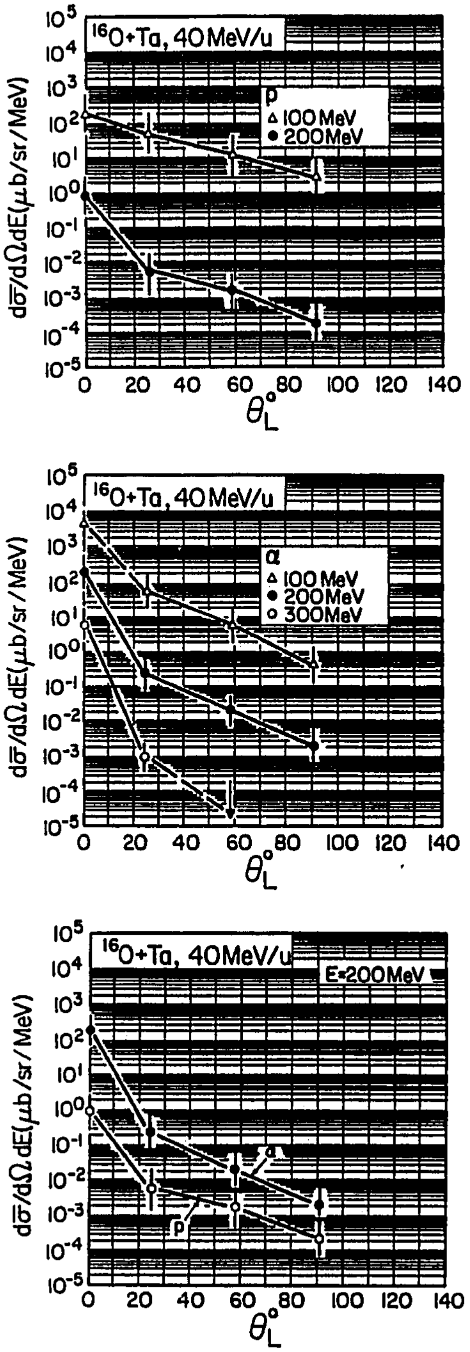

Figs. IV.16 (top), IV.17 (middle) and IV.18 (bottom): The angular distributions (in the laboratory) for 40 MeV/u ^{16}O on Ta at different beam and emitted particle energies. Dashed lines indicate an extrapolation to other angles.

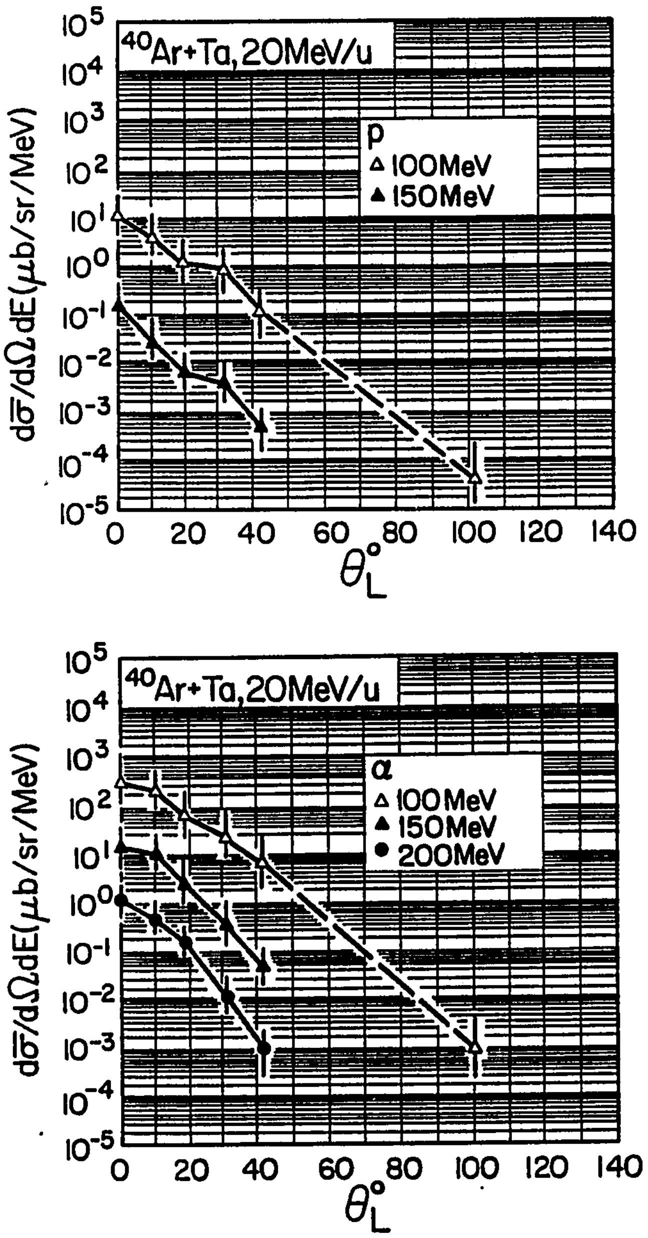

Fig. IV.19 (top) and IV.20 (bottom): The angular distributions of p and α particles (in the laboratory) for 20 MeV/u ^{40}Ar on Ta at different energies. Dashed lines indicate an extrapolation to the experimental points.

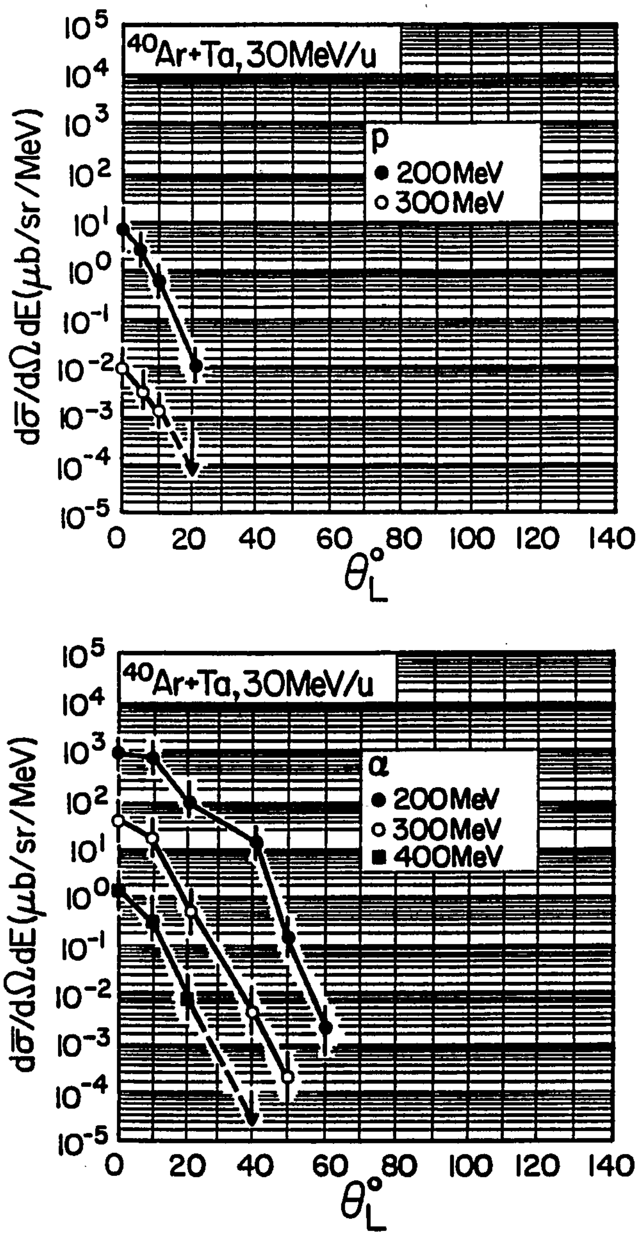

Fig. IV.21 (top) and IV.22 (bottom): The angular distributions of p and α particles (in the laboratory) for 30 MeV/u ^{40}Ar on Ta at different energies. Dashed lines indicate an extrapolation to other angles.

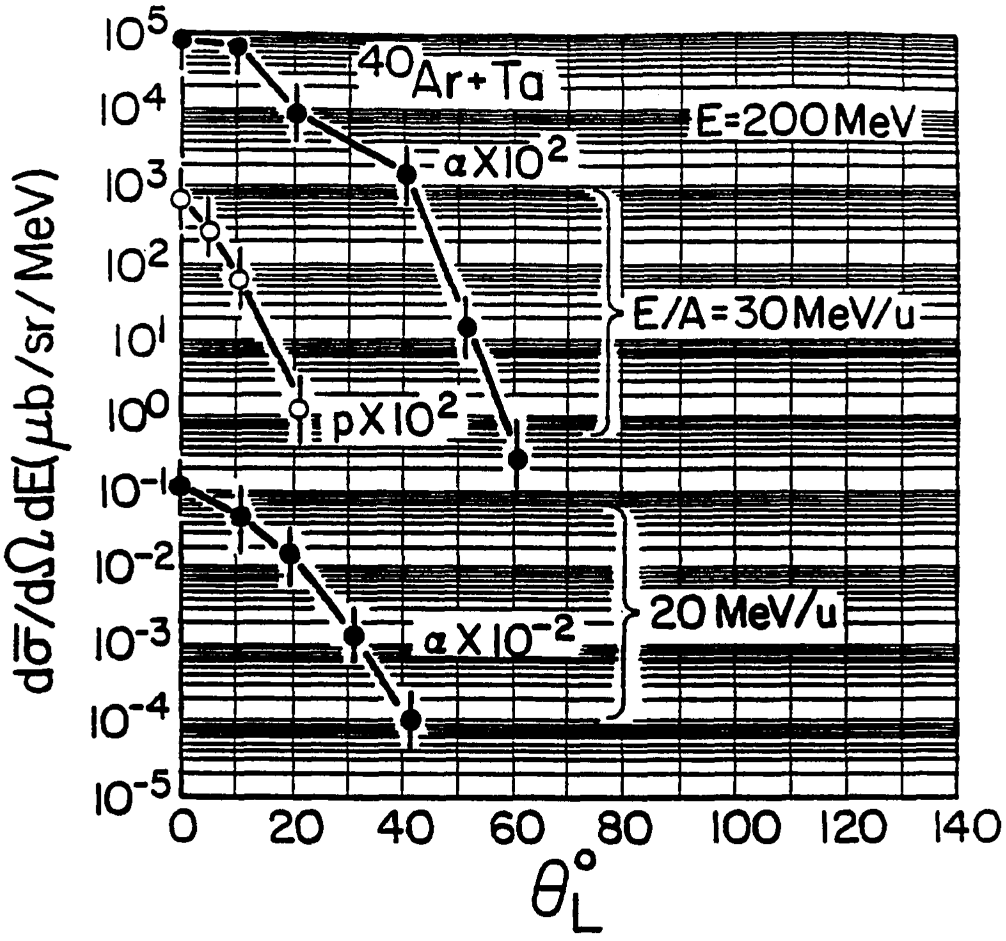

Fig. IV.23. The angular distributions of α particles in the laboratory for 20 and 30 MeV/u ^{40}Ar on Ta and 30 MeV/u ^{40}Ar on Ta for p.

It is noticed that cross-sections from Ta and Cu targets for ^{16}O and ^{40}Ar beams are similar. This leads to the conclusion that projectile breakup (by some mechanism) may be the main source for these particles. The multiplicity (Fig. IV.28 - IV.31) seems to increase with larger projectile masses regardless of the targets. This again means that the fragmentation is closely related to the projectile and the targets are primarily spectators.

The relative yield depends on the ejected masses and target nucleus, as seen from Table IV.1 and the bar graphs (Figs. IV.24 - IV.27). Table IV.1 doesn't give a clear and systematic dependence of particle yields on the beam energy. However, it is noticed that the source more easily ejects α-particles than protons. Since an α particle has high internal binding energy (BE^{α} = 28.3 MeV) only ca. 20 MeV is typically needed to remove an α from a projectile nucleus.[4]

Alpha particle zero degree spectra from ^{16}O on both Ta and Cu extend to near the beam energy, while p spectra extend to about half the beam energy. It was expected that this observation would continue with higher beam energy. The ^{40}Ar data doesn't support this despite the fact that light particles are still emitted with high energies. The cross-section is not large for proton emission compared to α-emission, particularly for α-cluster projectiles such as ^{16}O.

System	Energy (MeV/u)	N_α/N_p	N_α/N_d	N_α/N_t
^{16}O + Ta	30	296	18	5.6
	40	165	11.	35
^{16}O + Cu	40	736	24	-
^{40}Ar + Ta	20	54	11	22
	30	78	4	-
^{40}Ar + Cu	30	560	32	-

Table IV.1. Energy integrated $\theta = 0°$ yields of p, d and t relative to α particles for different targets and beam energies.

System: 30 MeV/u ^{16}O + Ta, θ=0°

v_s/v_b	T_L^p	T_S^p	T_L^d	T_S^d	T_L^α	T_S^α
1	16	6.2	17.3	4.9	26.7	4.5
0.75	"	8.6	"	8.7	"	5.9
0.5	"	10.8	"	12	"	13.3

System: 40 MeV/u ^{16}O + Ta, θ=0°

v_s/v_b	T_L^p	T_S^p	T_L^d	T_S^d	T_L^α	T_S^α
1	17.2	7.9	18.4	6.8	25.2	6
0.75	"	9.8	"	10.1	"	10.8
0.5	"	11.8	"	13.6	"	16.7

System: 40 MeV/u ^{16}O + Cu, θ=0°

v_s/v_b	T_L^p	T_S^p	T_L^d	T_S^d	T_L^α	T_S^α
1	17	8	19.2	7.4	24	5.4
0.75	"	9.9	"	10.9	"	10.1
0.5	"	11.9	"	14.5	"	15.9

Table IV.2. Experimental slope parameters T_L and deduced (moving-source model) source temperatures of p, d and α-particles for the above systems. Fits were made for $\theta^\circ = 0^\circ$ spectra assuming three different source velocity (v_s) to beam velocity (v_b) ratios.

System: 20 MeV/u ^{40}Ar + Ta, 0°

v_s/v_b	T_L^p	T_S^p	T_L^d	T_S^d	T_L^α	T_S^α
1	12.1	6.7	13.1	9.2	16	4.5
0.75	"	8	"	11.7	"	7.1
0.5	"	9.2	"	13.6	"	9.9

System: 30 MeV/u ^{40}Ar + Ta, 0°

v_s/v_b	T_L^p	T_S^p	T_L^d	T_S^d	T_L^α	T_S^α
1	15	8.8	19.3	8.4	28.5	11.4
0.75	"	10.4	"	10.8	"	15.8
0.5	"	11.9	"	14.2	"	20.1

System: 30 MeV/u ^{40}Ar + Cu, 0°

v_s/v_b	T_L^p	T_S^p	T_L^d	T_S^d	T_L^α	T_S^α
1	-	-	19	7.2	21	4.9
0.75	-	-	"	9.6	"	8.6
0.5	-	-	"	12.5	"	11.5

System: 30 MeV/u ^{40}Ar + thin Ta, 0°

v_s/v_b	T_L^p	T_S^p	T_L^d	T_S^d	T_L^α	T_S^α
1	-	-	-	-	22.8	4.5
0.75	-	-	-	-	"	8.8
0.5	-	-	-	-	"	12.7

System: 30 MeV/u ^{40}Ar + thick Ta, 0°

v_s/v_b	T_L^p	T_S^p	T_L^d	T_S^d	T_L^α	T_S^α
1	-	-	-	-	21.7	8
0.75	-	-	-	-	"	11.3
0.5	-	-	-	-	"	-

Table IV.3. As per Table IV.2.

System: 9.5 MeV/u ^{32}S + Ta, 0°

v_s/v_b	T_L^p	T_S^p	T_L^d	T_S^d	T_L^α	T_S^α
1	6.4	4.4	-	-	12	7

System: 14 MeV/u ^{32}S + Ta, 0°

v_s/v_b	T_L^p	T_S^p	T_L^d	T_S^d	T_L^α	T_S^α
1	11	7.3	-	-	19	10

System: 10.3 MeV/u ^{58}Ni + Ta, 0°

v_s/v_b	T_L^p	T_S^p	T_L^d	T_S^d	T_L^α	T_S^α
1	4.6	3.7	-	-	7.5	4.1

Table IV.4. As per Table IV.2(Ref.43).

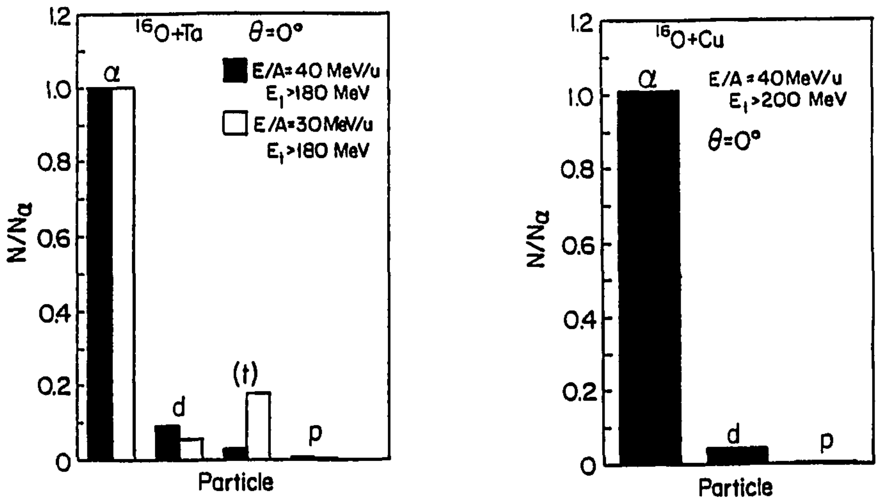

Fig. IV.24 (left) and IV.25 (right): The yields relative to α particles for ^{16}O on Ta and Cu at different beam energies. Parenthesis indicate that particle identification is uncertain.

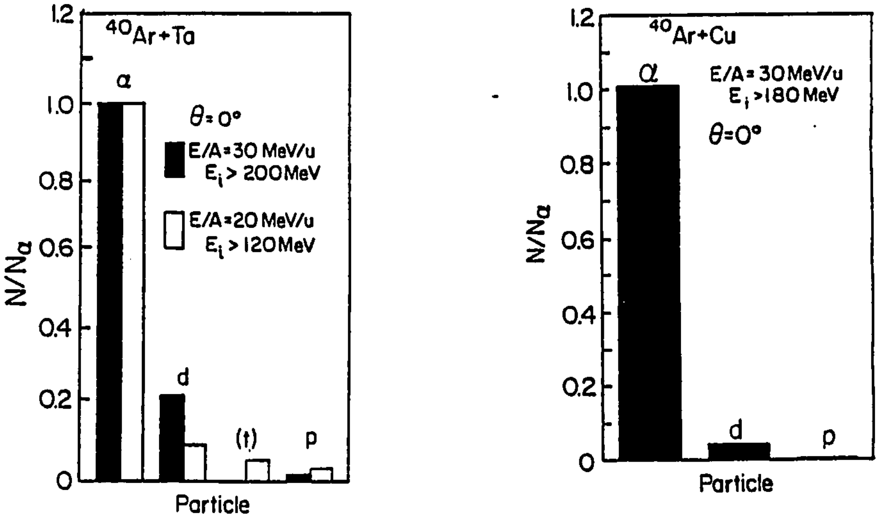

Fig. IV.26 (left) and IV.27 (right): The yields relative to α particles for ^{40}Ar on Ta and Cu at different beam energies. Parenthesis indicate that particle identification is uncertain.

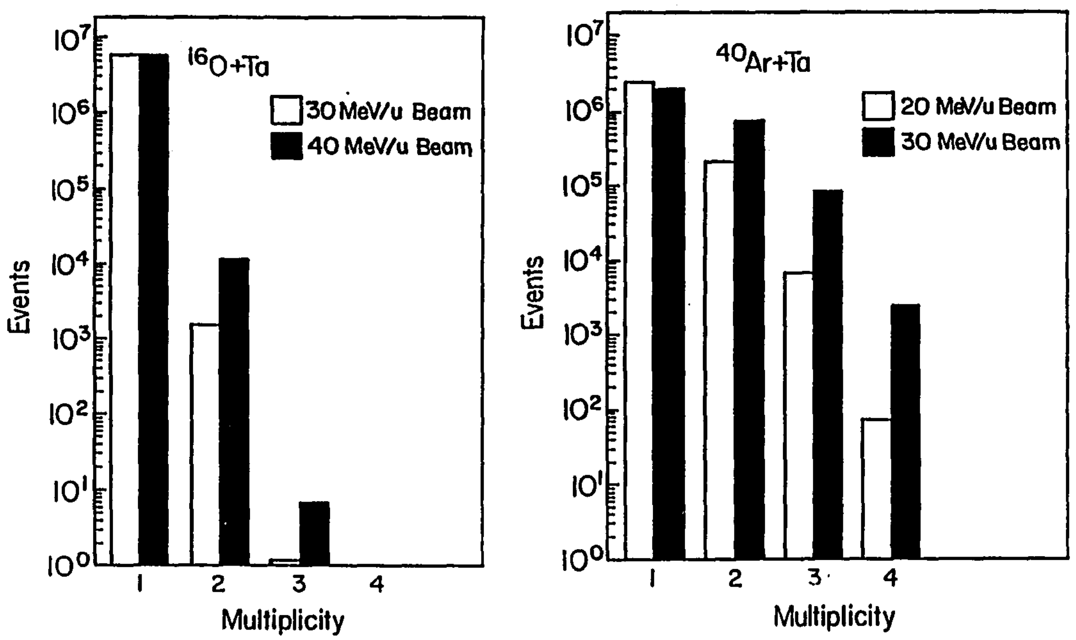

Fig. IV. 28 (left) and IV.29 (right): Event multiplicity in detectors for both ^{16}O and ^{40}Ar on Ta at different beam energies.

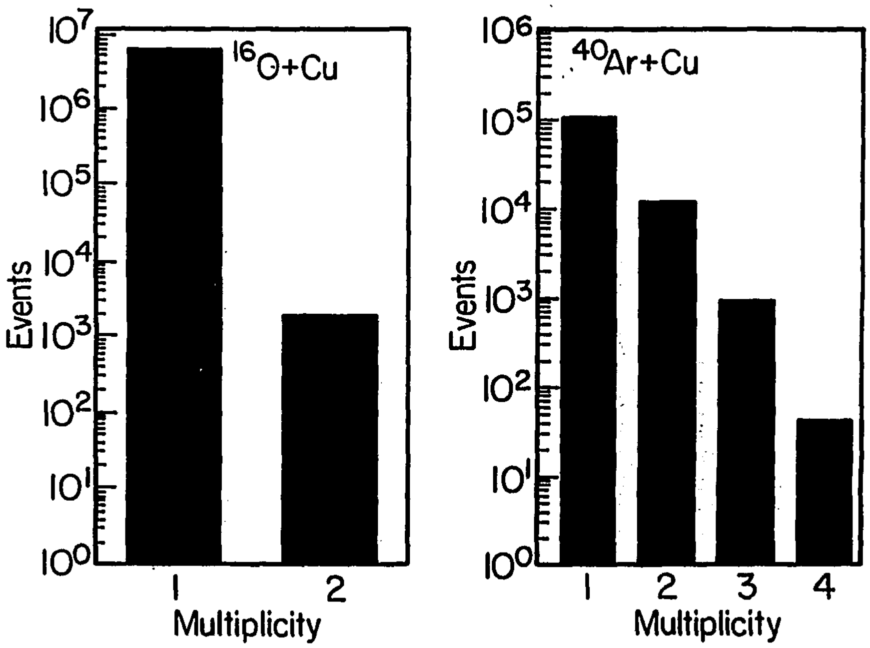

Fig. IV.30 (left) and IV.31 (right): Event multiplicity in detectors for ^{16}O and ^{40}Ar on Cu, 40 MeV/u and 30 MeV/u respectively.

IV.2. Moving-Source Model Fits to Data

The moving source model (Eq. II.5) has been used to fit the energy spectra and angular distributions of emitted light ions (Figs. IV.32 to IV.43). Calculations were done assuming moving source velocities of $v_s = 0.5\ v_b$, $0.75\ v_b$ and $1.0\ v_b$. This covers the range of v_s expected in the limit of nucleon-nucleon collisions ($v_s = 0.5\ v_b$; Fig. II.1 with $v_b = v_p$) through projectile break-up ($v_s = v_b$; Fig. II.1). The source temperature, T_S, and cross section normalization were then adjusted to fit the magnitude and shape (e.g. T_L) of the LI energy spectra at $\theta = 0°$ (Figs. IV.41 and IV.42). Since the data at $\theta = 0°$ are not sufficient to independently determine v_s *and* T_S it is then necessary to also compare with data for $\theta > 0°$. Along with the data for ^{16}O and ^{40}Ar projectiles, data obtained previously at ANL-ATLAS for ^{32}S and ^{60}Ni beams were also fit. Some typical calculations are shown in Figs. IV.37 to IV.40 (for clarity not all calculations are shown).

One observes that the data for the most foreward-angle, highest-energy α particles are best fit using $v_s \rightarrow v_b$, corresponding to $T_S \leq T_L/1.5$ (Table IV.2 to IV.4). This also applies to the deuteron and proton spectra, but to a lesser extent, (Figs. IV.32 to IV.36), particularly for angles, $\theta > 20°$. At large angles *viz.* $40° < \theta < 100°$, particularly for protons and deuterons, $v_s \rightarrow 0.5\ v_b$ is indicated. This is consistent with published analyses of similar data, $\theta > 20°$ which typically require $0.4 < v_s/v_b < 0.7$. The most extensive data available ($\theta \rightarrow 180°$) are best fit with a multi-component source,[1,14,24] each having a separate velocity and temperature, the latter generally in the range $T_S = 3$ to 10 MeV ($v_s \doteq 0.5 v_b$). While our data $\theta \geq 40°$ do not necessarily require $v_s > 0.5$, the data as $\theta \rightarrow 0°$, particularly for the α-particles, requires $v_s \rightarrow v_b$, consistent with projectile-like fragmentation. Also, the apparent source temperatures, T_S, needed to fit the energy spectra, α-particles in particular, are higher than needed to fit the data

$\theta \geq 40°$, or those reported by other groups fitting data $\theta > 40°$.

The required T_S values for α particles are in the range 6 MeV to 20 MeV and are greatest for the α-cluster projectiles ^{16}O and ^{32}S (see Tables). [The values of T_S are even higher if one uses $v_s = 0.5v_b$, the value normally used to describe fragmentation data, $\theta \geq 40°$.] If the source (projectile or target) had achieved thermal equilibrium in the reaction, one would expect the Fermi gas model to apply (Appendix A) and one can then deduce a source temperature by assuming total conversion of the incident beam energy, E_{beam}, into source excitation, E_x, and then using Eq. A.13. This yields $T_S \doteq 14$ to 20 MeV for a source mass equal to the projectile mass (16 or 40 u) and $T_S \doteq 5$ MeV for $A_S = A_{CN}$. Also, above T_S = 8 MeV, the mean nucleon binding energy (Appendix A), the source will become totally unbound, hence, in thermal equilibrium, a *limiting* source temperature of ca. 8 MeV can be expected, *independent* of the beam energy i.e. E_x. This has been reported in other experiments.[1]

It is therefore instructive to display the apparent source temperatures vs. $(E/A)_{beam}$. These are shown in Fig. IV.44 and compared with general systematics reported for LI emission, $\theta \geq 10°$, in HI collisions.[1] Obviously our data indicate that for α-particle emission the source is often not at thermal equilibrium (i.e. $T_S > 8$ MeV) nor are there indications of reaching a limiting temperature, $T_S \doteq 8$ MeV as indicated by some other experiments, $10 < E/A_{beam} < 100$ MeV/u. This has also been observed to be the case for $E/A \geq 200$ MeV/u and is attributed[1] to a local heating ("hot spot") of the projectile (or a small piece of the latter). In any case it appears that a *significant* fraction of the beam energy can be transferred, via local heating or other mechanisms, to α-particles, and to some extent other LIs, particularly for lighter, α-cluster projectiles such as ^{16}O and ^{32}S.

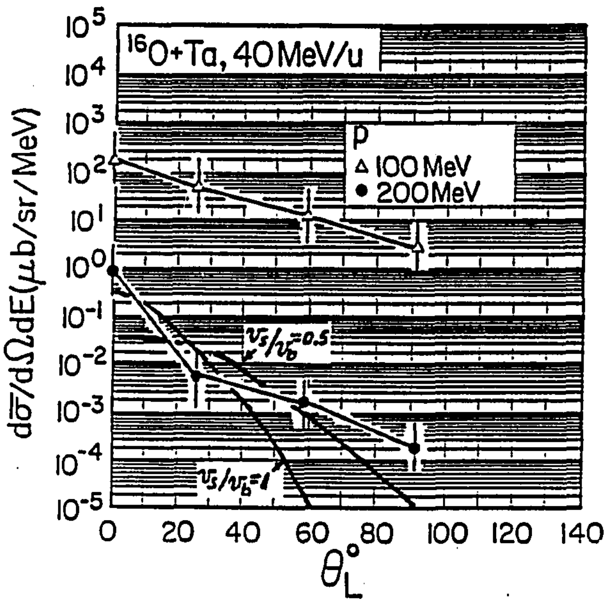

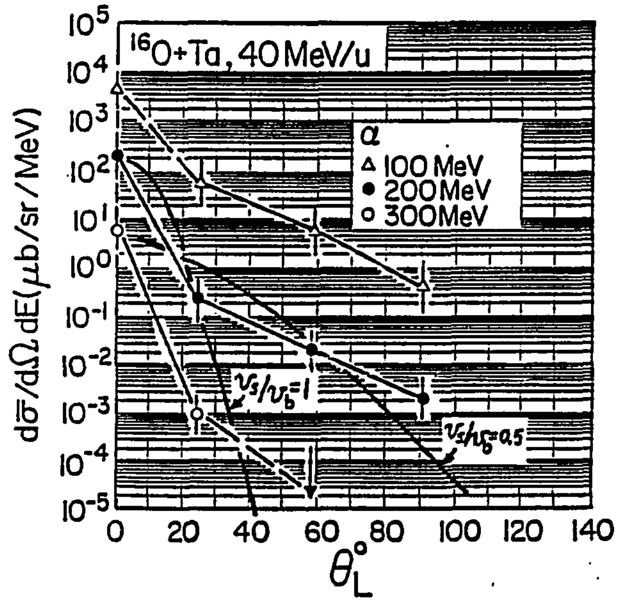

Fig. IV.32. The angular distributions of p and α-particles for 40 MeV/u ^{16}O on Ta at different emitted particles energies. The curves shown are moving-source model fits.

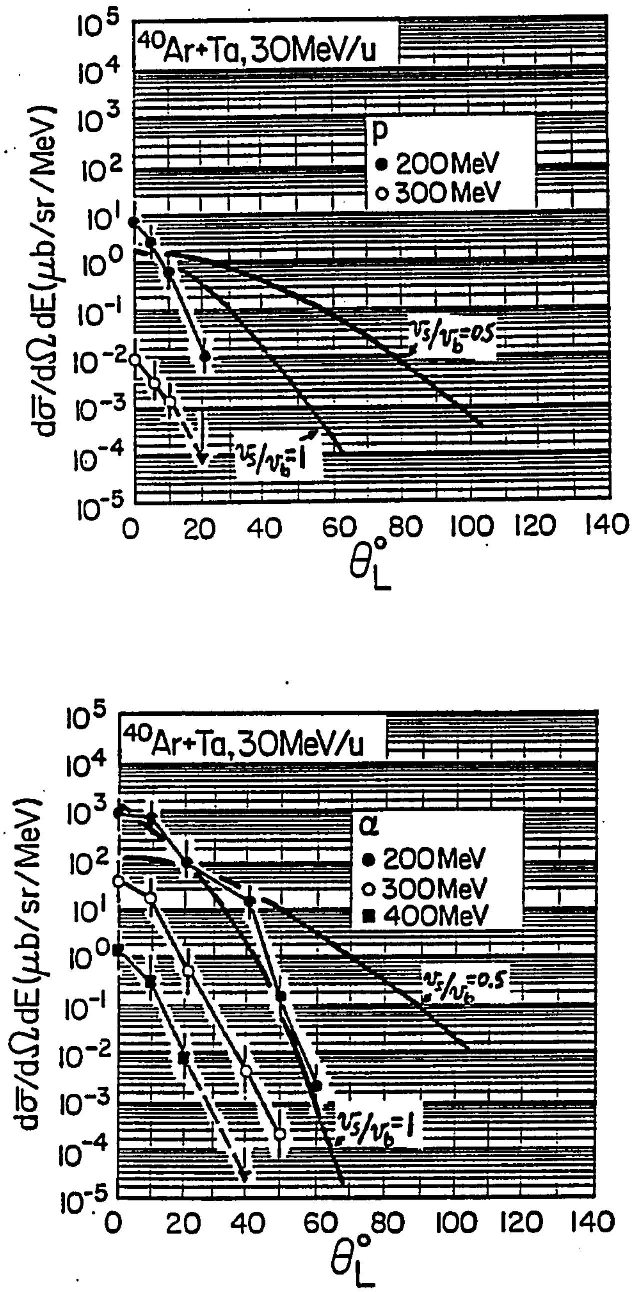

Fig. IV.33. The angular distributions of p and α-particles for 30 MeV/u ^{40}Ar on Ta. The curves shown are moving source model fits.

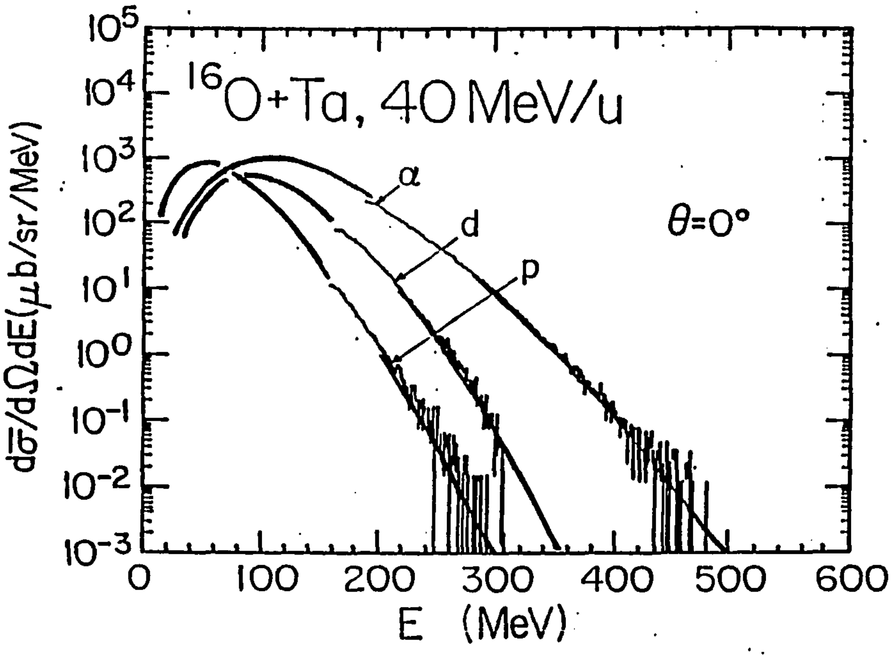

Fig. IV.34. The p, d and α energy spectra for 40 MeV/u ^{16}O on Ta and moving-source model fits, $v_s/v_b = 1.0$, 1.0 and 0.75 respectively.

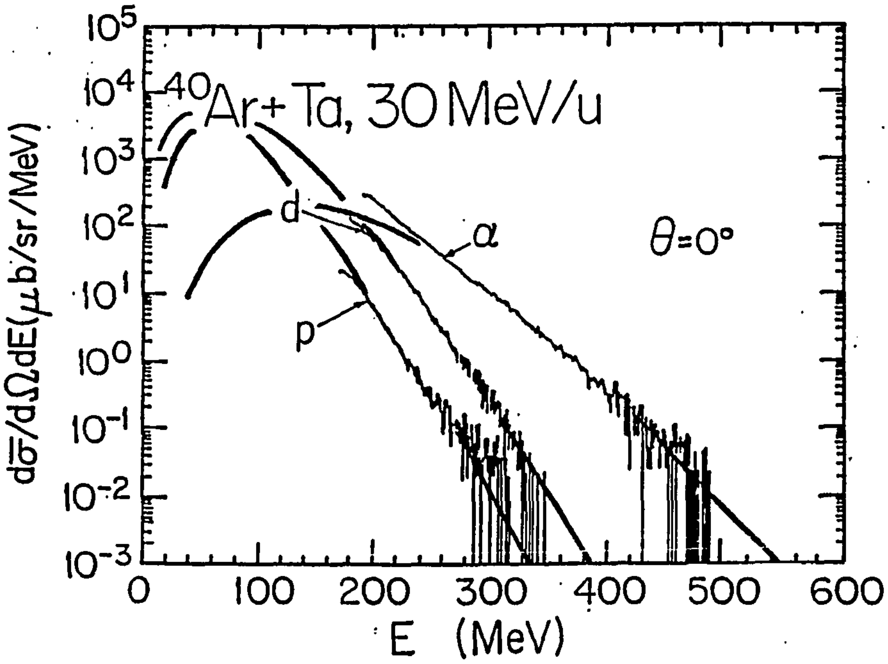

Fig. IV.35. The p, d and α energy spectra for 30 MeV/u ^{40}Ar on Ta and moving-source model fits, $v_s/v_b = 1.0$.

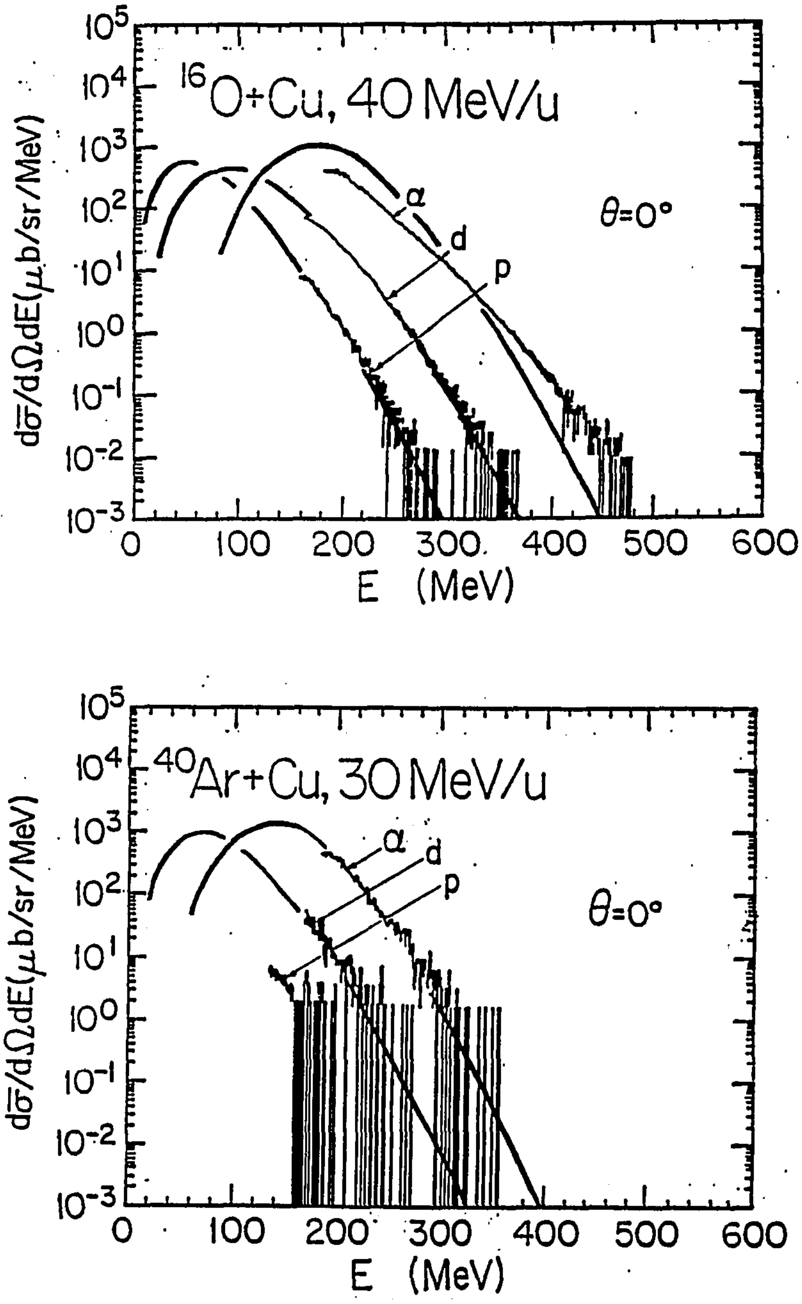

Fig. IV.36. The p, d and α energy spectra at 0° for a Cu target and moving-source model fits, $v_s/v_b = 1.0$.

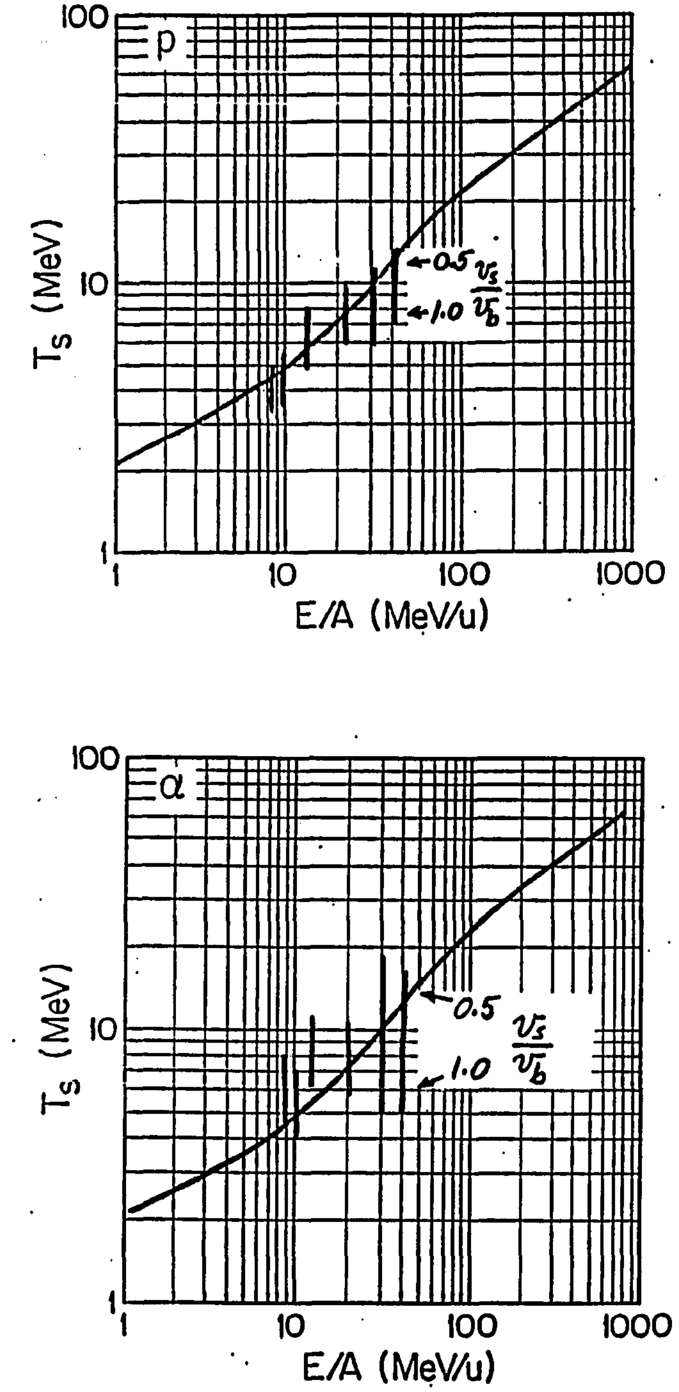

Fig. IV.37. Apparent source temperatures as a function of beam energy. The curve represents systematics reported in Ref. 1 for various LI emission.

CHAPTER V

CONCLUSIONS

We have shown that a large BGO scintillator detector is well suited for detection of very-high-energy light ions in heavy ion reactions. TOF alone can give adequate particle identification for energies up to about 1.3 GeV. Large arrays of BGO detectors appear to be desirable for future measurements. Since BGO is a fast scintillator, the high count rates encountered in high-energy heavy-ion reactions can be tolerated. This is not often the case for conventional high density particle detector scintillators such as NaI and CsI. Also, the high stopping power of BGO permits detection and use of cosmic ray muons for calibration purposes even in small detectors.

Fitting the data with the moving source model, including Coulomb correction of the particles' velocities due to the projectile, requires a source velocity (v_s) relative to the beam velocity (v_b) in the range

$$0.5 \leq v_s/v_b \leq 1$$

This gives the following ranges for source temperatures (T_s) of p, d and α particles respectively.

$$4\ MeV \leq T_s^p \leq 12\ MeV$$

$$5\ MeV \leq T_s^d \leq 15\ MeV$$

and

$$4\ MeV \leq T_s^\alpha \leq 20\ MeV.$$

These values are generally higher than CN or Fermi gas-model temperatures assuming thermal equilibrium (*viz* $T_{CN} \sim$ 5-6 MeV). Therefore, it can be concluded that the process is often a non-equilibrium emission from a rapidly moving hot source with velocities $v_s \doteq v_b$. Preferred fragmentation is into α-particles, particularly for α cluster like projectile such as ^{16}O and ^{32}S. At zero degrees the α-particle energies can reach values close to the total beam energy. Measurements using thin and thick targets at $\theta = 0°$, using TOF for particle identification confirm, as expected, that the sources of the highest energy particles are due to the highest energy component of the beam.

Comparison of multiplicities using ^{16}O and ^{40}Ar beams showed a marked increase in multiple-particle emission for the ^{40}Ar beam. This supports the conclusion that the source of very-energetic light particles is associated primarily with the projectile. The spectra and multiplicities observed for a Cu target are similiar to those observed for a Ta target and again support the latter hypothesis. Calculations showed that the effect of Coulomb force on the reaction cross-sections is very small if not negligible.

Future experiments at NSCL ($E = 800q^2/A$ MeV) cyclotron are planned in the future, with heavy ion beams $E/A \geq 80$ MeV/u. An array of four BGO detectors, based on the detectors and techniques used in this work, is being built and will be used in future measurements. These experiments should help provide more clarification on the production mechanism of very-high-energy light particles in heavy ion collisions. In particular, this will further examine the apparent source temperatures of the emitted particles at 0° as a function of increased beam energy and the fraction of the beam energy which can be transferred to the emitted light particles.

APPENDIX A

THE NUCLEAR FERMI GAS MODEL

The nuclear Fermi gas model assumes that each nucleon moves in an attractive net potential which can be represented approximately by a three-dimensional finite square well as shown in Fig. A.1. This potential represents the average effect of the interaction of one nucleon with the other nucleons in the nucleus[38,39]. Since the density of nucleons is approximately constant inside the nucleus, the potential there is constant and then falls off to zero outside the nucleus, within the range of the nuclear force.

Since protons and neutrons are distinguishable from each other, the exclusion principle operates on each type of nucleon independently[38,39]. Therefore we can imagine two potential wells, one for neutrons and the other for protons. In its ground state the nucleons occupy the energy levels of the potential well in some way to minimize the total energy without violating the exclusion principle. Therefore, it is reasonable to treat a nucleus as being a gas composed of two sets of independent fermions. The total excitation of the nucleus, E_x, can then be related to a nuclear temperature, T.

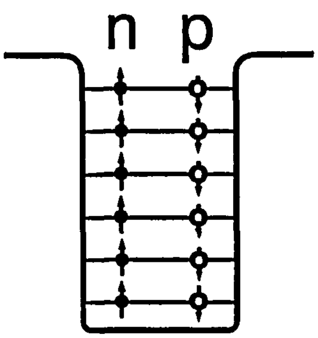

Fig. A.1. The nucleons inside the nuclear potential well. Each nucleon has a spin s = 1/2 and two spin states $m_s = \pm 1/2$. The nucleons at the highest filled level have an energy E_F.

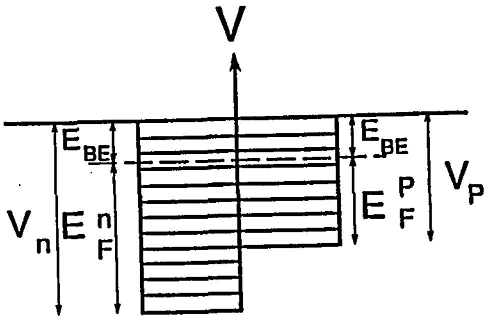

Fig. A.2. The relation between the depth of the potential well, nuclear binding energy and the Fermi energy $(V = E_{BE} + E_F)$ for neutrons and protons.

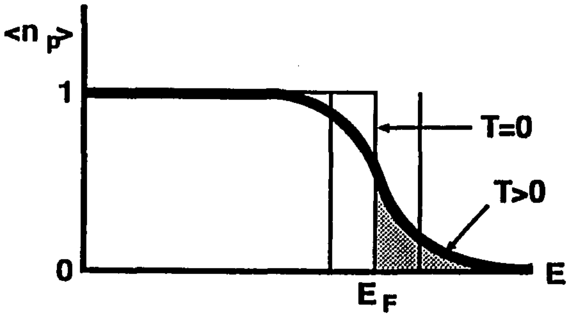

Fig. A.3. Average occupation number in an ideal Fermi gas (T > O).

The energy of a nucleon in the highest-filled level is called the Fermi energy which is defined only at $T = 0°$ K and denoted by E_F (Fig. A.2). Associated with this energy other quantities such as p_F, v_F and T_F *i.e.* the Fermi momentum, velocity, and temperature respectively. The Fermi energy is the maximum kinetic energy of a nucleon bound to the nucleus in its ground state[40]. The Fermi momentum and velocity are the maximum values for a nucleon at E_F. T_F is the classical temperature needed to give a nucleon an energy equal to E_F (e.g. E_F=k T_F). In nuclei we often use energy units of MeV for T, T_F etc. Hence T_F=E_F in units of MeV.

According to Fermi-Dirac statistics, the Fermi energy is given by[39]

$$E_F = \frac{\pi^2\hbar^2}{2m}(\frac{3}{\pi}\rho)^{2/3} \qquad (A.1)$$

where ρ is the density of the nucleon of mass m.

For a nucleus with atomic number A, radius R, its volume is given by

$$V = (4/3)\pi R^3 = (4/3)\pi r_o^3 A \qquad (A.2)$$

where $r_o(\sim 1 \cdot 4\ fm)$ is the nucleon radius. Then

$$R = r_o A^{\frac{1}{3}} \qquad (A.3)$$

Typically, the proton ratio is 45% relative to the total number of the nucleons inside a heavy nucleus. Hence the numbers of protons and neutrons are given by[39]

$$N_p \simeq 0.45A \quad \text{and} \quad N_n \simeq 0.55A \qquad (A.4)$$

Then the densities of protons and neutrons are

$$\rho_p = N_p/V \quad \text{and} \quad \rho_n = N_n/V \tag{A.5}$$

Using (A.2) and (A.4), equations (A.5) can be rewritten as

$$\rho_p = \frac{0.338}{\pi r_o^3} \quad \text{and} \quad \rho_n = \frac{0.413}{\pi r_o^3} \tag{A.6}$$

Using equations (A.6) and $\hbar c$ = 197 MeV-Fermi, $m_p c^2$ = 938 MeV and $m_n c^2$ = 939 MeV, the Fermi energies for the protons and neutrons are

$$E_F^p \simeq \frac{\pi^2 \hbar^2 c^2}{2Mc^2} (\frac{3}{\pi^2} \frac{3.38}{10 r_o^3})^{2/3} \simeq 23\,\mathrm{MeV} \tag{A.7.1}$$

$$E_F^n \simeq \frac{\pi^2 \hbar^2 c^2}{2Mc^2} (\frac{3}{\pi^2} \frac{4.13}{10 r_o^3})^{2/3} \simeq 26\,\mathrm{MeV} \tag{A.7.2}$$

Figure A.2 shows the relation between the depth of the potential well, the Fermi energy, and the average nuclear binding energy E_{BE} ($\simeq$ 8 MeV). The potential well depth for protons and neutrons will be

$$V_0^p = E_F^p + E_{BE} \simeq 23 + 8 \doteq 31\,\mathrm{MeV} \tag{A.8.1}$$

$$V_0^n = E_F^n + E_{BE} \simeq 26 + 8 \doteq 34\,\mathrm{MeV} \tag{A.8.2}$$

i.e the neutron's potential well is deeper because there are more neutrons whereas the Fermi levels are the same for both. Otherwise, β-decay will occur.[41]

The Fermi temperature, T_F, and Fermi momentum, p_F are given by $T_F = E_F/k$, where $k = 0.861 \times 10^{-10} MeVK^{-1}$ is the Boltzmann constant and $p_F = \frac{1}{c}\sqrt{2mc^2 E_F}$.

For the protons, these give $T_F = 2.67 \times 10^{11}$K, and $p_F = 207.7 MeV/c$. This high value of the temperature shows that in the normal cases the nuclear gas is highly degenerate *i.e.* frozen in its ground state or its solid state where most of the particles are in the low energy levels.

Now what happens if the gas is given an extra energy? Some excitation will take place as seen from Fig. A.3. The relation between the energy at temperature T and at T = 0 is[39,42]

$$E_T = E(0)\left[1 + \frac{3\pi^2 n^2}{20}\left(\frac{kT}{E(0)}\right)^2 + \ldots\right] \tag{A.9}$$

where n is the number of the particles and $E(0) = \frac{3}{5} n E_F$, is the energy of the ground-state. Then the excitation energy is defined as

$$E_x = E(T) - E(0) = D(kT)^2 \tag{A.10}$$

where

$$D = \frac{3\pi^2 n^2}{20E(0)} = \frac{\pi^2 n}{4E_F} \tag{A.11}$$

and consequently

$$D_p = \frac{\pi^2\, 0.4A}{4\,(34)} = 0.053\, A \tag{A.12.1}$$

$$D_n = \frac{\pi^2\, 0.6\, A}{4\,(43)} = 0.05\, A \tag{A.12.2}$$

then

$$D \simeq 0.1A \qquad \text{and} \qquad E_x \simeq 0.1\, A(kT)^2 \tag{A.13}$$

where kT is the nuclear temperature in units of MeV.

As an example for an ^{40}Ar projectile given an internal excitation energy of 800 MeV, the nuclear temperature would be $kT \simeq 14.14$ MeV.

APPENDIX B

THE JACOBIAN OF THE TRANSFORMATION OF THE CROSS-SECTION EQUATION FROM THE REST FRAME TO THE LABORATORY SYSTEM

Let us assume that the source is at rest and emits particles with energy E_R and momentum $\vec{p}_R$ at an angle θ_R where the subscript R denotes the rest frame quantities, as seen in Fig. B.1. The spectrum in this system is given[10] by

$$\frac{d^2\sigma(E_R, \theta_R)}{dE_R\, d\Omega_R} = N_0 \sqrt{E_R} \exp(-E_R/T_S) \qquad (B.1)$$

where N_0 is a normalization constant.

In the laboratory the source moves with a constant speed $v_s = v_L$ and emits particles with energy E_L and momentum $\vec{p}_L$. The relations between the rest frame and the laboratory are seen in Fig. B.2. From the figure these relations are

$$\frac{p_R}{m} \sin\theta_R = \frac{p_L}{m} \sin\theta_L \qquad (B.2)$$

$$v_L + \frac{p_R}{m} \cos\theta_R = \frac{p_L}{m} \cos\theta_L \qquad (B.3)$$

and m is the mass of the emitted particle.

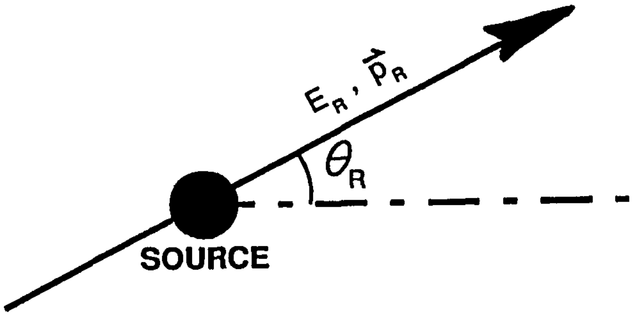

Fig. B.1. Source S at rest in its own frame, emits particles at angle θ_R with energy E_R and momentum $\vec{p}_R$. The source has temperature T_S.

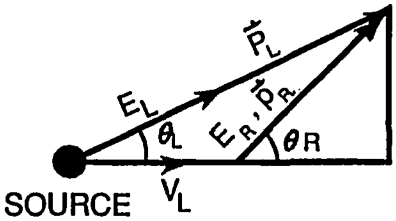

Fig. B.2. Source moves with velocity $v_s = v_L$ in the laboratory and emits particles at angle θ_L with energy E_L and momentum $\vec{p}_L$.

Squaring and adding each side of equation B.2 and B.3 we get

$$\frac{p_L^2}{m^2} = \frac{p_R^2}{m^2} + v_L^2 + \frac{2v_L p_R}{m}\cos\theta_R \tag{B.4}$$

Multiplying both sides by $m/2$ and using $p_R = \sqrt{2mE_R}$, and $E_S = mv_L^2/2$ we get

$$E_L = E_R + E_S + 2\sqrt{E_S E_R}\cos\theta_R \tag{B.5}$$

From the last equation B.3 cos θ_R can be written as

$$\begin{aligned} \cos\theta_R &= \frac{p_L}{p_R}\cos\theta_L - \frac{mv_L}{p_R} = \sqrt{\frac{E_L}{E_R}}\cos\theta_L - m\sqrt{\frac{2E_S}{m}}\frac{1}{\sqrt{2mE_R}} \\ \text{or} \quad \cos\theta_R &= \sqrt{\frac{E_L}{E_R}}\cos\theta_L - \sqrt{\frac{E_S}{E_R}} \end{aligned} \tag{B.6}$$

Using equation B.6, equation B.5 can be expressed as

$$E_R = E_L - 2\sqrt{E_L E_S}\cos\theta_L + E_S \tag{B.7}$$

The Jacobian[1] of the transformation is

$$\frac{\partial(E_R, \Omega_R)}{\partial(E_L, \Omega_L)} = \begin{vmatrix} \frac{\partial E_R}{\partial E_L} & \frac{\partial E_R}{\partial \Omega_L} \\ \frac{\partial \Omega_R}{\partial E_L} & \frac{\partial \Omega_R}{\partial \Omega_L} \end{vmatrix} \tag{B.8}$$

Now let us find each element of this determinant. From equation B.7 we get

$$\frac{\partial E_R}{\partial E_L} = 1 - \sqrt{\frac{E_S}{E_L}}\cos\theta_L \tag{B.9}$$

and

$$\begin{aligned} \frac{\partial E_R}{\partial \Omega_L} &= \frac{\partial E_R}{\partial \theta_L}\frac{\partial \theta_L}{\partial \Omega_L} = \frac{\partial \theta_L}{\partial \Omega_L} 2\sqrt{E_L E_S}\sin\theta_L d\theta_L \\ \text{or} \quad \frac{\partial E_R}{\partial \Omega_L} &= \frac{\sqrt{E_L E_S}}{\pi} \end{aligned} \tag{B.10}$$

where $d\Omega_L = 2\pi \sin\theta_L \, d\theta_L$

From equation B.6

$$\begin{aligned} \frac{\partial \cos\theta_R}{\partial E_L} &= -\sin\theta_R \frac{d\theta_R}{\partial E_L} = \frac{1}{2}\frac{1}{\sqrt{E_R E_L}}\cos\theta_L \\ \text{or} \quad \frac{\partial \Omega_R}{\partial E_L} &= -\frac{\pi}{\sqrt{E_R E_L}}\cos\theta_L \end{aligned} \tag{B.11}$$

Finally from equation B.3 by differentiating both sides

$$\begin{aligned} \frac{p_R}{m}\sin\theta_R\, d\theta_R &= \frac{p_L}{m}\sin\theta_L d\theta_L \\ \text{or} \quad \frac{\partial \Omega_R}{\partial \Omega_L} &= \frac{p_L}{p_R} = \sqrt{\frac{E_L}{E_R}} \end{aligned} \tag{B.12}$$

and by using the results of equations B.9, 10, 11, 12 in the determinant we get the desired transformation

$$\frac{\partial(E_R, \Omega_R)}{\partial(E_L, \Omega_L)} = \sqrt{\frac{E_L}{E_R}} \tag{B.13}$$

Now, applying this result on equation B.1, the laboratory equation will be

$$\begin{aligned} \frac{d^2(E_L, \theta_L)}{dE_L\, d\Omega_L} &= \sqrt{\frac{E_L}{E_R}}\, \frac{d^2\sigma(E_R, \theta_R)}{d\,E_R\, d\Omega_R} \\ &= N_0\sqrt{\frac{E_L}{E_R}}\sqrt{E_R}\, e^{-E_R/T_S} \end{aligned}$$

therefore

$$\frac{d^2(E_L\,, \theta_L)}{dE_L\, d\Omega_L} = N_0\sqrt{E_L}\exp[-(E_L + \frac{1}{2}mv_L^2 - \sqrt{2mE_L}\, v_L \cos\theta_L)/T_S] \tag{B.14}$$

which is the required relation where $v_s = v_L$ is the source velocity and T_S is the source temperature.

APPENDIX C

PARTICLE IDENTIFICATION METHODS

A. The Time of Flight (TOF) Method

The TOF method is used to discriminate different particles on the basis of the time they take to travel from the target to the detector. Usually one measures the relative TOF, since the start signal is taken to be the first event signal and the stop signal is the next rf signal. This is arranged in this backward way to avoid excessive triggering of the electronics. As an example, if the start signal is the beam pulse, then there will be about 50 million start signals/sec for Δt (beam) of 20 ns but it is probable that no particle will be detected for a given beam burst.

The nonrelativistic TOF is given by the relation:

$$TOF = d\sqrt{(M/2E)} \tag{1}$$

where d is the flight path, M the mass, and E is the particle's kinematic energy. Thus, a plot of the TOF vs. energy gives distinct parabolic bands, each representing one mass of particle and those particles with the smaller mass come earlier in time. Although $\mathcal{L}$ is a function of M, E, and z i.e. particles with the same E and m give different $\mathcal{L}$ due to the different z, one may still need z separation *e.g.* to distinguish ^{3}H and ^{3}He.

B. Pulse Shape Discrimination (PSD) method

The pulse shape for each particle is related to the time profile of the current produced at the detector. Mostly these pulses differ in the rise time which is the reason why sometimes this method is called “rise-time discrimination”.

Basically, the idea is to pass the pulses through a shaping circuit to produce bipolar pulses. The time at which the bipolar pulse crosses zero depends on the rise time and the shape of the pulse. Now different particles have different cross over points. The interval between the leading edges and the cross over points are measured and then converted into amplitudes corresponding to different[30] particles.

REFERENCES

1. C. Guet, Nucl. Phys. **A400** (1983) 191C.
2. H.C. Britt and A.R. Quinton, Phys. Rev. **124** (1961) 877.
3. E. Newman and F.E. Steigert, Phys. Rev. **118** (1960) 1575.
4. *Introduction to Nuclear Physics,* by H. Enge, A.W. (1966).
5. D.R. Bowman *et al.,* Phys. Lett. **B189** (1987) 282.
6. J.B. Ball and R.L. Auble, *Nuclear Physics at Cyclotron and Intermediate Energy,* Proceedings of the Second Indo-US Symposium on Nuclear Physics at Cyclotron and Intermediate Energy, ed. B. Sinha, Bombay May 24-28, 1982, p.359.
7. R. Vandenbosch *et al.,* Phys. Rev. **37** (1988) 1301.
8. S. Wald *et al.,* Phys. Rev. **32** (1985) 894.
9. R.L. Robinson *et al.,* Phys. Rev. **24** (1981) 2084.
10. H. Machner *et al.,* Phys. Rev. **31** (1985) 443.
11. J.B. Natowitz *et al.,* Phys. Rev. Lett. **47** (1981) 1114.
12. C. Borcea *et al.,* Nucl. Phys. **A351** (1981) 312.
13. H. Machner, D. Protić, G. Riepe, H.G. Bohlen, KFA Annual Report (Jülich, 1984).
14. G. Caskey *et al.,* Phys. Rev. **31** (1985) 1597.
15. D. Neuhauser and S.E. Koonin, Nucl. Phys. **A462** (1987) 163.
16. Harshaw Chemical Company (unpublished publication on BGO).
17. F.D. Becchetti, P.M. Lister and C.E. Thorn, Nucl. Instr. and Meth. **225** (1984) 280.
18. *Nuclear Heavy Ion Reactions*, by P. Hodgson, Clarendon Press Oxford (1978).
19. V.A. Antonchik *et al.,* Sov. J. Nucl. Phys. **39** (6), June (1984) 944.
20. V.V. Avdeichikov, Phys. Lett. **B201** (1988) 432.
21. K. Möhring, T. Srokowski, D.H.E. Gross, H. Homeyer, Hahn Meitner-Institut für Kernfoschung Berlin (unpublished data).
22. A.C. Shotter, J. Phys. G: Nucl. Phys. **12** (1986) L93.
23. H. Morgenstern, W. Bohne, W. Galster, and K. Grabisch, Atomic Nuclei **324** (1986) 443.
24. J.L. Charvet *et al.,* Phys. Lett. B **189** 388.
25. A. Fahli *et al.,* Z. Phys. **A326** (1987) 169.

26. C.K. Gelbke *et al.,* Phys. Lett. **70** (1977) 415.
27. R.L. Auble, *et al.,* Phys. Rev. **28** (1983) 1552.
28. A.S. Goldhaber, Phys. Lett. **53B** (1974) 306.
29. T. Nakamwia, Nucl. Instr. and Meth. **A240** (1985) 207.
30. *Radiation Detection and Measurements*, by Glenn F. Knoll J.W. (1979).
31. *Tables of Energy Losses and Ranges of Heavy Charged Particles*, by Bakers and Berger NASA Sp-3013 (1964).
32. *TRIUMF Kinematics Handbook*, 2nd ed., by L.G. Greenians (1987).
33. *Bicron NaI Scintillation Detectors*, by J. Bellian and P. Dayton, Bicron Inc.
34. *Nuclei and Particles*, 2nd ed., Emilio Segre, W.A. Benjamin, Inc. (1977).
35. *Probing the interior of 19" × 19" NaI crystal with cosmic muons - A Monte Carlo Simulation*, by B.J. Fineman *et al.,* BNL LEGS report No. 8 (1985).
36. R. Glasow *et al.,* Nucl. Instr. and Meth. **228** (1985) 354.
37. C.F. Maguire *et al.,* Nucl. Instr. and Meth. (in press, 1989).
38. *Quantum Physics of Atoms, Molecules, Solids, Nuclei and Particles,* by Robert Eisberg and Robert Resnick, J.W. (1985).
39. *Physics of Nuclei and Particles,* by Pierre Marmier and Eric Sheldon, Academic Press, Vol. II, (1970) p. 1234.
40. *Nuclear Structure,* Aage Bohr and Ben R. Mottelson, W.A. Benjamin Inc., Vol. I, (1969) p. 141.
41. *Nuclear Physics,* by Enrico Fermi, revised edition, The University of Chicago Press, (1950) p. 161.
42. *Statistical Mechanics,* Kerson Huang, J.W. (1987), p. 264.
43. S. Shaheen *et al.,* Proc. 5th International Conference on Clustering in Nuclei, Kyoto, Japan (1988) unpublished.